Title: Growth and spectroscopic studies (continuous and time-resolved) of ultrathin films of topological insulators

Author: Mateusz Weis

Citation style: Weis, Mateusz. ([2018]). Growth and spectroscopic studies (continuous and time-resolved) of ultrathin films of topological insulators. Praca doktorska. Katowice : Uniwersytet Śląski ; Le Mans : Le Mans Université

Institute of Physics of August Chelkowski
University of Silesia in Katowice

IMMM Insitute of Molecules and
Materials in Le Mans, UMR 6283 CNRS
Le Mans Université

PhD thesis:

Growth and spectroscopic studies (continuous and time-resolved) of ultrathin films of topological insulators

Mateusz WEIS

Doctoral school: **3MPL**

Reviewers:

Professor Jozef Korecki, IFIS - ZFCS, AGH - Krakow

Professor Luca Perfetti, LSI - Ecole Polytechnique - Palaiseau

Examiner:

Professor Grazyna Chełkowska - ZFCS, University of Silesia - Katowice

Professor Massimiliano Marangolo - INSP - University of Sorbonne - Paris

Invited Guests:

Doctor Artur Chrobak, WMFCH - ZFCS, University of Silesia - Katowice Professor Roman Wrzalik, WMFCH - ZBiFM, University of Silesia - Katowice

Professor Andrzej Burian, WMFCH - ZBiFM, University of Silesia - Katowice

Supervisors:

Professor Pascal Ruello, IMMM - CNRS, Maine University - Le Mans

Professor Jacek Szade, WMFCh - ZFCS, University of Silesia - Katowice

Co-supervisors:

Doctor Katarzyna Balin, WMFCh - ZFCS, University of Silesia - Katowice

Doctor Gwenaelle Vaudel, IMMM - CNRS, Maine University - Le Mans

Acknowledgements

First of all, I would like to express my gratitude to my supervisors Professor Pascal Ruello and Professor Jacek Szade, for their patience and guidance during my studies. Their inspiring scientific discussions and insight helped me in all the time of research and writing of this thesis. I could not have imagined having a better advisors and mentors for my Ph.D study. I would like to thank my Ph.D co-supervisor Katarzyna Balin and Gwenaelle Vaudel. Without their precious support it would not be possible to conduct this research. I would also like to thank Embassy of France in Poland for granting me Cotutelle scholarship, without it this research would be impossible. Last but not the least, I would like to thank my family and my Love for supporting me spiritually throughout writing this thesis and my life in general.

Contents

Chapter 1

Outline

Topological insulators (TIs) represent an interesting group of materials that exhibit a quantum phenomena even at room temperature. In 2016 Nobel Prize in physics was awarded for theoretical discoveries of topological phase transitions and topological phases of matter [1]. As stated in the press release of the Nobel Committee laureates: *"opened the door on an unknown world where matter can assume strange states. They have used advanced mathematical methods to study unusual phases, or states, of matter, such as superconductors, superfluids or thin magnetic films. Thanks to their pioneering work, the hunt is now on for new and exotic phases of matter. Many people are hopeful of future applications in both materials science and electronics"*. Over the last decade, topology research has been leading in the field of condensed matter physics - mainly due to the discovery of new topological phases matter and exotic effects not observed in classic materials, giving hope for wide use in a variety of devices. By entering into current trends, we propose an experimental approach to the subject including the creation of TI-based structures and the study and modification of their properties. TI are poorly conducting electricity in the bulk (centre) of the crystal, but the surface electrons are able to move around freely in a manner that is protected from defect scattering. Moreover all electrons moving in a given direction must have their spins, pointing the same way (spin locking), or to put it another way, all electrons with the same spin component must travel in the same

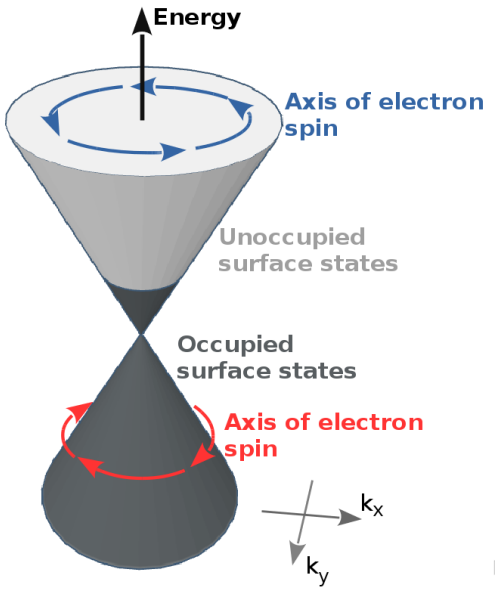

Figure 1.1: Artistic view of Dirac cone in topological insulators.

direction. This spin or internal angular momentum can be imagined as a property associated with particle motion around its own axis (Fig.1.1) [2, 3].

The result possibility to control of moving spin polarized electrons around the material by passing current has generated considerable interest in potential electronic applications. Like for example spin valves or sources (injectors) of spin-polarized carriers, Schottky diodes or even spin-to-charge converters [4, 5, 6, 7]. Such phenomena as surface states and the electron spin polarization is still hard to observe without a highly sophisticated equipment such as angle resolved photo emission spectroscopy (ARPES) [8, 9, 10, 11]. Unfortunately such measurements require extremely fresh surface layer because of low penetration depth of measurements as well as overlapping of the band structure coming from oxidation of the layers. Because of that it is impossible to work on a sample outside of the ultra high vacuum, and even then it is possible to keep complete freshness of the surface only for couple of hours. Fortunately it is possible to still tap into this phenomena in real working conditions. In order to do so it is necessary to utilise the very short penetration depth of the visible light in materials such as

Bi_2Te_3. Due to thorough analysis of the existing oxidised layer it is known that it is a mixture of tellurium and bismuth oxide, which are transparent in visible spectra, that does not disturb the measurement [12]. Because of their similar properties to the passivated layer of aluminium oxide they create stable about 2nm thick layer that protects the material from further damage and moisture.

The technique that can utilise all those properties to its fullest potential is so called pump-probe femtosecond laser spectroscopy. The basic concept of this method is quite simple. Femtosecond laser creates short pulses 200fs (200×10^{-15}s) that are divided into a pumping beam, that excites the electrons and vibration with the thin layer, and probe which detects the change of reflection or transmission as a function of time. This experiment is very similar to creation of stop-motion film one photo at the time, due to a moving mirror (delay line) we are able to "photograph" effect of the pump after a slightly different time. This technique allows subtle interaction with the matter and is able to detect even the slight changes within analysed structure without damaging it. That is why pump-probe spectroscopy is widely used in electronic devices development and control of their quality. The signal registered with this technique consists of different phenomena such as relaxation of the photo-excited carriers, phonon vibrations and even mechanical vibration of different structures in the sample. Due to the ability of direct interaction with the electrons it is possible to observe such subtle changes like modification of electron dynamic even after exposure to air and ageing of the thin film, or to directly register the crystal lattice (phonon) vibration in time domain. In this work we utilized advanced techniques for creation (MBE) of the samples that allow us to perform thorough investigation of the effects generated by variable nanostructures such as state of crystallization or critical thickness dependence as well as phenomena occurring at close proximity to TI-metal interface. This techniques along with careful structural (LEED/RHEED), chemical and electronic analysis (XPS) can provide a great insight into realization of working spintronic and optospintronic systems. We hope that the data presented in this work will bring us closer to understanding of phenomena governing this highly interesting phase of matter.

Chapter 2

Introduction

The primary focus of this work is physics surrounding the topological insulators, in particular, the Bi_2Te_3. In this chapter we will concentrate on bringing closer the subject of this new physical phase of matter and physical phenomena that will help to understand it better. We will also try to outline its present and future applications.

2.1 Topological Insulators

In this section, we described closer the history of topological insulators and physics standing behind them.

2.1.1 Discovery of TIs

To fully understand the concept of topological insulators, we have to mention two most crucial discoveries to this topic. First of which is one of the greatest successes in quantum physics. That is band theory of electric conduction made by Bloch in 1920 [13]. This theory gave us an understanding of process governing the conduction within the crystals. In this model electronic states of electrons are described by Bloch states. These states are plane waves with momentum wavevector $\mathbf{k}$ modulated by the crystal lattice symmetries. This approach brought to live the idea of continues band structure of the solids and gave us a tool to easily distinguish materials that are conductors, semiconductors, or insulators. The reaction of a crystal to an external electric field can be purely determined by the state of electrons close to the Fermi energy. In case of metals in which bands are only partially fielded out, an external current can cause asymmetrical redistribution of the population of electrons along the momentum leading to the launching of the electric current. In case of insulators and semiconductors, energy bands below the Fermi level are filled out, and the empty bands are separated from them by the so-called energy gap. This gap prevents the redistribution of the population of electrons by the external field and in result blocks the launch of the current.

The second important point on the path to the topological insulators was the discovery of integer quantum Hall effect. Effect first predicted by Ando, Matsumoto, and Uemura in 1975 and then directly observed by Kitzling in 1980 [14, 15]. This quantum mechanical version of Hall effects appears in two-dimensional electron systems in presence of low temperatures and strong magnetic fields. Under this circumstances, the Hall conductance σ transforms into a

quantum version with quantized values given by the following expression:

$$\sigma = \frac{I}{V_{Hall}} = \nu \frac{e^2}{h}$$

where σ is Hall conductance, I the channel current, V_{Hall} is the Hall voltage, ν is so-called filling factor and can take integer $(1,2,3...)$ or fractional $(\frac{1}{3}, \frac{3}{7}, ...)$ values, e is elementary charge and h is a Plank's constant. We can interpret this effect as a situation where the bulk of the material can be an insulator while the edges are conducting. In case of two dimensions materials, when electrons are in strong perpendicular to the surface magnetic field, they start to be confined into circular cyclotron orbits. In low temperatures, these orbits are quantized. The energy levels of these quantized orbitals are highly degenerate Landau levels n and take on following discrete values:

$$E_n = \hbar\omega_c \left(n + \frac{1}{2} \right)$$

where ω_c is the cyclotron frequency related to the external magnetic field $\omega_c = \frac{eB}{m}$. In the case when N energy levels are fully occupied and $(N+1)$ is empty, we have a situation similar to the insulator with a gap equal to $\hbar\omega_c$, meanwhile on the edged magnetic field forces the electrons into robust skipping orbits. This effect leads to the situation mentioned above where the material appears to be insulating in bulk and conducting on its edges.

Those two discovers paved the road for Moore and Balents to introduced in 2007 a new phase in condense matter physic "Topological Insulator". This new kind of electronic phase was discovered independently by three theoretical groups in summer of 2006. Soon after that, this exotic state was observered in several real materials such as strained $HgTe$ quantum wells, $\alpha - Sn$, and $Bi_{1-x}Sb_x$ alloys. Those discoveries resulted in rapid development of an entirely new branch of materials which have shown this new phase [2, 3, 9].

2.1.2 Theory of TIs

Origin of this unique quantum phase lies in degeneration of the energy levels of chemical bondings by the break in the crystal field symmetry at the surface of the material (Fig.2.2.a).

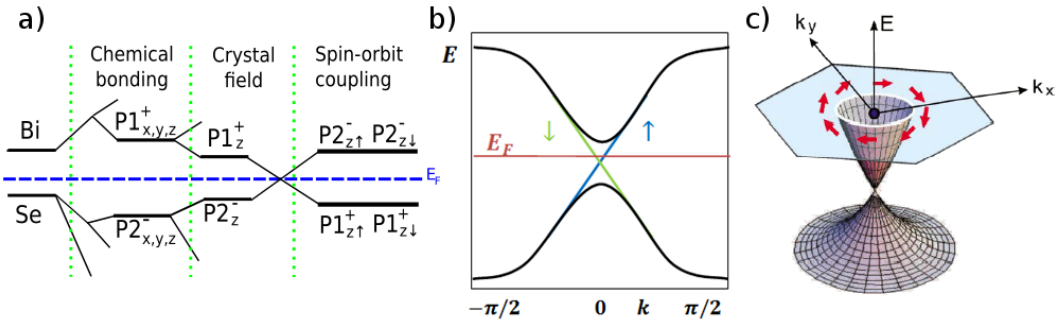

Figure 2.1: a - Evolution of the molecular band structure leading to appearence of TI state. b - Schematic of the spin-polarized surface-states dispersion in bismuth based TI. Green and blue arrow indicate the polarization of the spin. c - 3D visulization of the Dirac cone in TI. From Hasan and Kane (2010).

These degenerated levels are then flipped by strong spin-orbit coupling interaction leading to the creation of the Dirac cone close to the Fermi energy (Fig.2.1.b/c). An effect like that can be observed for materials such as Bi_2Te_3 and Bi_2Se_3 [16] where the Dirac cone lies precisely at the Γ point in Brillouin zone. This materials like any other ordinary insulator or semiconductor show clear bulk energy gap separation, of the lowest unoccupied electronic band from the highest occupied band, but the difference lies in the presence of gapless edge states (2D) or surface states (3D) (Fig.2.1.b and c) which are protected by Θ time-reversal symmetry (product of spatial and spin degrees of freedom). As well as "half-integer" quantum Hall effect (QHE), in which the skin and bottom of the thin film are contributing a half-integer unit of quantum conductance $e62/h$. These two half-integer parts create so-called Hall conductance plateau, which is quantized with integer units of e^2/h[3]. Half-integer QHE is another unique property of TI and is direct proof that surface-states carriers are spin-polarized massless Dirac fermions Fig.2.2. They are the same massless Dirac fermions that exist in other novel material graphene, which consist of only one atom sheet of carbon. In graphene, the charge carriers are, opposed to topological insulators, not spin polarized and exist in four degenerate states (Dirac cones), whereas on a topological insulator surface there is only one Dirac cone, in the

center of Brillouin zone at Γ point. In order to better understand the topological insulators let us introduce the definition of Berry phase that can be interpreted as a phase acquired by the wavefunction, when the parameters appearing in the Hamiltonian are slowly changing in time they allow the system to adapt its configuration (adiabatic process). Lets consider Berry phase in crystal [17]. We can approximate Hamiltonian of the independent electron as:

$$\hat{H} = \frac{\hat{p}}{2m_e} + V(r)$$

where $V(r) = V(r+R_n)$ has a period of the lattice R_n. With boundary conditions $\psi_{mk}(r+R_n) = e^{ikR_n}\psi_{mk}(r)$ where ψ_{mk} is the eigenstate corresponding to the m band and k is the wave number which is defined in the Brillouin zone. We can rewrite them in following way $\psi_{mk} = e^{ikr}u_{mk}(r)$ where $u_{mk}(r)$ has the same period as lattice. The function u_{mk} satisfy the following Schrodinger equation:

$$\hat{H}(k)\,|u_m(k)\rangle = E_m\,|u_m(k)\rangle$$

Let us consider a two-dimensional crystalline system. Then the Berry connection of the m band is equal to:

$$A^{(m)}(k) = i\,\langle u_m(k)|\nabla_k u_m(k)\rangle$$

and the Berry curvature $\Omega^{(m)}(k)$ can be written as:

$$\Omega^{(m)}(k) = \nabla_k \times i\,\langle u_m(k)|\nabla_k u_m(k)\rangle$$

This leads us to the Chern number that can be written as:

$$Q^{(m)} = -\frac{1}{2\pi}\int_{BZ}\Omega^{(m)}(k)dk$$

the above integration is taken over the Brillouin zone (BZ), the Chern number is an intrinsic property of the band structure and has various effects on the transport properties of the system. Chern number is an integral relating the curvature of topological invariant $n \in \mathbb{Z}$ ($\mathbb{Z}$ describes the integers). Good example is genus (Fig.2.2.a and Fig.2.2.b) the topological number, which

Table 2.1: Periodic table of topological insulators and superconductors. Ten symmetry classes are labelled using Altland and Zirnbauer (1997) notation.

Symmetry				**Dimension**							
AZ	Θ	Ξ	Π	1	2	3	4	5	6	7	8
A	0	0	0	0	$\mathbb{Z}$	0	$\mathbb{Z}$	0	$\mathbb{Z}$	0	$\mathbb{Z}$
AIII	0	0	1	$\mathbb{Z}$	0	$\mathbb{Z}$	0	$\mathbb{Z}$	0	$\mathbb{Z}$	0
AI	1	0	0	0	0	0	$\mathbb{Z}$	0	$\mathbb{Z}_2$	$\mathbb{Z}_2$	$\mathbb{Z}$
BDI	1	1	1	$\mathbb{Z}$	0	0	0	$\mathbb{Z}$	0	$\mathbb{Z}_2$	$\mathbb{Z}_2$
D	0	1	0	$\mathbb{Z}_2$	$\mathbb{Z}$	0	0	0	$\mathbb{Z}$	0	$\mathbb{Z}_2$
DIII	-1	1	1	$\mathbb{Z}_2$	$\mathbb{Z}_2$	$\mathbb{Z}$	0	0	0	$\mathbb{Z}$	0
AII	-1	0	0	0	$\mathbb{Z}_2$	$\mathbb{Z}_2$	$\mathbb{Z}$	0	0	0	$\mathbb{Z}$
CII	-1	-1	1	$\mathbb{Z}$	0	$\mathbb{Z}_2$	$\mathbb{Z}_2$	$\mathbb{Z}$	0	7	0
C	0	-1	0	0	$\mathbb{Z}$	0	$\mathbb{Z}_2$	$\mathbb{Z}_2$	$\mathbb{Z}$	0	0
CI	1	-1	1	0	0	$\mathbb{Z}$	0	$\mathbb{Z}_2$	$\mathbb{Z}_2$	$\mathbb{Z}$	0

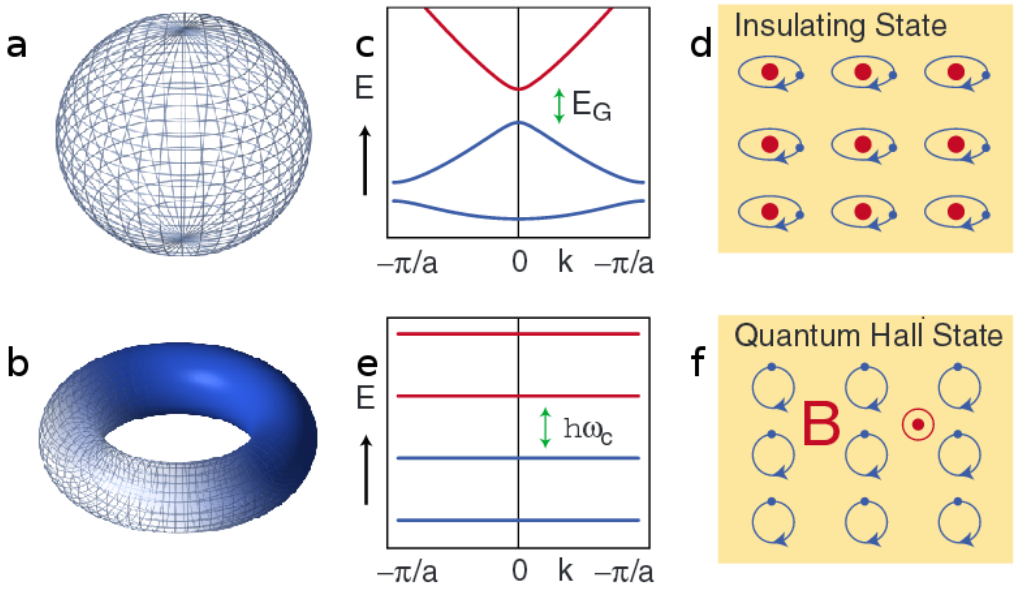

Figure 2.2: Example of object with genus g=0 (a) and g=1 (b) . c and d depict model of insulator. e and f are model of quantum Hall state. From Hasan and Kane.

counts the quantity of holes, that remains constant under continues and smooth transformations. In presented below table we listed the topological classification of topological insulators and superconductors according to presence or absence of time symmetry Θ, particle hole symmetry Ξ and chiral symmetry $\Pi = \Xi\Theta$. Values in columnns 2,3 are specifying the Θ^2 and Ξ^2, we can see that this symmetries as a function of dimensionality show regular pattern of topological systems ($\mathbb{Z}, \mathbb{Z}_2$ and 0)[3]. According to M.Z. Hasan and C.L. Kane we can find that materials with quantum Hall state occupy class *A* with no symmetry and exist in 2D materials; TI which require $\mathbb{Z}_2$ can be found in class *AII* with $\Theta^2 = -1$ in 2D and 3D materials; super conductors (SC) which can posses either $\mathbb{Z}$ or $\mathbb{Z}_2$ can be found in class *D* with $\Xi^2 = 1$ required for the existence of Copper pairs, in 1D and 2D materials. Simplest example of $\mathbb{Z}_2$ system can be presented with the Kitaev's toy model [18] for one dimensional spinless plane wave superconductor [Fig.2.3]. Let us consider following Hamiltonian to describe above situation:

$$H = -\mu \sum_j c_j^+ c_j - \frac{1}{2} \sum_j (t c_j^+ c_{j+1} + \Delta e^{i\varphi} c_j c_{j+1} + h.c.)$$

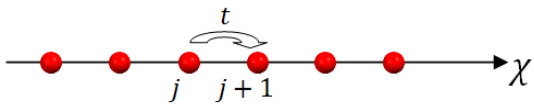

Figure 2.3: 1D crystal with hopping constant t.

where μ is chemical potential and t is a hopping constant between j and $j+1$; Δ describes superconducting band gap; $e^{i\varphi}$ is phase of SC and c_j describes spinless fermion operator and:

$$t \geq 0 \quad and \quad \Delta \geq 0$$

because we have superconducting gap. Because of the Pauli exclusion principle all spinless states must have odd parities. In our divagation we will consider the simplest case of plane wave with periodic boundary conditions:

$$c_k^+ = (c_k^+ c_{-k})$$

$$H = \frac{1}{2} \sum_{k \in B.Z.} c_k^+ H_k c_k$$

Were H_k takes form:

$$H_k = \begin{pmatrix} \varepsilon_k & \tilde{\Delta}_k^* \\ \tilde{\Delta}_k & -\varepsilon_k \end{pmatrix}$$

where

$$\varepsilon_k = -tcos(k) - \mu \quad \text{is even function}$$
$$\tilde{\Delta}_k = -i\tilde{\Delta} e^{i\varphi} \qquad \text{is odd function}$$

All above expressions can be derived to the form:

$$H = \sum_{k \in B.Z.} E_{bulk} a_k^+ a_k$$

Where $a_k^+ a_k$ are so called Bogoliubov quasi particles and are representing Cooper pairs. We can rewrite them to represent electron hole branches:

$$a_k = u_k c_k + v_k c_{-k}^+$$

where $u_k c_k$ is electron branch and $v_k c^+_{-k}$ is hole branch. By solving the case of SC we will get following expressions:

$$u_k = \frac{\tilde{\Delta}_k}{|\tilde{\Delta}_k|} \frac{\sqrt{E_{bulk} + \varepsilon_k}}{\sqrt{2E_{bulk}}}$$
$$v_k = \left(\frac{E_{bulk} - \varepsilon_k}{\tilde{\Delta}_k} \right) u_k$$
$$E_{bulk} = \sqrt{\varepsilon_k^2 + |\tilde{\Delta}_k|^2}$$

To find the gapless solutions we need to find condition when energy is equal to zero. Those gapless bulk excitations occur at:

$$\mu = t \quad \text{or} \quad -t$$
$$k = 0 \quad \text{or} \quad \pm\pi$$

and this is true, for example let us insert $\mu = -t$ and $k = 0$, we will receive $\varepsilon_k = 0$. Because $\tilde{\Delta}_k$ is an odd function of k, Cooper pair is forbidden at $k = 0, \pm\pi$. We can now receive one of two possible states of the system. Let us rewrite the H_k in fallowing way:

$$H_k = h(k) \cdot \sigma$$

where σ are Pauli spin matrices. Let also include following operations of symmetry:

$$\begin{cases} h_{x,y}(k) = -h_{x,y}(-k) \\ h_z(k) = h_z(-k) \end{cases}$$

then in case $k = 0$:

$$h(0) = S_0 \hat{z}$$

and if we have $k = \pi$:

$$h(\pi) = S_\pi \hat{z}$$

Let us define new quantity which will be a product of S_0 and S_π:

$$\nu = S_0 S_\pi = \begin{cases} 1 & \text{trivial} \\ -1 & \text{topological} \end{cases}$$

The trivial phase occurs when $\mu < -t$ and topological when $\mu > t$. For example trivial phase expression $S_0 \longrightarrow k = 0$ will cause:

$$\varepsilon_k = -tcos(0) - \mu = -(\mu + t)$$

because for trivial phase $\mu < -t$:

$$-(\mu + t) > 0 \longrightarrow S_0 = 1$$

and for expression $S_\pi \longrightarrow k = \pi$:

$$\varepsilon_k = -tcos(\pi) - \mu = t - \mu$$

because for trivial phase $\mu < -t$:

$$t - \mu > 0 \longrightarrow S_\pi = 1$$

and so product of those two will give:

$$\nu = S_0 S_\pi = 1 \longrightarrow trivial$$

Such system is called $\mathbb{Z}_2$ topological system. Chern number possess physical interpretation of the Berry phase of the Bloch wave functions. For example, a standard insulator (Fig.2.2.c and Fig.2.2.d) differs from the Quantum Hall State (Fig.2.2.e and Fig.2.2.f) only by the topology of the 2D band structure [3]. In QH we can distinguish metallic edges at the boundaries of the 2D electronic system, what is very similar to the 2D TI surface states. Physics of the topological insulators involves mainly the interaction between bulk (dimension d) and the surface (dimension d-1). Such states can be observed at a system with d=2 and d=3. For example, direct measurements of the band gap structure with ARPES have directly shown the formation of this novel state with a strong dependence on the thickness of the material (Fig.2.4) [9, 10, 11]. The 3D topological insulator can be characterized by the $\mathbb{Z}^2$ topological invariant. For the material to exhibit this phase, it is necessary to meet few conditions. First is

the existence of four time-invariant points at $\Gamma_{1,2,3,4}$ in the B.Z. and Kramers degeneracy of the surface state by crystal field. The second one is breaking of this degeneracy away from those particular points by dominant spin-orbit coupling [16]. If conditions mentioned above are met surface states form the Dirac cone. This leads to appearance of the unique 2D topological metal and massless Dirac fermions (their mass is the second derivative of the Energy in k, and for this cone is equal to 0), what is the direct cause of the ballistic conductance of those materials. Additionally, this new metallic state posses non degenerated spin surface states on Fermi surface. This phenomenon is directly caused by time symmetry which requires that k and -k possesses opposite spin.

In this we can observe non-trivial Berry phase, which strongly influences the interaction with magnetic fields as well as effects of the disorder. We can say that electrons in strong topological insulators are not localized even in the presence of disorder, what is analogous to the quantum spin Hall insulators edge states.

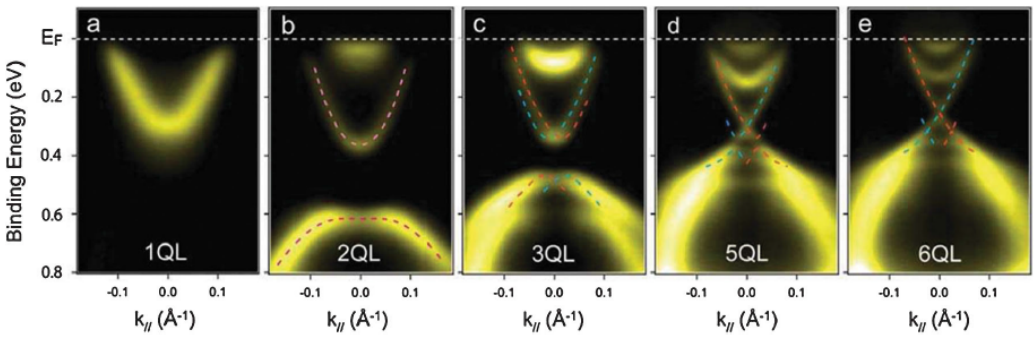

Figure 2.4: Crossover of the three-dimensional topological insulator Bi_2Se_3 to the two-dimensional limit. From Yi Zhang Nature Phys. (2010).

2.2 Applications of topological insulators and limitations of the technology

Topological insulators exhibit unique and fascinating electronic properties, such as the quantum spin Hall effect, quantum anomalous Hall effect, and topological magneto electric effect, as well as magnetic monopole images and Majorana fermions [2, 19, 20]. Unique properties of topological insulator have great possible applications for spintronics and quantum information processing, as well as magneto electric devices with higher efficiency and lower energy consumption [2, 4]. Currently the most promising branch of spintronics where topological insulators can find their use is spin-charge conversion thanks to their strong spin-orbit coupling [5, 6, 7] they poses the crucial ability to connect charge with spin degree of freedom. Ability to control the spin current by charge transport and reverse are the main goals of spintronics. Topological insulators, thanks to their strong spin orbit coupling and possession of insulating bulk and metallic surface states with a Dirac cone dispersion, gained reputation of perfect candidate for realization of spin-charge conversion devices. Thanks to unique helically locked, in Fermi contour, spin and momentum at the surface of TI injection of the spin current into the surface of a TI will result in appearance of 2D charge current density on the surface

(known as the inverse Edelstein effect) [21]. Recently, the IEE was shown experimentally by spin pumping [22, 23]. The helical surface states of topological insulator lead to a non-zero Berry's phase (π) of the electron wave function generating a broad spectrum of phenomena such as absence of back-scattering [24, 25] and weak antilocalization [26].

Creation of new devices based on this material requires from us better understanding of the phenomena surrounding this structures as well as knowing all limiting factors that will put a barrier in their development. One of the phenomena that somehow was disregarded so far in the literature is the role of electron-phonon coupling. As it is well known spin orbit coupling is essential in formation of the topological state, but the electron-phonon coupling appears to set a limit on 2D surface electron transport. It was already shown that existence of strong coupling with LO mode mode [27] and strong coupling of 2D surface electrons with LA mode [28] put limits on electron transport. Knowing that the electron-phonon coupling plays such an important role in this materials it is even more important to well know this coupling behaviour[29].

Second important challenge ahead of us is enhancement of the surface states contribution into overall properties of the topological insulator material. In case of ultra thin films the ratio of surface states to bulk states starts to be not negligible and grants us ability to design a working components based on those materials, and through use of advanced techniques of deposition it is possible to achieve high quality crystals [30]. In the case of thin films, at a critical thickness the surface states from opposite surfaces of the films can couple together and open thickness-dependent gap (Fig.2.4) [9, 31, 32], which is non trivial and may give rise to quantum spin Hall state similarly to HgTe quantum wells [33]. The band gap opening, in compounds like Bi_2Se_3 and Bi_2Te_3, has been reproduced theoretically and it has been reported that additional quantum size effects should appear leading to topological quantum phase transitions that depend on the film thickness. So far this phenomenon was observed only by angle resolved photo-emission spectroscopy that has to be made under perfect high vacuum and with the samples which surface is extremely fresh, usually few minutes after deposition or cleaving of the crystal. Even then the measurements prove to be difficult because of rapid evolution

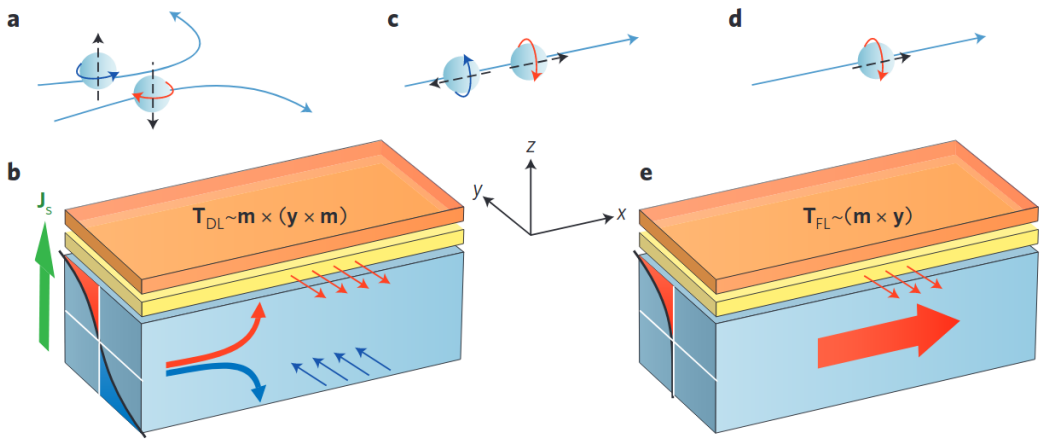

Figure 2.5: Presentation of effects generated by spin-orbit coupling for working spin-current conversion: a Thanks to the Magnus effect spin Hall effect create force that acts on spinning particles. b, On schematic Heavy metal with strong spin-orbit coupling is marked with blue, with yellow ferromagnetic layer and on top (orange) protective capping layer. Torque created by the spin Hall effect in a magnetic bilayer separates moving spins into aligned parallel (blue arrows) and anti-parallel (red arrows) to the direction of flow, this produce polarized spin current J_S (green arrow). This effect generates anti-damping torque T_{DL} that depends on the magnetization m and the direction of the spin accumulation y. c To nullify effect of the Magnus force spin angular momenta (dashed arrows) must be frozen along the current direction. d In case of a system without inversion symmetry like in topological insulators, this effect creates spin polarized current. In case of breaking the inversion symmetry directly at the interface between the material with strong spin-orbit coupling (blue) and ferromagnetic layer (yellow) spin accumulates along the transverse direction leading to appearance of non-equilibrium spin-orbit torque T_{FL}. From A. Manchon Nat.Phys.(2014).

of the states in presence of small amount of adsorbents. In order to gain better understanding of the processes of electron and phonon dynamics, under working conditions or exposure to air, new approach to sample geometry and experimental methods like femtosecond laser spectroscopy have to be employed [12].

The third important part necessary to understand, in order to create working devices, is the reaction both chemical as well as physical of topological insulators with additional materials deposited on it [34]. Currently carried experiment of spin-current conversion require close proximity to ferromagnetic (Fig.2.5) or metallic layer with strong spin orbit coupling like platinum or cobalt [5, 6, 7]. The greatest challenge, to efficiently harness the potential of topological insulator, is to create a stable chemically system that conserves the topological insulator surface states and still allow the transfer of generated polarized spin current into other layers. This requires from us a thorough investigation of the chemical states and potential chemical reactions and evolutions of such interfaces. Knowledge gained through that would be crucial in finding proper configurations, that retain the proper evolution of the band system of topological insulators (like in a case of trivial interfaces [2, 3]), for realization of new generation of spintronic devices.

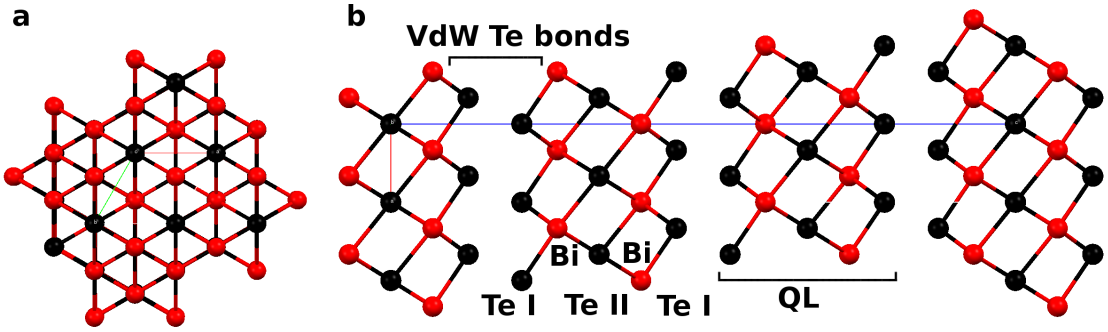

Figure 2.6: Crystallographic structure of Bi_2Te_3 with the QL's connected through Van der Waals Te bonds. a Depicts view from **c** plane and b from the **b** plane.

2.3 Basic Information on Bi_2Te_3

Bi_2Te_3 is promising material which exhibits topological insulating properties [16]. Similarly to the Bi_2Se_3 and Sb_2Te_3 it belongs to the 3D topological insulator family which are more closely described in previous subsection. Bismuth telluride in its bulk form is a narrow bandgap semiconductor which, aside of its TI behaviour possess very strong thermoelectric properties, that play an important role in thermoelectric devices. This semiconductor have one of the highest figures of merit at room temperature. It is very promising material for wide application in electronics and especially in quantum computing due to very good parameters and high ballistic conductivity.

Bi_2Te_3 is trigonal rhombohedral crystal with 15 atoms in unit cell, with Hermann - Mauguin index R$\bar{3}$m:H and space group number 166. Single unit cell possess one bismuth atom in coordinate [35] at:

$$\text{Bi(x,y,z)} = (0.00000;\ 0.00000;\ 0.40046)$$

two not equivalent positions of tellurium atoms at

$$Te_1\text{(x,y,z)} = (0.00000;\ 0.00000;\ 0.00000)$$

$$Te_2\text{(x,y,z)} = (0.00000;\ 0.00000;\ 0.79030)$$

and unit cell parameters

$$a = b = 4.395 \text{ Å} \quad c = 30.440 \text{ Å}$$
$$\alpha = \beta = 90^\circ \quad \gamma = 120^\circ$$

Bi_2Te_3 can be easily cleaved along the trigonal axis due to Van der Waals bonding between neighbouring tellurium atoms Fig.2.6. This figure presents cell generated with crystal visualisation program Mercury using shown parameters.

In the recent years electronic properties of Bi_2Te_3 compound have been experimentally and theoretically studied by various ab-initio methods ([36, 37]). Theoretical calculations have shown that Bi_2Te_3 is a narrow-gap semiconductor and its gap structure strongly depends on spin-orbit coupling. Calculations shown in this work were performed in case of non spin orbit simulations on $20 \times 20 \times 4$ k-point mesh, and full spin-orbit calculations on $30 \times 30 \times 6$ k-point mesh. Calculations of the band structure were performed with and without taking into account the spin-orbit coupling. Such calculations were performed with spin-polarised Hamiltonian and additional $\sigma \cdot L$ term responsible for this coupling. In addition very weak external field of $0,017T$ was added in direction of z-axis in order to break spin symmetry. Calculated band structures without and with spin-orbit coupling are shown in Fig 2.7. It can be seen that Bi_2Te_3 is a semiconductor with a narrow energy gap. The character of the gap strongly depends on the spin-orbit interaction. This coupling changes the shape of the bands and the character of the gap from a direct to indirect one, such result was already reported in this material [36]. From the calculations of the total density of states the value of the energy gap, changed in case of calculations without spin-orbit coupling from $0.36eV$ down to $0.08eV$ in the case of spin-orbit calculations. This value is very close to experimental one of $0.145eV$ [38].

Beside the crucial spin-orbit coupling effect on the features of surface and bulk electrons dynamics, the large electron-phonon coupling mechanisms is the object of active discussion and appear to play a peculiar role in the transport properties of the TIs. Bismuth telluride possess both optical and acoustic phonons modes, which are depicted in Fig.2.8 and table.2.2. Structure of this compound with 3 inequivalent positions give rise to three acoustic phonon

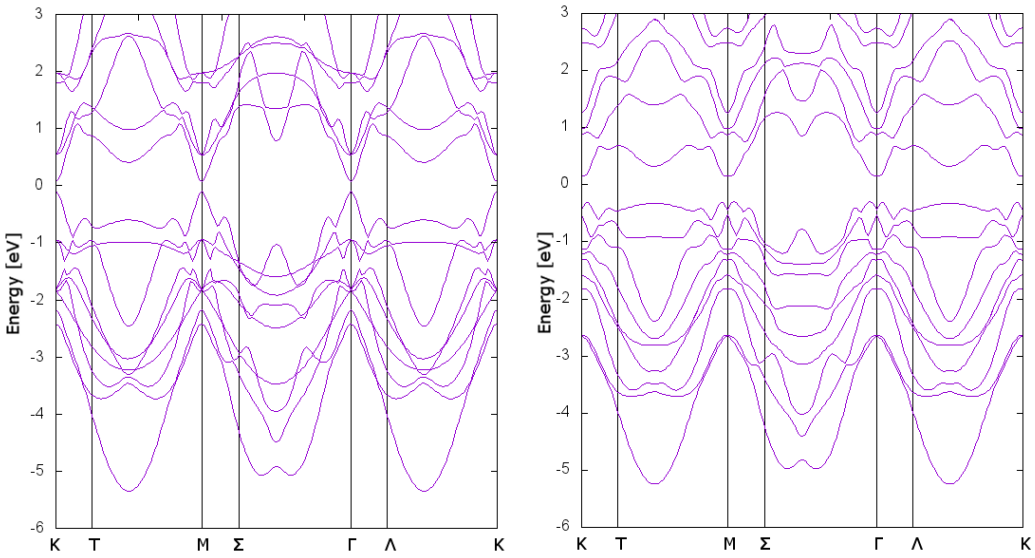

Figure 2.7: Band structure a) without and b) with spin orbit interactions.

Table 2.2: Phonon modes frequencies (in THz) of Bi_2Te_3. Letters "E" in-plane and "A" out-of-plane lattice vibrations, letter g denotes Raman active and u IR active modes.

Name	Raman[39]	IR[39, 40]	Simulation [41]
A^1_{1g}	1,88		1,84
A^2_{1g}	4,02		3,74
A^1_{1u}		2,82	2,88
A^2_{1u}		3,60	3,58
E^1_g	1,10		1,47
E^2_g	3,09		3,42
E^1_u		1,50	1,43
E^2_u		2,85	2,90

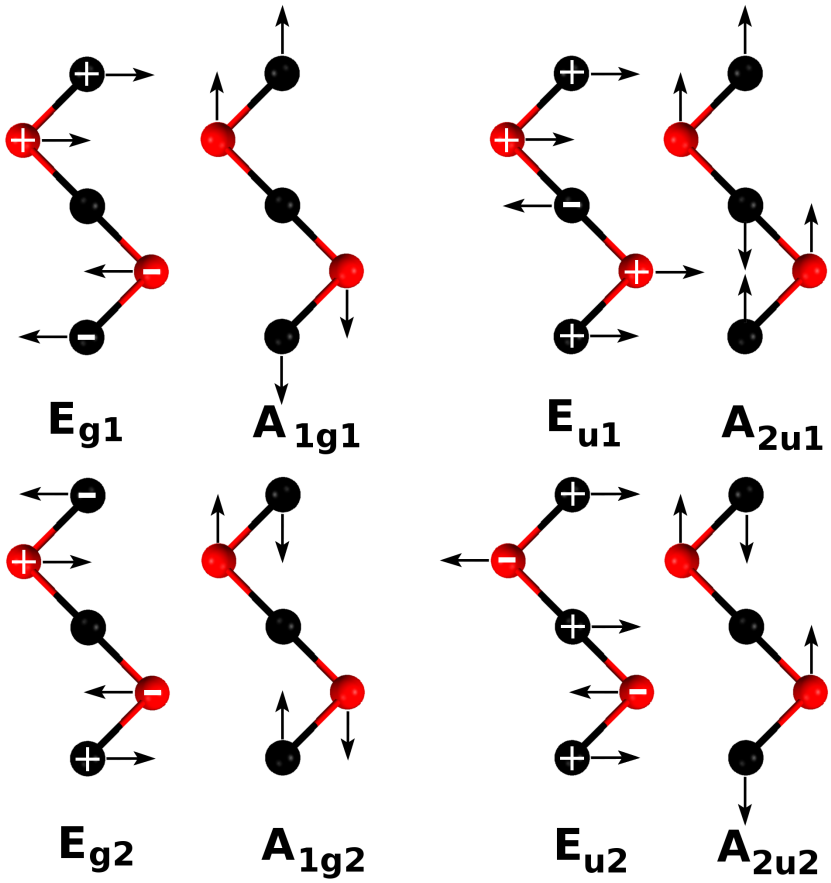

Figure 2.8: Optical phonon modes in Bi_2Te_3. The "+" and "-" signs in presented figure describe motions toward and from the observer.

modes and twelve optical phonon modes. With two distinguish sub groups Raman active A_{1g} and E_g and two Infra-red active A_{1u} and E_u [41].

Chapter 3

Samples preparation

In this chapter we will describe the process of crystal growth with prime focus on the molecular beam epitaxy technique. In the main section we will present the developed techniques of deposition Bi_2Te_3 ultra thin films as well as I will go in to detail regarding the preparation of samples used in this work.

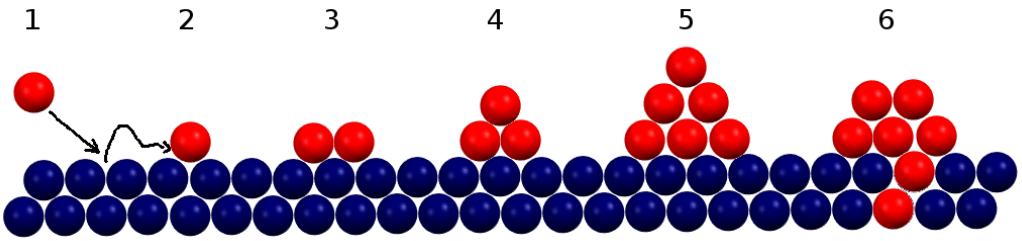

Figure 3.1: Steps of thin film growth: 1 - absorption, 2 - surface diffusion, 3 - chemical bond formation, 4 - nucleation, 5 - microstructure formation, 6 - bulk changes.

3.1 Growth of ultra thin films

We can differentiate 6 different steps in crystal growth Fig.3.1[42]. First one the absorption or physisorption when approaching atom can be either reflected or absorbed on the top of the substrate surface. This step strongly depends on rate of the flux of incoming atoms, the trapping probability and sticking coefficient.

In the second step of the crystal growth overall surface energy is being minimized by atoms which have enough energy to diffuse to low energy site. This step is strongly govern by the temperature of the surface, through diffusion rate k_s that increase with the temperature [42]. The diffusion length of relaxing atoms has a following form:

$$\Lambda = a\sqrt{k_s t}$$

where t is the diffusion time and a is the hop distance. Λ at low temperatures increase with temperatures, while at higher temperatures desorption from the substrate overtakes the absorption causing the Λ to shorten. Typical diffusion lengths for physisorption is $300\mu m$ while for chemisorption this distance is much shorter $5nm$[42].

In third step after being physisorpt the atom can start to chemicaly bond (chemisorption) to molecule-molecule or substrate-molecule or desorpt from the surface. In order for the atom to be either physisorpt or chemisorpt it has to overcome local energy barriers (Fig.3.2). Arriving atoms that manage to attach to the surface create tension (energy) in the surface by stretching

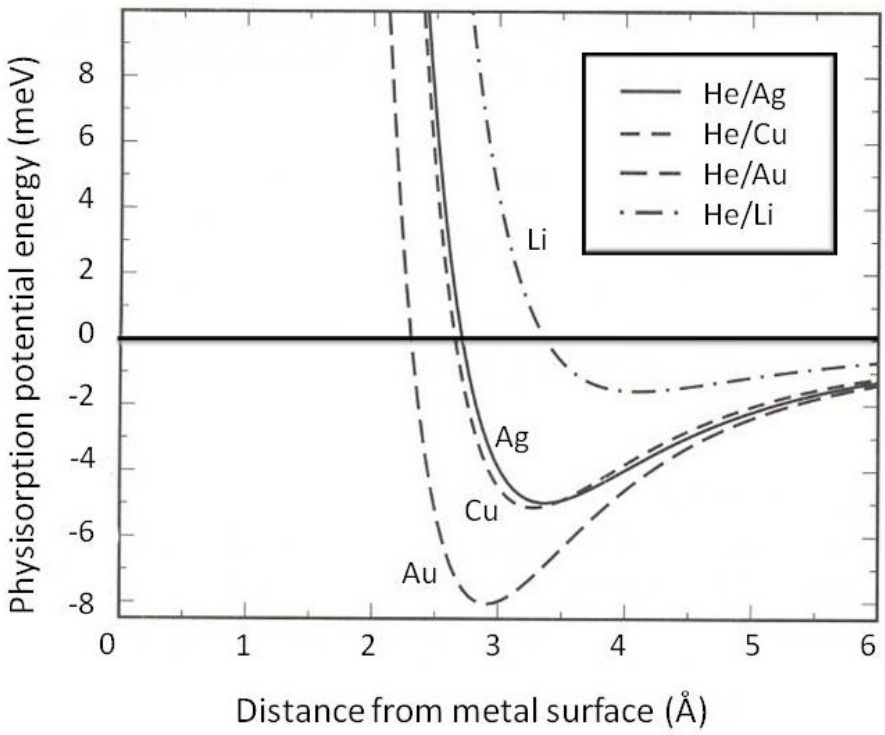

Figure 3.2: Physisorption potential energy for Helium calculated for various metal substrates (from E. Zaremba et.al [43]).

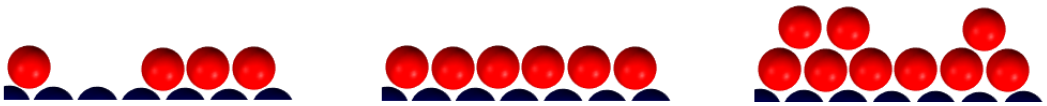

Figure 3.3: Frank van der Merwe crystal growth - Layers.

the bonds of substrate atoms. Such energy is a function, of broken bond energy of the top layer atoms, which depends on the crystal structure of used substrate. We can distinguish two main types of the substrate structures used for the growth process. That is heteroeptaxial structure where there is a strong mismatch between the crystal structure and homoepitaxial where the crystal structure of both substrate and grown material are very close or identical.

In fourth step deposited material start to create nuclei of the crystal. This step is extremely critical to create a stable film. In case of to small nuclei the total surface energy is overpowering the process of proper crystallization. We can say that the nuclei has optimal size when by adding additional molecules we are able to decrees the Gibb's free energy. We can distinguish two types of nucleation undesirable one Homogeneous which is a rare occurrence [42]. Where the free energy of the atoms in a gas form is smaller than when they are nucleated. Second one desirable so called Heterogeneous where the nucleation on the substrate surface reduces the Gibb's energy by reducing the surface area. Nucleation processes are strongly dependant on the substrate temperature which determines the size of the crystal embryos but increase the barrier for nucleation. As well as depend on the deposition rate. With higher deposition rate the critical size of the nuclei decreases but the energy barrier for nucleation diminish. Rate of the process of nucleation N depend on three parameters:

$$N = N^* A^* \omega$$

N^* the equilibrium concentration of stable nuclei, A^* critical area of embryos and ω the rate in which the incoming atoms cover said area.

In fifth step when the nuclei are big enough they start to merge in one of the following ways.

Large particles are taking the material from small ones (Ostwald Ripening). Two nuclei are forming a neck between each other. Shape of the neck allows for faster growth and merging of both nuclei (Sintering). Nuclei can as well undergo surface diffusion, when both nuclei are in local energy minimum they will align and merge (Cluster Coalescence). The merging nuclei start to form the microstructures. We can distinguish three different kinds of film forming. First one the Frnak van der Merwe growth (Fig.3.3) where the layers tend to form uniform layers one by one. This growth happens when the substrate-vapour surface energy is larger than the total surface energy of the film. This results in smooth film that wets the surface decreasing the energy of surface tension. Second form of growth is Volmer Weber growth (Fig.3.4.a) where the film start to grow in Island like structures. This occurs when the entire surface energy of the interface is larger than substrate-vapour energy. This situation leads to accumulation of film into an islands in order to minimize the surface area touching the substrate. This leads to films with uneven growth and very slow internal diffusion due to accumulation of structural defects. Third type the Stranski-Krastanov growth is a mixture of the two (Fig.3.4.b). During this growth in the initial phase the film is growing in uniform layer, and after few monolayers it starts to grow island like structures. This is the result of straining of the initial layer near the interface with the substrate, where grown layer starts to match the structure of the underlying substrate. This stress after few layers start to relax changing in result the overall surface energy of deposited film [42].

In the last and final step the deposited layer starts to relax. Structure of the film goes into a local minimum of the energy by diffusion of atoms. In results that leads to formation of defects within the layer and grain formation. Defects in crystals, that is break in periodicity by shift of position of singular atoms or whole molecules or even entire grains can be divided into 4 separate categories. Point defects that that occur within single cell and do not expand in any direction, there are few defects in this category. Vacancy defect - where one of the positions in unit cell is vacant. Surrounding crystal structure prevents the structure from collapsing. This type of defect is called as well Schottky defect. Antisite defect - where atoms if different type

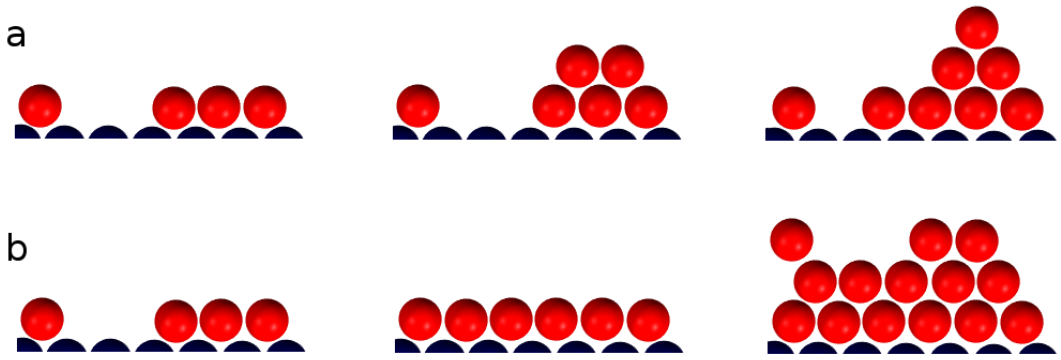

Figure 3.4: a - Volmer Weber crystal growth - Islands. b - Stranski-Krastanov crystal growth - Mixed

change places. Interstitial defect - which is caused by atom occupying a site that usually do not exists. Frenkel defect - when the interstitial and vacancy defect occur at the same place. Line defects that are dislocations of entire planes of the crystal. We can distinguish two main types of this defect. Edge dislocation that is termination of QL within the crystal, causing the adjacent planes to bend around it. Screw dislocation that is spiral like growth of the planes of crystal where each layer has slightly different angle of growth. Planar defect include all grain formations such as boundary defects between grains where direction of lattice abruptly changes. Stacking faults when local change of the stacking sequence in complex crystal is changed. Twin boundaries where neighbouring grains poses mirror symmetries to each other. To this category we can also include step formation between atomically flat terraces. The last group of defect are bulk defects that include formations of pores, cracks and inclusions. This group include as well voids in the crystal and clusters of impurities so called precipitates.

3.2 Molecular beam epitaxy (MBE)

All samples described in this work are thin films prepared by thermal evaporation in Molecular Beam Epitaxy chamber (Fig.3.5 for overview of the samples see table 3.1.). In MBE, material is evaporated under high vacuum ($10^{-9} - 10^{-12}$mbar) from effusion cells, forming molecular beams that are incident upon a heated sample. Lack of carrier gases and ultra-high vacuum environment, makes the MBE the best method for creation the highest purity grown films. A typical MBE vacuum chamber effusion cells are situated directly underneath the substrate. Cells are equipped with shutters covering them to enable control over which material is being deposited. Typical effusion cells consist of a crucible for the source material, and a heating source. There are two types of heating used in such effusion cells that is ohmic heating from a filament wound around the crucible or by electron beam heating. In case of electron beam heating electrons from cathode are accelerated through a potential of a few kV toward the material usually in shape of thin cylinder. Such technique allows to deposit large amounts of power, generating heating in the source material up to $2400^{o}C$. Evaporated material is then directed on to the sample manipulator on which samples are mounted. Such manipulator allows rotation of the sample, that is necessary to create uniform coverage of the produced layer. Typical sample holder consists of the substrate, onto which the material is deposited, and includes heating system. Holder typically have one of two forms of heating: resistive up to $1000^{o}C$ or by electron beam.

Presented above chamber (Fig.3.5) was used in our experiments and is equipped with RHEED (reflected high energy electron diffraction, described in 4th chapter), quartz micro balance and mechanical shutter. The quartz crystal microbalance (QMB) measures the change of mass of deposited material per unit area by detecting the variations in frequency of a quartz crystal resonator. Thanks to the high precision of this device it is possible to achieve stable rates with extremely low flux with precision of 10^{-5}Å/s. The mechanical shutter allow us to cover parts of the substrate during the deposition. This gives us ability to create steps on the sample, regions with different thickness or partially cover the sample with different material.

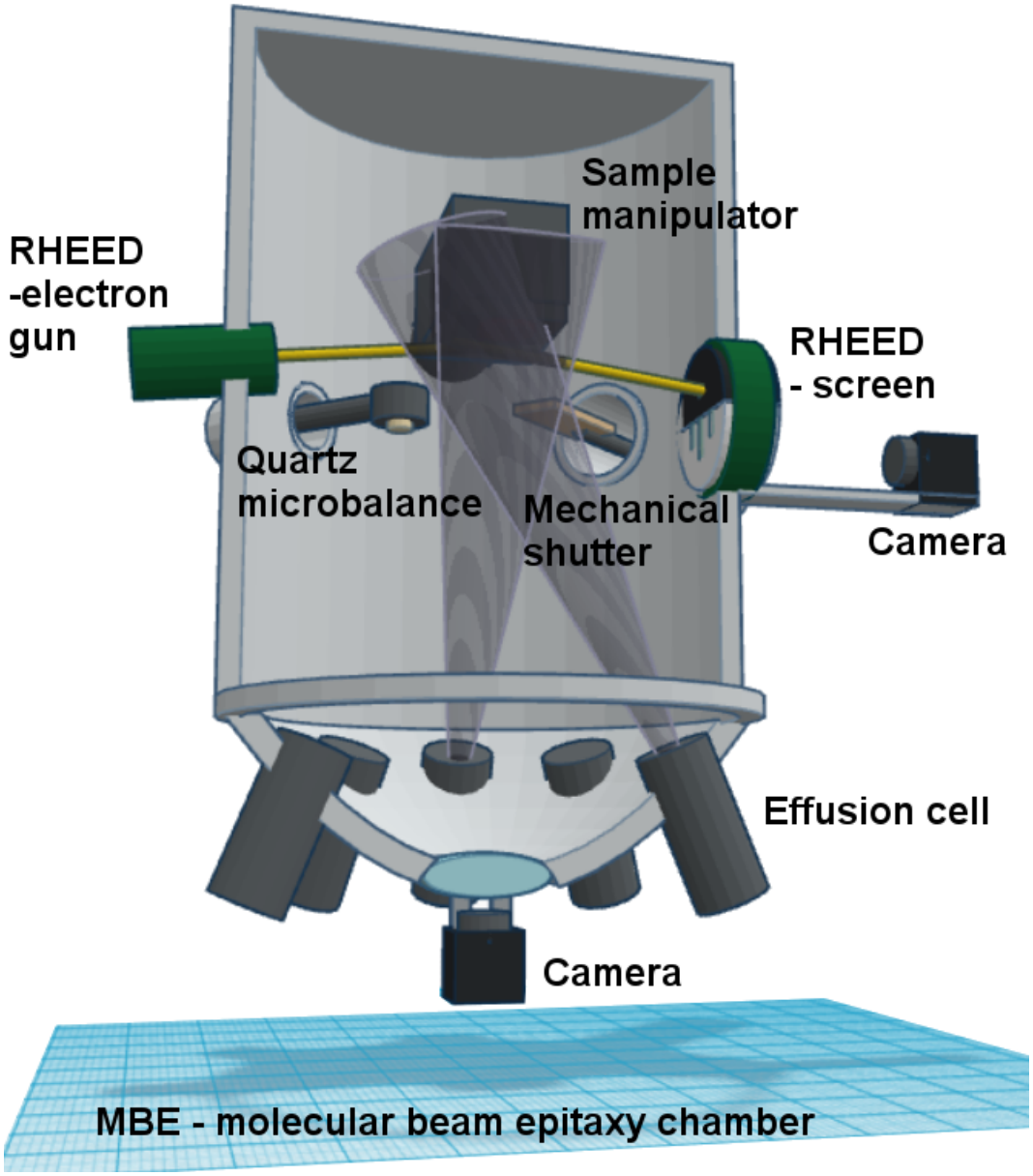

Figure 3.5: Model of MBE chamber used in our experiments.

MBE deposition rate (typically less than 30 000 Å/h) allows the films to grow epitaxially, that is layer by layer. With a growth strictly imposed by the substrate. In industrial applications it is required that the deposited material will create a crystalline overlayer with well-defined orientation to the substrate crystal structure. We can distinguish two main types of epitaxy. First one the Homoepitaxy where the substrate has exactly the same crystallographic structure as the deposited material or the structure is very close to it, this type includes deposition of the same material as substrate to achieve for example a different kind of doping. Heteroepitaxy is epitaxy where the substrate crystallographic structure differs from the deposited material, this allows sometimes to make the grown layer take a different not achievable by other means crystallographic orientations.

Figure 3.6: High vacuum cluster in laboratory of Surface Physics in Institute of Physics, University of Silesia.

3.3 Sample description

As previously mentioned all samples described in this work are thin films prepared by thermal evaporation in Molecular Beam Epitaxy chamber from PREVAC company, which is part of high vacuum cluster in laboratory of Surface Physics in ŚMCEBI in Chorzów. Samples were made using two different substrates, Muscovite mica (110) (Ted Pella. Inc.) and silicon (001), and two different growth methods [30] [44]. Core objective of our project was investigation of electric carriers dynamics of TI in extremely thin layers and in close proximity to metallic interface, in case of our project with Fe layer. Finding the correlation between structure and physical functionality of such junctions is crucial for fundamental understanding of the physical processes behind the spin transport as well as application in new technology. Most of our samples were grown on Muscovite mica, which allowed us to efficiently grow monocrystalline layers of topological insulator Bi_2Te_3. This substrate aside of providing optimal conditions for growth of the films also provides excellent thermal and electric insulation of grown layer, with excellent optical properties which are crucial for time-resolved femtosecond laser spectroscopy. For the processes of growth Bi pieces of purity 99.999% (Aldrich Chem. Co.) and spectrographically standardized Te ingots (Johnson Matthey Chemicals) were used as a deposition sources in standard effusion cells in all discussed processes of growth. The Fe wire of purity 99.999% (Aldrich Chem. Co.), was evaporated with electron cell. The deposi-

Table 3.1: Characteristics of growth of the samples.

Name	Substrate	Plane	Substrate temp. $[^oC]$	*Bi* dep. rate	*Te* dep. rate	Thickness
A_1	Mica	(110)	$120°C$	0.0145 Å/s	0.0210 Å/s	15 *nm*
A_2	Silicon	(001)	$130°C$	0.0090 A/s	0.0380 A/s	10 *nm*
A_3	Silicon	(001)	$130°C$	0.0140 A/s	0.0200 A/s	10 *nm*
B_1	Mica	(110)	$120°C$	0.0145 Å/s	0.0210 Å/s	15 *nm*
B_2	Mica	(110)	$120°C$	0.0145 Å/s	0.0210 Å/s	15 *nm*
C_1	Mica	(110)	$120°C$	0.0145 Å/s	0.0210 Å/s	15 *nm*
C_2	Mica	(110)	$120°C$	0.0145 Å/s	0.0210 Å/s	15 *nm*

tion process was held under ultra-high vacuum conditions, the pressure during the growth did not exceed the level of $5 \cdot 10^{-9}$mbar.

Sample A1 - reference sample - was made with a standard technique described in our previous works. That is the Muscovite mica with (110) plane which was cleaved and mounted on standardized sample holder for resistive heating from PREVAC company and inserted into to the system. After introduction into the vacuum environment, holder was slowly reheated to 120^oC in order to degas it and remove the impurities that might be stuck on the surface. After the primal cleaning, the temperature of the substrate was risen up to 250^oC for at least 1h to completely remove any remaining residue and reorganized the surface. The substrate was then left at 120^oC for at least 12h. The temperature during the deposition process was kept at 120^oC. The rates of the Bi and Te vapour flux were controlled with quartz crystal microbalance, and were kept at 0.0145Å/s for bismuth and 0.0210Å/s for tellurium, which gives a correct ratio of 2:3 structure of Bi_2Te_3. The total flux of the molecular beam was 0.0355Å/s, such flux was maintained for the duration of 1h 15min to achieve 15nm layer of the Bi_2Te_3. Layer after the deposition was left at 120^oC over night to reorganise its crystal structure.

Sample A2 - polycrystalline sample on silicon - sample was prepared according to the tech-

nique described by Rapacz et.al. The silicon wafer was cut with a diamond pen and cleaned in solution of isopropanol in ultrasound bath. After that, it was reheated on the hotplate up to 200^oC for an hour, then the substrate was mounted on standardized sample holder for resistive heating from PREVAC company and inserted into to the system. After introduction into vacuum environment, holder was slowly reheated to 130^oC in order to degas it and remove the impurities that might be stuck on the surface. The substrate was then left at 130^oC for at least 12h. The temperature during the deposition process was kept at 130^oC. The rates of the Bi and Te vapour flux were kept with quartz crystal microbalance, and were maintained at 0.0090Å/s for bismuth and 0.0380Å/s for tellurium. The total flux of the molecular beam was 0.0370Å/s, such flux was maintained for the duration of 35min to achieve 10nm layer of Bi_2Te_3. Layer, after the deposition, was left at 100^oC over night to reorganise its crystal structure.

Sample A3 - polycrystalline sample on silicon - sample was prepared according to the technique described by Rapacz et.al. The silicon wafer was cut with a diamond pen and cleaned in solution of isopropanol in ultrasound bath. After that it was reheated on the hotplate up to 200^oC for an hour, then substrate mounted on standardized sample holder for resistive heating from PREVAC company and inserted into to the system. After introduction into vacuum environment, holder was slowly reheated to 130^oC in order to degas it and remove the impurities that might be stuck on the surface. The substrate was then left at 130^oC for at least 12h. The temperature during the deposition process was kept at 130^oC. The rates of the Bi and Te vapour flux were maintained with quartz crystal microbalance, and were kept at 0.0140Å/s for bismuth and 0.0200Å/s for tellurium. The total flux of the molecular beam was 0.0340Å/s, such flux was maintained for the duration of 50min to achieve 10nm layer of Bi_2Te_3. Layer, after the deposition, was left at 100^oC over night to reorganise its crystal structure.

Sample B1 - step sample Fig.3.7. - was made with standard technique with slight modification. Mica substrate, in order to achieve better quality of the surface, was separated with scotch tape to ensure lack of additional terraces and perfectly smooth substrate with orientation (110). After this substrate was mounted on standardized sample holder for resistive

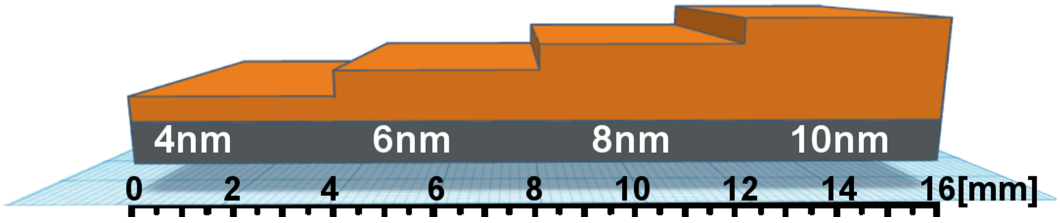

Figure 3.7: Sample B1 - art view of monocrystaline sample of Bi_2Te_3 with terraces' thickness of 4, 6, 8 and 10nm .

heating from PREVAC company and inserted into to the system. After introduction into vacuum environment, holder was slowly reheated to 120^oC in order to degas it and remove the impurities that might be stuck on the surface. After the primal cleaning the temperature of the substrate was risen up to 250^oC for at least 1h to completely remove any remaining residue and reorganized the surface. The substrate was then left at 120^oC for at least 12h. The temperature during the deposition process was kept at 120^oC. The rates of the Bi and Te vapour flux were controlled with quartz crystal microbalance, and were kept at 0.0145Å/s for bismuth and 0.0210Å/s for tellurium, which gives a correct ratio of 2:3 structure of Bi_2Te_3. The steps on the sample were achieved by creating the shadow over the substrate with integrated manipulator within the MBE chamber. The procedure to achieve the step structure was as follows: after the stabilization of the effusion cells, the total flux was kept at 0.0355Å/s, at which point both shutters were opened to substrate plate; after 19min, the mechanical shutter was shifted by 4mm, in order to stop the growth over the region with 4nm step; after each 19min, the mechanical shutter was shifted by another 4mm up to the layer with 10nm of thickness at which point after the elapsing of 19 minute mark, the effusion cells where covered. Layer after the deposition was left at 120^oC over night to reorganise its crystal structure.

Sample B2 - wedge sample Fig.3.8 - was made with standard technique with a slight modification. Mica substrate, in order to achieve better quality of surface, was separated with scotch tape to ensure lack of additional terraces and perfectly smooth substrate with orien-

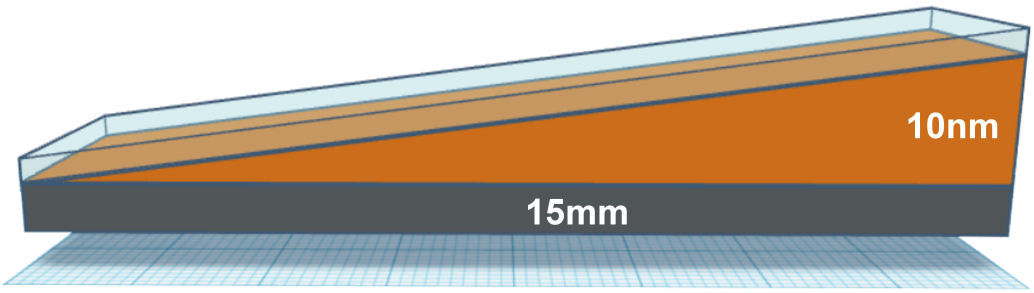

Figure 3.8: Sample B2 - art view of monocrystaline wedge of Bi_2Te_3 with slope of 0.66nm/mm.

tation (110). After this, substrate was mounted on standardized sample holder for resistive heating from PREVAC company and inserted into to the system. After introduction into vacuum environment, holder was slowly reheated to 120^oC in order to degas it and remove the impurities that might be stuck on the surface. After the primal cleaning, the temperature of the substrate was risen up to 250^oC for at least 1h to completely remove any remaining residue and reorganized the surface. The substrate was then left at 120^oC for at least 12h. The temperature during the deposition process was kept at 120^oC. The rates of the Bi and Te vapour flux were maintained with quartz crystal microbalance, and were kept at 0.0145Å/s for bismuth and 0.0210Å/s for tellurium, which gives a correct ratio of 2:3 structure of Bi_2Te_3. The procedure to achieve the wedge sample was as follows: after the stabilization of the vapour flux at 0.0355Å/s, the mechanical shutter was moved with the motor with speed of 0,005mm/s during the time of 47min until the sample was completely covered by the shutter and we achieved the maximal thickness of 10nm; due to this procedure it was possible to get a sample with gradient of thickness 0,66 nm/mm; layer, after the deposition, was left at 120^oC over night to reorganise its crystal structure.

Sample C1 - iron oxide cover - sample was made with the standard technique the same way as described for sample A1. The temperature during the deposition process was kept at 120^oC.

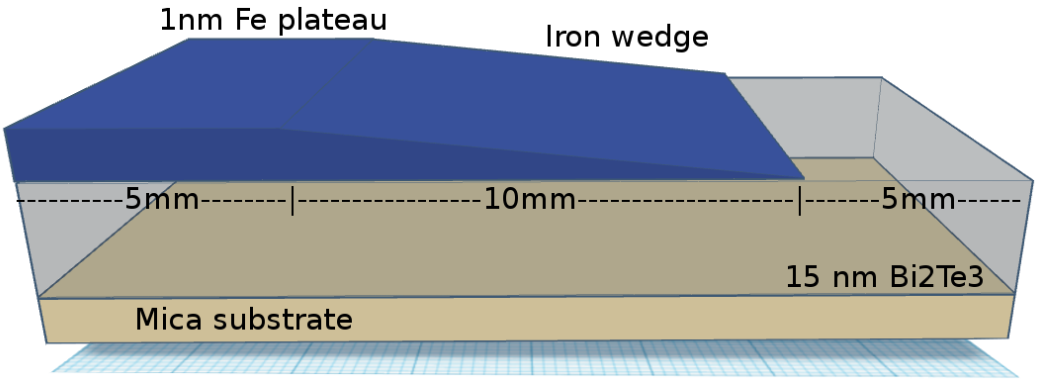

Figure 3.9: Sample C2 - art view of monocrystaline sample of Bi_2Te_3 with 3 sections: 1st - plateau of iron with a thickness 1nm and lenght 5mm; 2nd - wedge of iron with gradient 1Å/mm; 3rd - free surface sample of BT.

The rates of the Bi and Te vapour flux were maintained with quartz crystal microbalance, and were kept at 0.0110Å/s for bismuth and 0.0160Å/s for tellurium, which gives a correct ratio of 2:3 structure of Bi_2Te_3. The total flux of the molecular beam was 0.0270Å/s, such flux was maintained for the duration of 1h 30min to achieve 15nm layer of the Bi_2Te_3. Layer after the deposition was left at 120^oC over night to reorganise its crystal structure. After one day, layer of iron was deposited on half of the clean Bi_2Te_3 surface. Iron was deposited at the rate of 0.063Å/s during the time of 160s, which resulted with capping layer of iron with thickness 1nm.

Sample C2 - iron oxide wedge Fig.3.9 - sample was made with the standard technique the same way as described for sample A1. The temperature during the deposition process was kept at 120^oC. The rates of the Bi and Te vapour flux were controlled with quartz crystal microbalance, and were kept at 0.0137Å/s for bismuth and 0.0201Å/s for tellurium, which gives a correct ratio of 2:3 structure of Bi_2Te_3. The total flux of the molecular beam was 0.0338Å/s, such flux was maintained for the duration of 1h 15min to achieve 15nm layer of the Bi_2Te_3. Layer after the deposition was left at 120^oC over night to reorganise its crystal structure. After

one day, iron plateau and wedge were deposited on top of the Bi_2Te_3 leaving 5mm wide region without iron for comparison. The rate of iron was kept at 0.00872Å/s during 19min, during this time automated manipulator was exposing the layer to create the wedge sample with a speed 0,0087mm/s.

3.4 Summary

By employing molecular beam epitaxy we successfully created high quality ultra thin films of Bi_2Te_3 that allowed us to tackle different questions concerning the properties of this material. Samples from the group A consist of three samples one deposited on Muscovite Mica and two deposited on Silicon (001). During their growth we used different rates of the molecular beam flux, as well as different temperatures of growth. That gave us the opportunity to see how the change of this parameters influences the quality of grown material as well as probe the electron-phonon coupling and phonon dynamics that may play a crucial role in development of future devices [27, 28].

The second group B of thin film was created for better understanding of the critical thickness of the Bi_2Te_3 [9, 31, 32, 33]. In order to answer this question, we prepared two samples deposited on Muscovite Mica with different geometry: one with large steps (that grants us an access to large surface area with uniform thickness) and second one with continuous slope (that allows us to conduct experiments with higher number of investigated spots). We believe that such geometries are optimal for investigation of the critical thickness influence on the behaviour of photo-excited hot carriers as well as give us opportunity to better understand the growth process of the material.

The last group C of the synthesized films was made in order to understand the chemical reactions and physical phenomena induced by the proximity to the oxidized iron layer [34]. Due to large interest of the community in creation of devices based on the topological insulator

phenomena [5, 6, 7], it is crucial to understand the basic interactions (both chemical and physical) of materials showing this effects in close proximity to other non-trivial, in topological sense, interfaces. In our study we have chosen the iron oxide as the covering layer and we have created two samples one with uniform thin cap of iron ($\sim 1nm$) covering half of the sample and second, similar to sample B2, with uniform continuous wedge of iron ($1nm \rightarrow 0nm$) deposited on $15nm$ layer of Bi_2Te_3. Such configuration gives us means to directly compare the effects induced by the presence of other material on both crystal structure as well as phonon and hot carrier dynamics. Using half of the sample as the reference we can eliminate effects that could be induced by different growth conditions and give us chance to directly compare the measured signals.

Chapter 4

Diffraction and continuous spectroscopy techniques

In this chapter we will focus on continuous spectroscopy techniques used to characterize the samples of Bi_2Te_3. We will describe as well the techniques that were used for characterization of our samples and we will discuss the most interesting results.

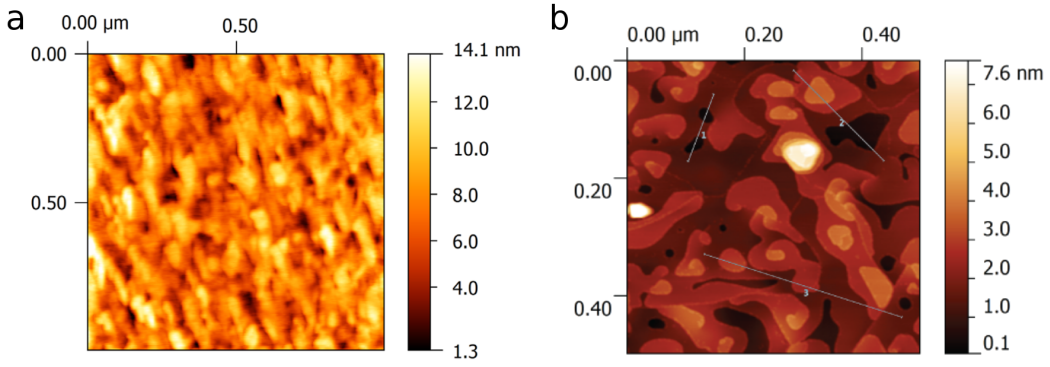

Figure 4.1: a -1 $\times$ 1μm AFM image of sample A2, Bi_2Te_3 grown on Si(001). b - 0.45 $\times$ 0.45μm AFM image of sample A1 grown on Muscovite mica (110). From R.Rapacz [30]

4.1 Surface structure analysis

One of the leading fields in modern physics is surface structure analysis, especially at nanoscale. In our arsenal we now posses a broad spectrum of different ways to characterize physical aspects of this region. One of the most prominent group is definitely the scanning probe microscopy (SPM) with atomic force microscopy (AFM) technique and scanning tunnelling microscopy (STM). The resolution of those microscopes is not limited by diffraction, but mostly by the size of the probe-sample interaction volume. Hence the ability to measure small local differences in object height like 1nm steps on Bi_2Te_3 (Fig.4.1.b). Unlike electron microscopy methods, some modes in this group do not require a partial vacuum but can be efficiently be used in air. But the most prominent advantage of this type of measurements is a wide diversity of techniques, which allow additional characterizations of measured samples. For example, we can measure local conductivity or magnetic and ferroelectric domain structure.

Second group of methods, widely used for surface characterization, are different kinds of electron diffraction methods, which provide us with information about crystal order in measured samples. To this group belong LEED and RHEED techniques, that were used in our

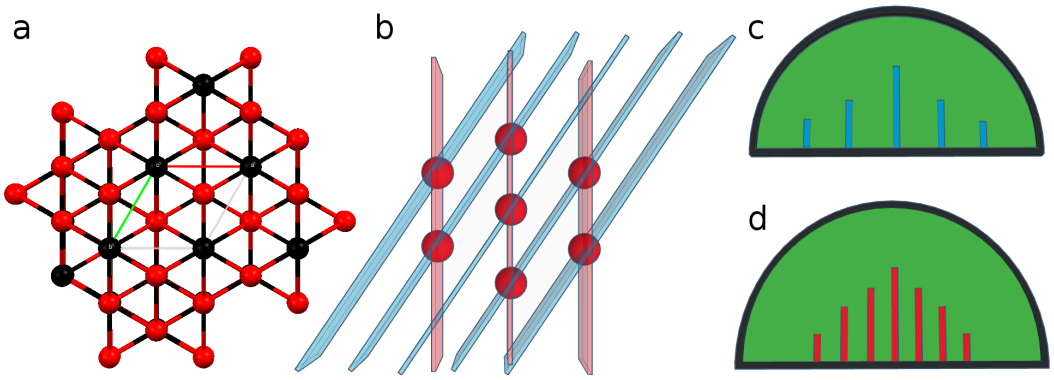

Figure 4.2: a - View on the c plane (001) of Bi_2Te3 cell. b - Two main symmetry planes in hexagonal cell, difference between them is exactly 30^o. c and d - Artistic representation of diffraction pattern made with RHEED along two main symmetries, colors are corresponding to the planes marked in picture b, the received pattern is in reciprocal lattice.

experiments. Low energy electron diffraction is based on the detection of diffracted electrons from collimated monoenergetic beam. The image is created by electrons elastically scattered back towards the electron source. The spatial distribution of the intensity maxima is determined strictly by the surface structure. Positions of the intensity maxima correspond to the lattice structure of the surface represented in reciprocal space.

4.1.1 Reflection high-energy electron diffraction (RHEED)

Reflective high energy electron diffraction method give us information about long range order of the sample surface in the plane perpendicular to the beam incidence plane. Namely if sample is monocrystalline or polycrystalline or posses some kind of texture. Additionally RHEED can be employed in measurement of thickness of samples grown in MBE chamber. RHEED because of its small penetration depth, caused by the interaction between incident electrons and atoms, is mainly sensitive to the atomic structure of the first few planes of a crystal lattice. This feature is especially useful for quick identification of grown film, for example

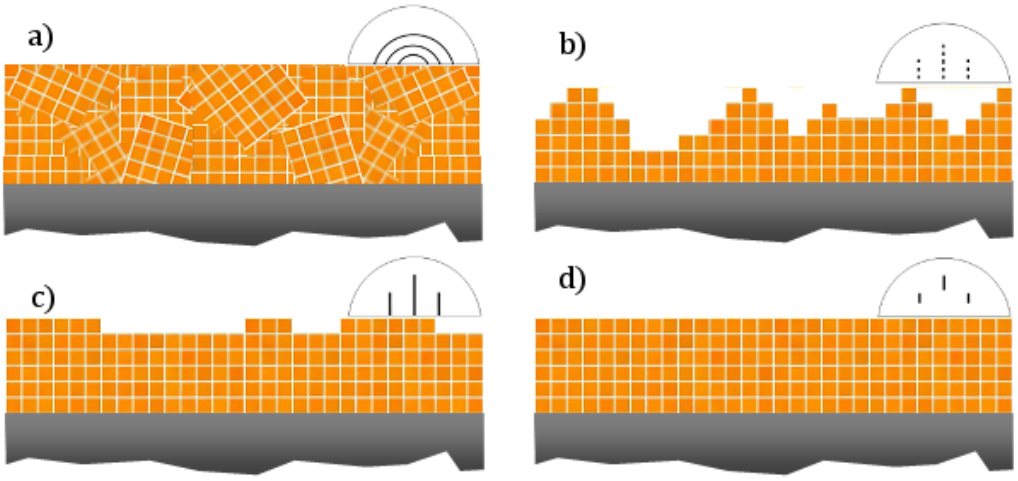

Figure 4.3: RHEED diffraction image from: a) Polycrystalline sample; b) Monocrystalline sample with additional 3D structures (for example islands or quantum dots); c) Monocrystalline structure with small terraces; d) Monocrystalline and perfectly flat structure .

(Fig.4.2) hexagonal structure of Bi_2Te_3 possess two characteristic RHEED patterns, which differ from each other by 30° rotation, what in result creates 60° repetition of each pattern.

Because of RHEED geometry incident beam is directed at a low angle to the surface and has a very strong effect on both the diffraction and its interpretation. When the atomic defects are parallel to the incident beam direction they can produce large changes in both the measured intensity and the shape of the diffracted beams, for example, atomic steps (Fig.4.3.c). In contrast, atomic structure in the diffracted intensity is mainly determined by the atomic structures perpendicular to the incident beam. Both of those phenomena are originating from very low glancing angle of the incidence beam.

Additionally, RHEED diffractometer can detect intensity changes of diffracted electron during the growth of the layer in MBE chamber, that can be used to follow in time the thickness of deposited layers. Our experiments, using this technique, have shown linear changes with a lack of any periodicity accustomed with Frank van der Merwe crystal growth (the growth

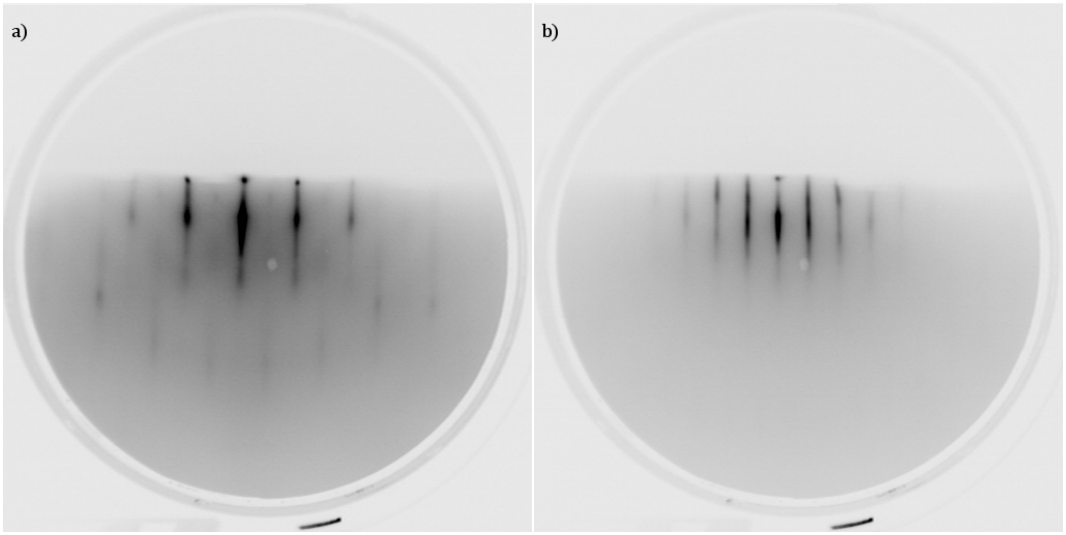

Figure 4.4: RHEED diffraction image of sample A1 along two main planes of symmetry characteristic to Bi_2Te_3 hexagonal crystal structure. Detected streaks are proof of monocrystalline terrace growth of the sample.

layer by layer). This result pointed us in two possible mechanism of growth of our samples that is either Volmer Weber (growth in island formations) or Stranski-Krastanov (mixed) crystal growth dynamic [42].

All samples were measured on RHEED from STEIB Instruments in situ environment, just after the growth of the samples. The analysis was performed with RHEED Vision v5.6.6 software. Sample A_1 diffraction image Fig.4.4 shows characteristic symmetries of hexagonal structure (difference of 30°), and appearance of streaks suggests high quality surface, similar to all samples from group B and C. Received results are a direct proof that technique, employed during the growth, is optimal for creation of very smooth and monocrystalline thin films of Bi_2Te_3. Samples, grown on silicon substrate A2 Fig.4.5.a and A3 Fig.4.5.b, exhibit formation of polycrystalline structure, which is mainly caused by mismatch between Bi_2Te_3 and silicon (001). Film A_3 possess additional streaks, which suggest creation of some long range ordering on the film. Both groups of samples B and C were grown with the same parameters of growth

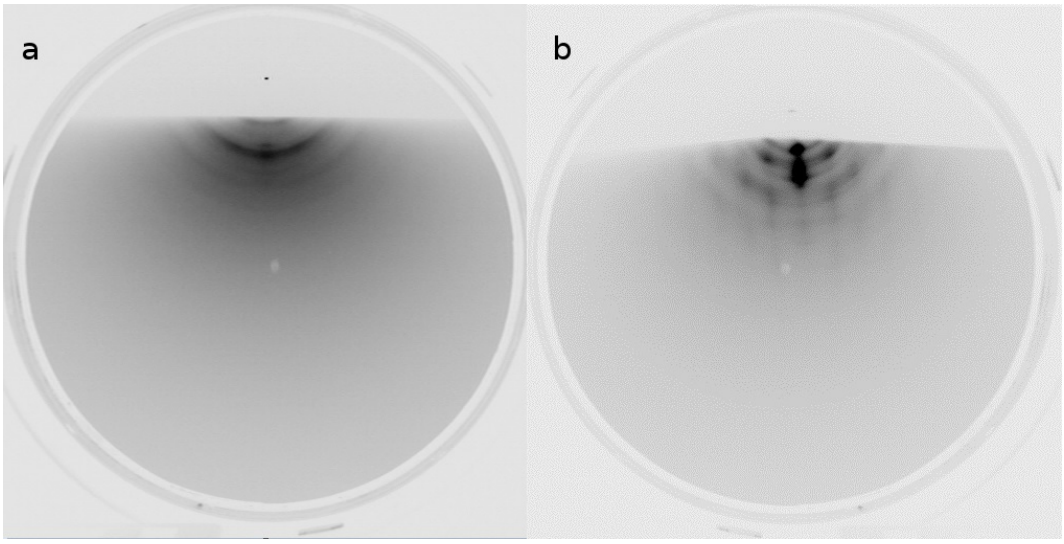

Figure 4.5: RHEED diffraction image of sample a - A2 and b - A3. Observed half circles are proof polycrystalline growth of the sample.

as the sample A1. In case of sample B2 Fig.4.6.a, we can observe similar streaks corresponding to one of the characteristic diffraction patterns of hexagonal crystal. The broadening is caused by the presence of planned steps in the structure. For both samples B1 and B2, due to their unique configuration with changing thickness and placement on the sample holder, it was impossible to get image from all the angles. In case of samples from batch C, they all showed uniform single crystalline structure of Bi_2Te_3 with smooth terraces of nm height Fig.4.6.b This is a proof of deposition quality repeatability using the method developed by our group.

4.1.2 Low energy electron diffraction (LEED)

LEED (low energy electron diffraction) is a technique in which beam of electrons, ejected from an electron gun, probes measured sample. Main components of the LEED are electron gun and fluorescent screen on which we observe registered diffraction patterns. Electron gun consists of two main parts, first is the heated cathode which is an emitter of electrons and

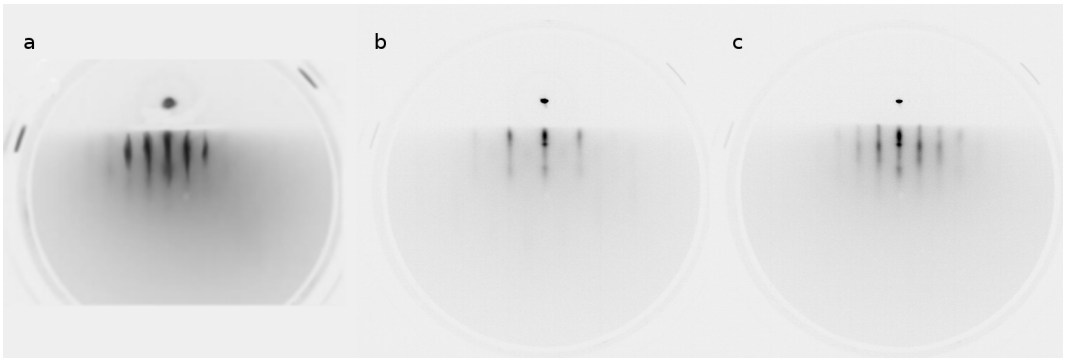

Figure 4.6: a - RHEED diffraction image of sample B2 along main planes of symmetry characteristic to Bi_2Te_3 hexagonal crystal structure. Observed streaks are proof of monocrystalline terrace growth of the sample. b and c - RHEED diffraction image of sample C2 along two main planes of symmetry characteristic to Bi_2Te_3 hexagonal crystal structure. Observed streaks are proof of monocrystalline terrace growth of the sample.

second, the array of focusing lenses. Such configuration allows to generate collimated beam of electrons with finely defined energy in range $20-300eV$, which are then scattered in numerous different directions strictly dependant on the surface crystallography. After the diffraction, electrons go through 3 different grids before arriving to the phosphor covered screen. First of those grids is grounded and acts as a shielding for the second one. Second is a filter which passes only electrons with enough of energy. Thanks to that electrons with lower energy, the image does not cloud or distort. The final grid acts as a barrier between negatively charged 2nd grid and positively charged screen. After that, electrons land on the screen creating a glow which intensity is strictly dependant on intensity of the arriving electrons. Pattern, created by those electrons, is an image in reciprocal space of measured structure.

LEED is one of the primary techniques in surface physics for determination of grown structures. We can distinguish two ways in which we can analyse acquired data. First one used in this work is analysis of the position of spots on the diffraction pattern. This method give us information about symmetries, size and rotational alignment of unit cells of our samples.

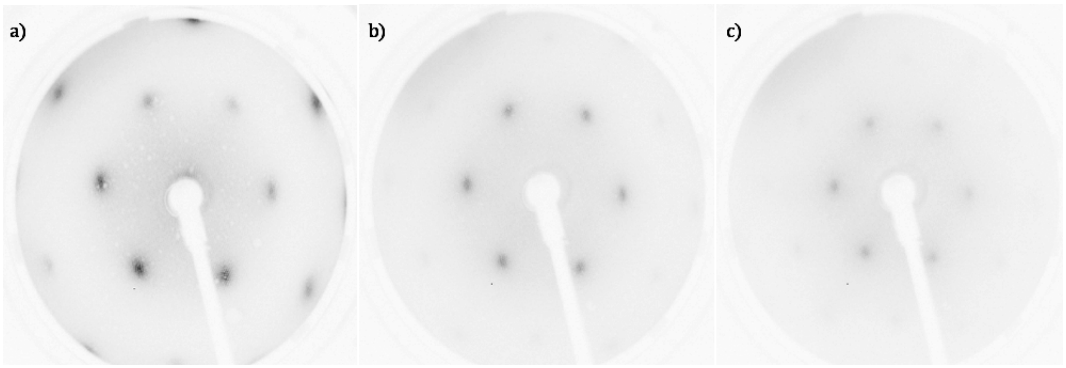

Figure 4.7: LEED diffraction image of sample A1 at different electron incident energies a) 56eV; b) 75eV; c) 98eV.

Second one is the analysis of acquired spots intensities recorded as a function of incident electron beam energy. This allows to generate so called I-V curves which can be directly compared with theoretical models giving in result accurate informations about atomic positions in unit cell of the measured sample.

All described LEED measurements were preformed in situ environment, in short span of time after the thin film deposition, on INTEGRALEED model BDL800IR-LMX-ISH. Samples A2 and A3, because of their polycrystalline structures, did not give any diffraction images. Fig.4.7. shows diffraction pattern of sample A_1. Conducted experiment has proven that grown structure posses correct Bi_2Te_3 hexagonal structure. Slight diffusion of diffraction points might be caused by slight mismatch between quintuple layers. Sample C_2 (Fig.4.8.) made with the same technique as sample A1 shows similar diffusion of diffraction points which might be characteristic for this method of growth. During this experiment it was possible to observe ordered structure at very low and high energy (up to $200eV$). Above this high energy region diffraction spots were vanishing. Ability to observe diffraction spots to such energies proofs correct and monocrystalline structure of grown thin film underneath the topmost atomic layers.

LEED images have provided us with very clear information about formation of crystal structure in case of our growth method. Deposition of the sample with evaporation rates,

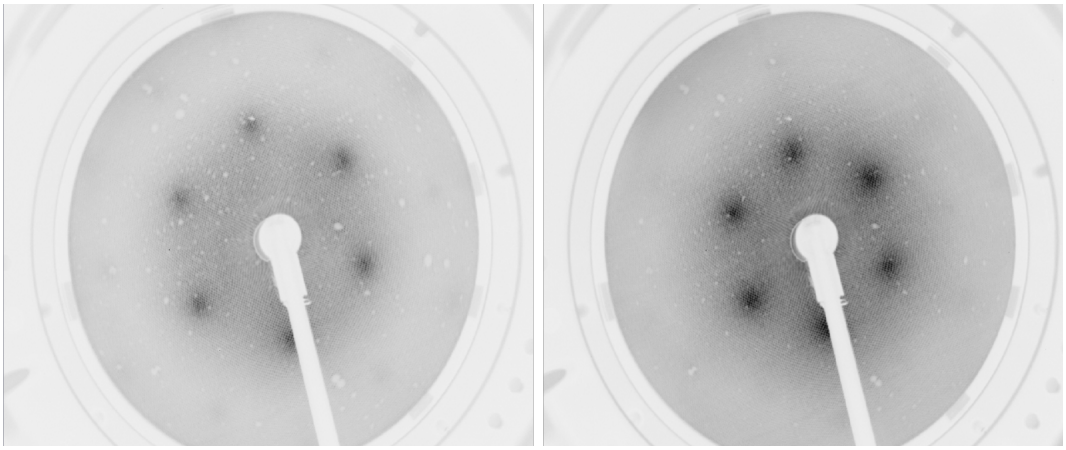

Figure 4.8: LEED diffraction image of sample C3 reviling characteristic Bi_2Te_3 hexagonal crystal structure. Broadening of the diffraction spots is a result of slight mismatch between nearest QL's.

similar to desired composition stoichiometry but with lower temperature of substrate, causes slight mismatch between nearest QL's but on the other hand, gives us very fine formation of Bi_2Te_3 structure.

To further analyse the nature of the crystal formation we performed the low energy electron diffraction experiments on the step layer sample B2 in order to confirm proper growth of the crystalline layer. A detailed LEED image on a 5 nm thick film is shown in Fig.4.9.a. Measurement confirmed the proper symmetry structure of the thin layer. In the region of 4nm thickness image started to become distorted because of the bending of the mica substrate.

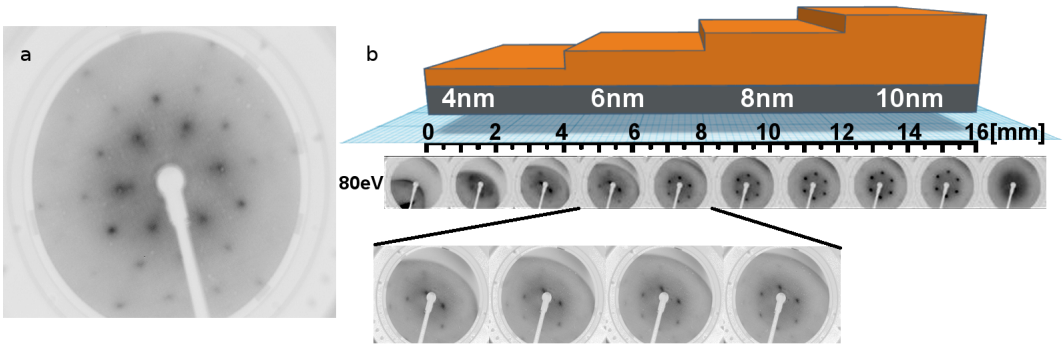

Figure 4.9: a - LEED of 5nm thickness sample at energy 115eV. b - Art view of the cross section of the step sample B2 with an inset in the bottom of the figure showing thickness dependence of LEED image obtained at energy 80eV.

4.2 Chemical and electron state analysis

In order to fully understand the physics hiding behind so complicated material like Bi_2Te_3, we need to have well defined samples. During the process of growth, the control over the rates of deposition is not always exactly the same, and the stoichiometry of deposited film can vary even when using exactly the same parameters. Even a slight variations in the ratio of bismuth to tellurium can cause self doping of the material, and their polarity can be changed from p-type to n-type by increasing bismuth concentration in the film [45]. The ability of self doping of Bi_2Te_3 is used in industry to better harness its thermoelectric properties [46, 47, 48, 49].

Because of this property and a direct modification of electron levels due to it, it is crucial to well characterize chemical state of each sample. In our case each sample was thoroughly measured with X-ray photo-emission spectroscopy. We put a special focus on investigating the changes in valence band and $Bi4f$ and $Te3d$ core level energy shift.

4.2.1 X-ray photo-electron spectroscopy

The photo-electron spectroscopy is one of the few methods which allows direct characterization of electronic and chemical states of the elements that exist inside the measured material. Emitted electron possess very shallow penetration of measured sample, usually in range of $0.5nm$ up to $2nm$. We can distinguish two separate methods by the energy of excited photons. Ultra-Violet Photo-electron Spectroscopy ($h\nu = 10 - 150eV$) and X-ray Photo-electron Spectroscopy ($h\nu = 150 - 3000eV$). Because binding energy decreases with the distance from nucleus, UPS method is only used for characterization of valence band electrons, while XPS method can be employed for characterization of both core level electrons and valence band electrons.

In principle, the PES method works by excitation of sample with radiation with specific energy $h\nu$, and absorption of a photon by the material, followed by the transfer of its total energy to an electron. Changing the state of the electron from $|i>$ to the state $|j>$:

$$h\nu = E_j - E_i$$

Then, if the emitted electrons energy E_j is larger than the work function barrier ϕ excited electron can be emitted into the vacuum. Kinetic energy E_k of this particle is then measured with energy analyser and is given by the Einstein equation:

$$E_k = h\nu - \phi - E_B$$

Work function ϕ is characteristic for each spectrometer and can be considered as constant, but the binding energy E_B of electrons depends on type of atom from which electron was irradiated as well as local chemical environment. Because each element possess characteristic structure of atom, measurement of E_B can be used for identification of elements and their chemical states in samples. Approximation of this energy (for multielectron atoms) is given by the quantum mechanics.

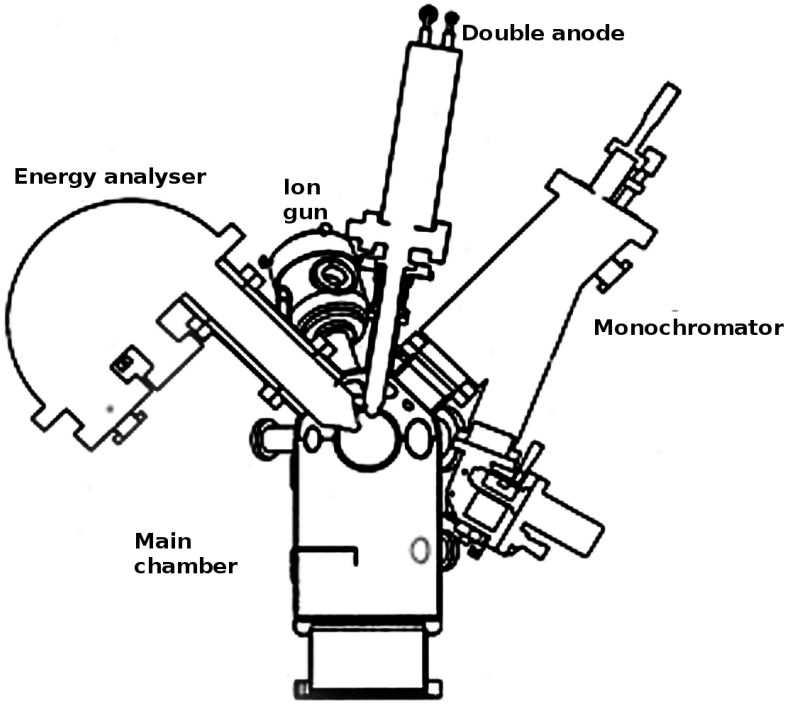

Figure 4.10: Schematic of *PhysicalElectronicsPHI*5700 spectrometer.

Samples group A

Conducted photo-electron spectroscopy studies were performed with the use of the monochromatized AlKα radiation using the PHI 5700 spectrometer from Physical Electronics Fig.10. All film after growth have been transferred in UHV from the MBE to the analysis chamber within minutes after deposition. The films studied in-situ showed no oxidation nor carbon contamination. The analysis spot had the diameter of 0.8 mm. The analysis of the spectra was done with the use of MULTIPAK program from Physical Electronics. The lines were fitted by Gaussian-Lorentz or asymmetrical lines. The same program was used to calculate the atomic concentration. During the measurements we obtain the photo-electron spectra of $Bi4f_{7/2}$ and $Te3d_{5/2}$ core levels, as well as general spectra in order to check the purity of grown films.

Analysis of XPS spectra allowed to determine the atomic composition and chemical state of the components (Table 4.1). All samples appear to be free of any contamination and the atomic composition characterized by the Bi/Te ratio spans from 33/67 (B_2) to 46/54 (A_1). The Bi_xTe_y system is known to form many layered nanostructures especially for the compositions $y/x < 3/2$, in witch stacking sequence of the quintuple layers has additional interlayers of Bi and Te located in-between the BT QL's [50].

The calculations, together with the analysis of core levels, indicate that at the used growth conditions main phase of Bi_2Te_3 is formed with some addition of Te. In samples A_2, A_3 we observed existence of two chemical states of Te, which can be associated to pure Te and the second one to the chemical state of Bi-Te compound. The observed chemical shifts (Table 4.1) exhibit similar trends for all examined films. The maximum of the $Bi4f_{7/2}$ peak is shifted, relatively to pure bismuth layer, towards higher binding energies while the $Te3d_{5/2}$ line is shifted towards lower binding energies compared to pure Te film. The high-binding- energy $Bi4f_{7/2}$ states observed for the film A_1 at 157.31 eV, up to 157.56 eV for the film A_3 and are in close agreement with those reported by R. Rapacz [30]. Good agreement with those energies can

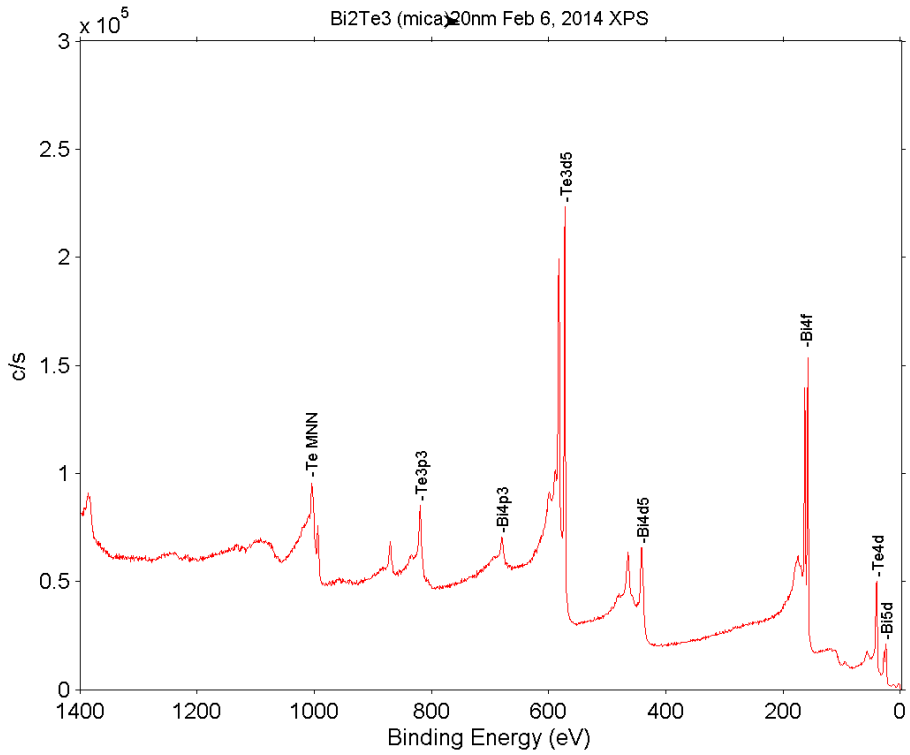

Figure 4.11: Typical XPS spectra of pure Bi_2Te_3 sample.

Table 4.1: Summary of the atomic concentration calculations derived from the XPS data.

Sample	$Bi4f_{7/2}$			$Te3d_{5/2}$		
	Low_{Be} state	$High_{Be}$ state		Low_{Be} state	$High_{Be}$ state	
	E_B [eV]	E_B [eV]	**At [%]**	E_B [eV]	E_B [eV]	**At [%]**
Tellurium	-	-	**-**	-	572.80	**100**
A_1	-	157.31	**46**	571.93	-	**54**
A_2	-	157.52	**35**	572.10	572.80	**65**
A_3	-	157.56	**33**	572.11	572.88	**67**
Bismuth	156.85	-	**100**	-	-	**-**

be also observed for the $Te3d_{5/2}$ band. The low- binding-energy state spans from 571.93 eV for film A_1 up to 572.11 for film A_3. Observed states of the main peaks of Te and Bi indicate formation of Bi_2Te_3.

Samples group B

As previously for group A the $Te3d_{5/2}$ and Bi 4f doublets and valence band were used for analysis of proper formation of the Bi_2Te_3 structure. On Fig.4.12 we presented the valence band where it is clear that thickness of the film does not influence considerably this part of the electronic structure but leads to shift of the energy ($\sim 0.2eV$). Obtained spectra for core levels of $Te3d_{5/2}$ doublet (Fig.4.13.a) shows lack of distortion induced by the thickness, while for the $Bi4f_{7/2}$ level a small contribution from metallic Bi could be detected after fitting of the spectra for the films with thickness up to 8 nm. Fig.4.14 shows the example of the results of fitting for the 6 nm film. This fact correlates with the obtained atomic concentration which is rich in Bi, especially for the thickness of 4 and 6 nm:

Atomic concentration of grown films

Thickness	Tellurium	Bismuth
4 nm	49,5	50,5
6 nm	52,4	47,6
8 nm	52,1	47,9
10 nm	53,2	46,8

One of the possible reasons of the Te deficiency changing with the thickness of the films could be related with the desorption of Te at the initial stage of growth. According to the literature formation of additional Bi layers between QLs is a consequence of that process. The super-structure Bi-BT conserves the stable structure within the QLs [51]. The Te desorption may be

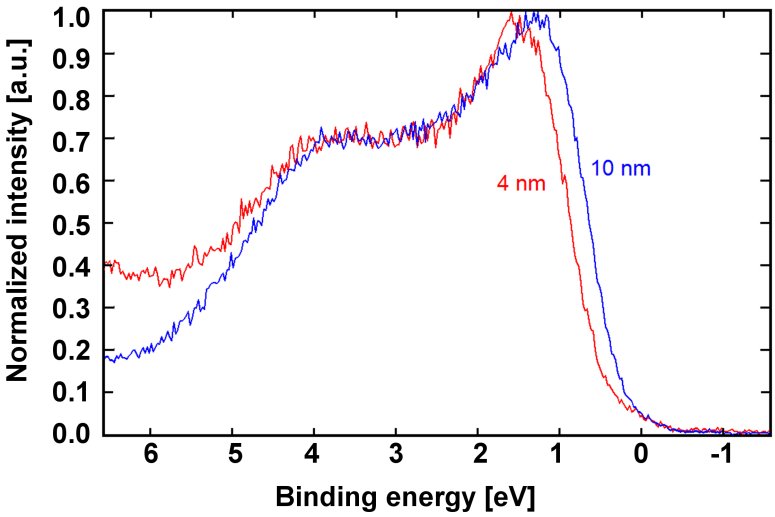

Figure 4.12: Valence band spectra for the as grown film with various thickness.

related to latent heat of the compound formation which causes overheating of the deposited film. The effect will be most pronounced at the thinnest films, because the heat transfer to the substrate is limited and the mass of the deposited BT is very low. The interface BT-mica has the van der Waals character limiting the heat transfer to the substrate.

Another important issue is related to the fact that the optical measurements were performed ex-situ, for the samples oxidized at the surface. In order to estimate the effect of surface oxidation, we performed the XPS analysis few months after the growth. The analysis has shown that even for the thinnest part of the sample we could observe in the photo-emission core level spectra the contribution from the unaffected BT compound with characteristic position of the Te and Bi lines (Fig.4.15). The remains of the Bi interlayers could also be detected for the films 4 and 6 nm thick. The oxides formed on the surface are mostly Bi_2O_3 and TeO_2. For the thinnest films, a small contribution with higher binding energy than for TeO_2 was observed indicating to TeO_3.

To estimate the thickness of the oxide layer, we used the formula that takes into account photo-emission intensity damping [51]:

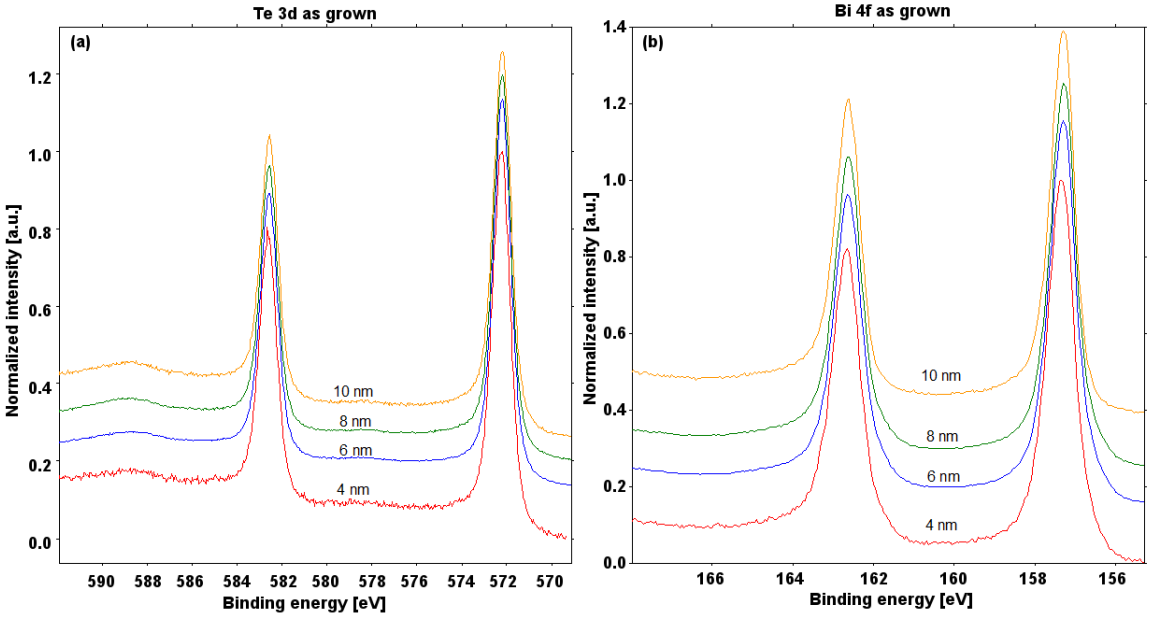

Figure 4.13: XPS $Te3d_{5/2}$ a and $Bi4f_{7/2}$ b doublets for the as-grown films.

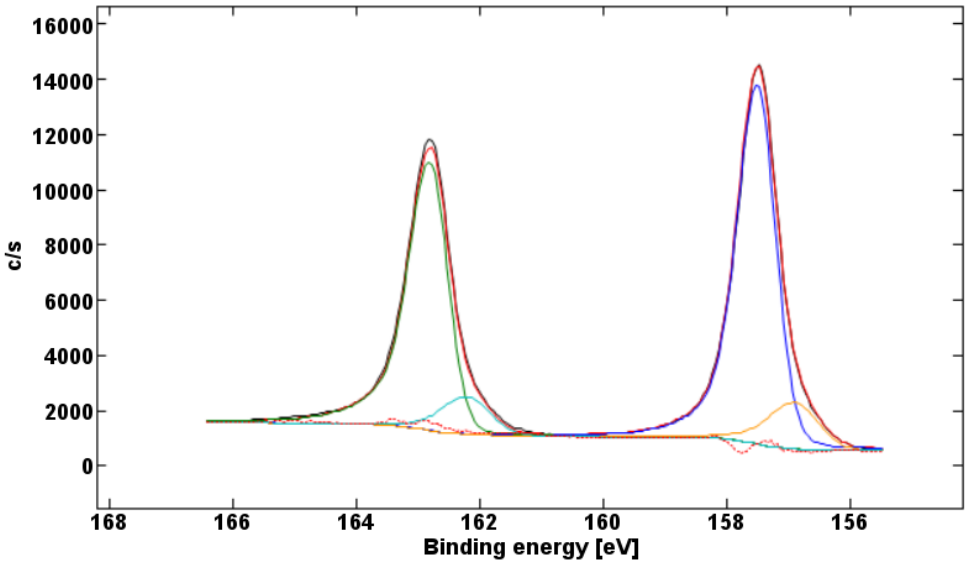

Figure 4.14: Fit of the $Bi4f_{7/2}$ doublet for the 6 nm thick film showing the contributions from the Bi_2Te_3 (high intensity doublet) and Bi (low intensity doublet).

$$\frac{I_C}{I_F} = \frac{I_{C_0}\left[1 - exp\left(\frac{-d}{\lambda_C cos\Theta}\right)\right]}{I_{F_0} exp\left(\frac{-d}{\lambda_F cos\Theta}\right)}$$

The intensity ratio from the oxide cap layer I_C and the main film I_F can be expressed with the use of the thickness of the cap layer d and inelastic mean free path within the basic film and the cap layer. The analysis angle was 45°.

The photo-electron mean free path λ can be estimated using the TPPM2M formula in the Quases program of S. Tougaard [52, 53, 54]. Performed calculations showed formation of about 1.75 nm of TeO_2 and 2.25 nm for Bi_2O_3. We calculated the relative intensity of the photo-emission components coming from oxides and BT. Size of the oxidised layer changes with the thickness, while for thin films of 4 and 6 nm the intensity ratio of oxide to BT is between 3 and 6, for the thicker films it is around 1.8.

When assuming uniform cap layer of mixed Bi and Te oxides one can calculate the thickness of the oxide film. Mean free path of about 2 nm was taken to the formula:

$$d = \lambda cos\Theta ln\left(\frac{I_C}{I_F} + 1\right)$$

where we applied assumption $I_{C_0}/I_{F_0} = 1$. The calculated thickness of the oxide layer varies from about 2.2 nm for thin films to about 1.4 nm for the films with thickness 8 and 10 nm.

Atomic concentration for the oxidized films

Thickness	Tellurium	Bismuth	C	O
2 nm	8.3	9.3	45.0	37.4
4 nm	10.5	11.0	41.1	37.4
6 nm	12.2	13.0	40.9	33.9
8 nm	9.5	10.2	47.7	32.8

Surprisingly the AFM studies of the oxidized sample showed higher roughness for the thicker films. It may be related to the Stransky-Krastanov way of BT growth leading to the increased

differences between the columns height. The quality of the surface seems to be better for those films what leads to the lower thickness of the cap layer formed by oxides. The thickness of the oxides is between 1.4 and 2.5 nm, what protects the film from further oxidation. It does not influence or hardly influences the optical response of the main film composed of Bi_2Te_3 with a possible interlayers of Bi.

Table 3. AFM roughness measurements on step sample after oxidation

Thickness	Roughness
8 nm	2.25 nm
6 nm	0.57 nm
4 nm	0.31 nm
2 nm	0.68 nm

The obtained thickness of the oxides' film on the BT films means that the effective thickness of the compound may be lower than that from the as-grown films by about 2 nm, what was taken into account in all presented figures.

Samples group C

In order to better understand the chemical and physical processes near the interface between the iron and Bi_2Te_3 layer we made precise measurements of the state of the sample after the exposure to the air. This process, just like in the case of samples from group B played especially important role in proper interpretation of the results received from femtosecond laser spectroscopy.

During the measurements we obtained the photo-electron spectra of $Te3d_{5/2}$ and $Bi4f_{7/2}$ core levels that were fitted by Gaussian-Lorentz or asymmetrical lines Fig.4.16. From the fitting of $Te3d_{5/2}$ core level line we can distinguish, aside of normal for this type of material oxidation states, of tellurium TeO_2 at 576.0eV and corresponding to the Bi_2Te_3 572.2eV line, additional state at 572.6eV that suggests presence of FeTe in the form of thin film. In case of

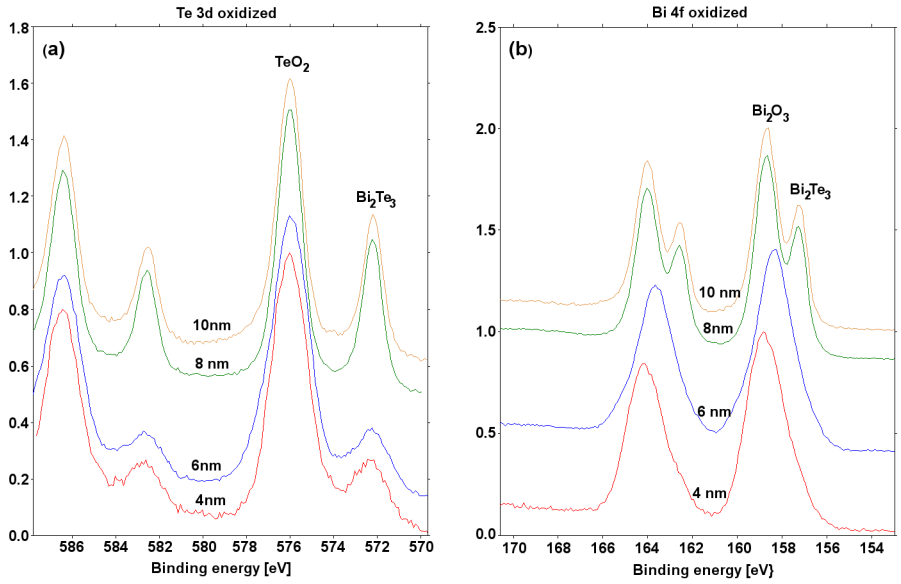

Figure 4.15: XPS doublets of $Te3d_{5/2}$ (a) and $Bi4f_{7/2}$ (b) after oxidation of the film.

bismuth, we can observe presence of only two main peaks coming from formation of Bi_2O_3 at 158.9eV and line coming from Bi_2Te_3 at 157.45eV.

Additionally, we performed a thorough investigation of the state of $Fe2p3$ core level line Fig.4.17, it was possible to successfully fit the multiplet of iron 2p3. In presented figure we can clearly see the main peak (709eV) and three others coming from the splitting. The additional peak at 713.5eV comes from the surface. Due to the fact that 1st and 2nd peak are of the same hight and, on the picture beneath, we can see the main line at 710ev and a satellite with shift of about 9eV. The iron is in a state of Fe3+ and because of the shape of the multiplet, we can say that the formed oxide with a big probability is $\gamma - Fe_2O_3$ (Maghemit) form of iron oxide [55]. Further analysis of the spectra also revealed as well existence of additional states in the valence band Fig.4.18 between the 2-8eV originating from the formation of the oxide layer, and additional states visible close to 1eV that correspond to Bi_2Te_3 compound.

After initial test of the states of the compounds directly on the surface of the sample, measured film was slowly removed with collimated beam of argon (Ar+) ions to perform depth

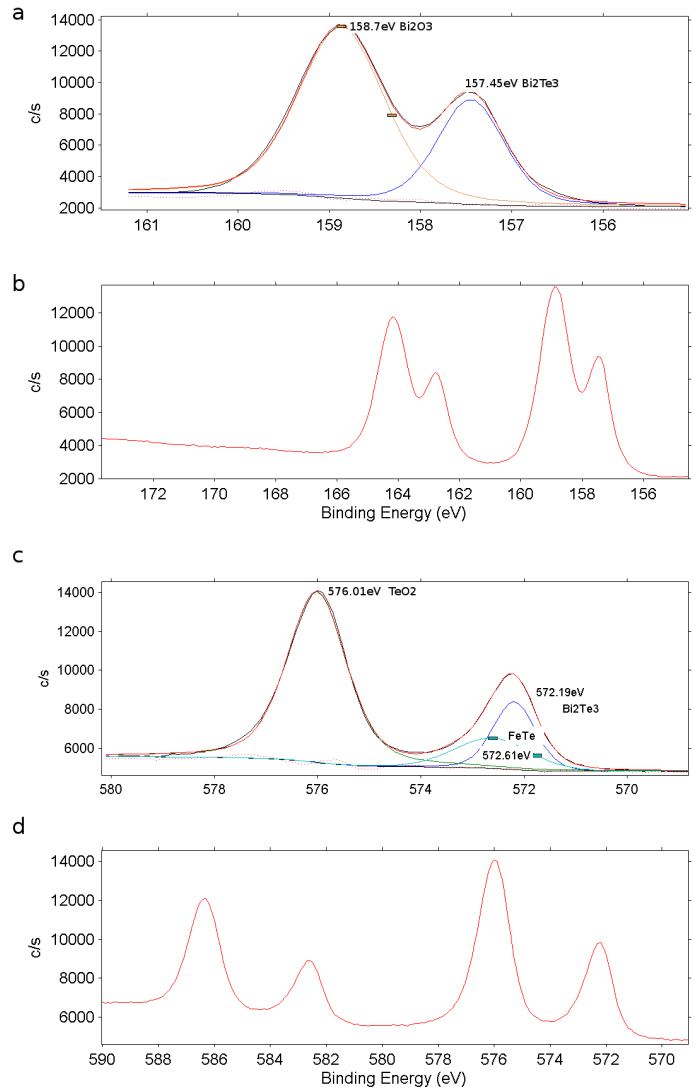

Figure 4.16: a - XPS spectra fitting of $Bi4f_{7/2}$ core level and b - view over $Bi4f_{7/2}$ doublet lines. We can see two chemical states of Bi, one belonging to the oxide and second one to Bi_2Te_3 compound. c - XPS spectra fitting of $Te3d_{5/2}$ core level and d - view over $Te3d_{5/2}$ doublet lines. We can see that the tellurium has three chemical states: two main ones belong to oxide and Bi_2Te_3, third one probably belongs to pure Te in metallic state or FeTe compound.

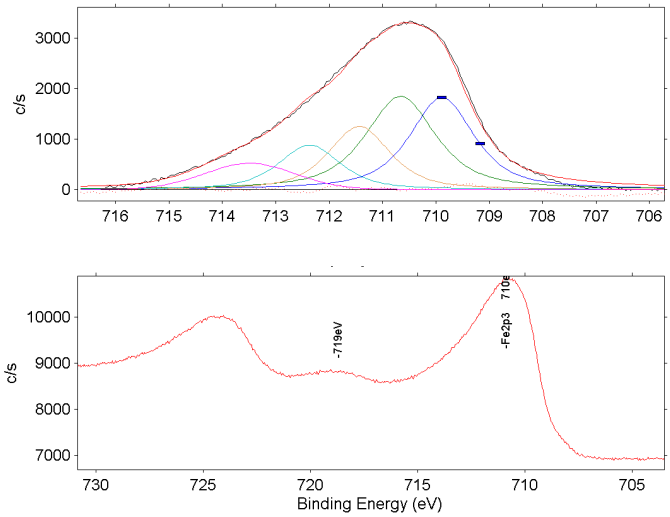

Figure 4.17: XPS spectra of $Fe2p3/2$ core level.

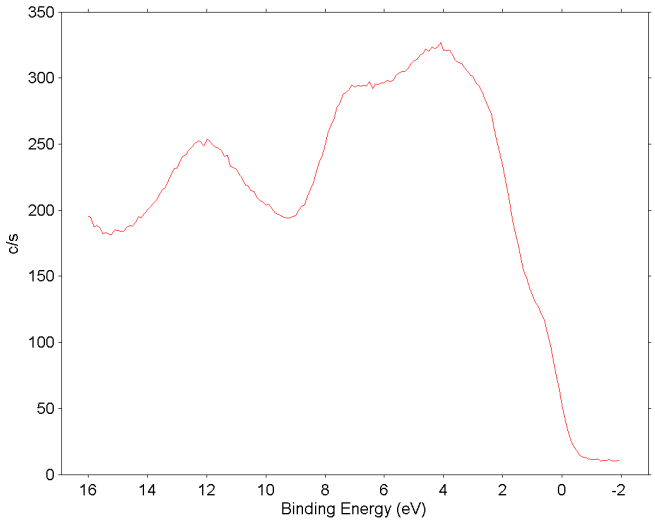

Figure 4.18: XPS spectra of valence band after the oxidation.

profiling of the sample. X-rays beam was arriving to the sample at 45° (Fig.4.19). The rate of the incoming ion beam was set to remove the layer with a speed of about 1nm per 30min with an energy of $0.7keV$, allowing us to receive a profile of the sample with a spectrum around every 2nm. It corresponds to $\sim 2QL$ change of thickness per spectrum. On presented in Fig.4.19.b depth profile we can observe change of chemical state of Tellurium. We can see that, after the removal of first 4-6nm, Te is only in a compound of Bi_2Te_3 (Fig.4.19.b yellow line). Presented in Fig.4.20.a evolution of the valence band structure shows that we are detecting the states coming from the Bi_2Te_3 already from the surface and starting from 2 line, they are dominating contribution. Analysis of the iron line Fig..4.20.b revealed traces of iron in deep parts of the sample, up to last 2-4nm of layer. Presence of iron at such depth can be explained by taking into account few factors:

• the layer growth has the dynamics of Stranski-Krastanov, where we have a formation of uniform plains upon which there is a growth of islands, such geometry allows diffusion of iron in between the islands and differences in thickness of capping layer;

• local defects in layer of Bi_2Te_3 and mica can act like channels through which iron can diffuse into the bottom layers;

• sputtering ions of argon can cause pushing in the iron deeper into the structure causing the observed effect.

We can observe as well slight shift in energy of the iron in to region of lower energy, this effect might be explained both by destruction of bonds in oxide, as well by different structure of iron deeper inside the layer. Based on previous observations [34] it is possible that iron forms the FeTe structure within the sample. Unfortunately, because of similar binding energy of Te in FeTe and Bi_2Te_3, it is impossible to use it for confirmation.

Performed depth profile on the valence band revealed that the electron structure typical for the Bi_2Te_3 is visible even through the oxide layer Fig.4.20.a. The oxidised states are a source of large contribution into the density of states between 2-8eV, and vanish rapidly after removal of fist 4nm. Starting from line (13-12nm) the valence bands are exactly the same as in pristine

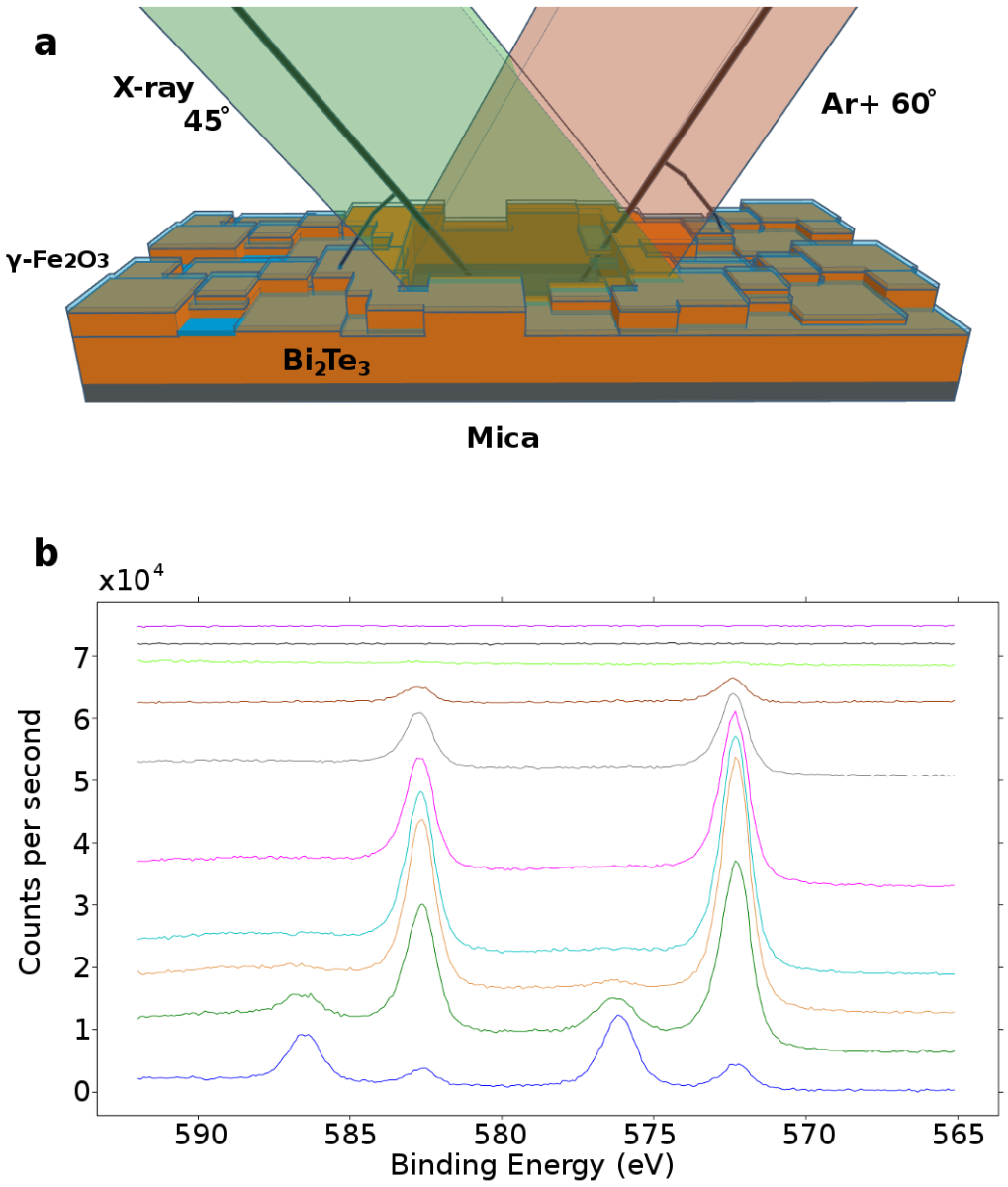

Figure 4.19: a - Artistic visualization of the surface of sample C2. Due to Stranski-Krastanov type of growth, sample at start of deposition develop well formed layers up to 10-12nm, after that the material started to form island-like structure that retained proper order and symmetry to the layers underneath. Highlighted with green plane indicates the direction of the X-ray analysis beam, where beem of ions used to remove layers was marked with red. b - Profile of sample C2 on line $Te3d_{5/2}$, the bottom blue line corresponds to the surface of the sample, following lines were made during removal of next 2nm (2 QL) from the sample.

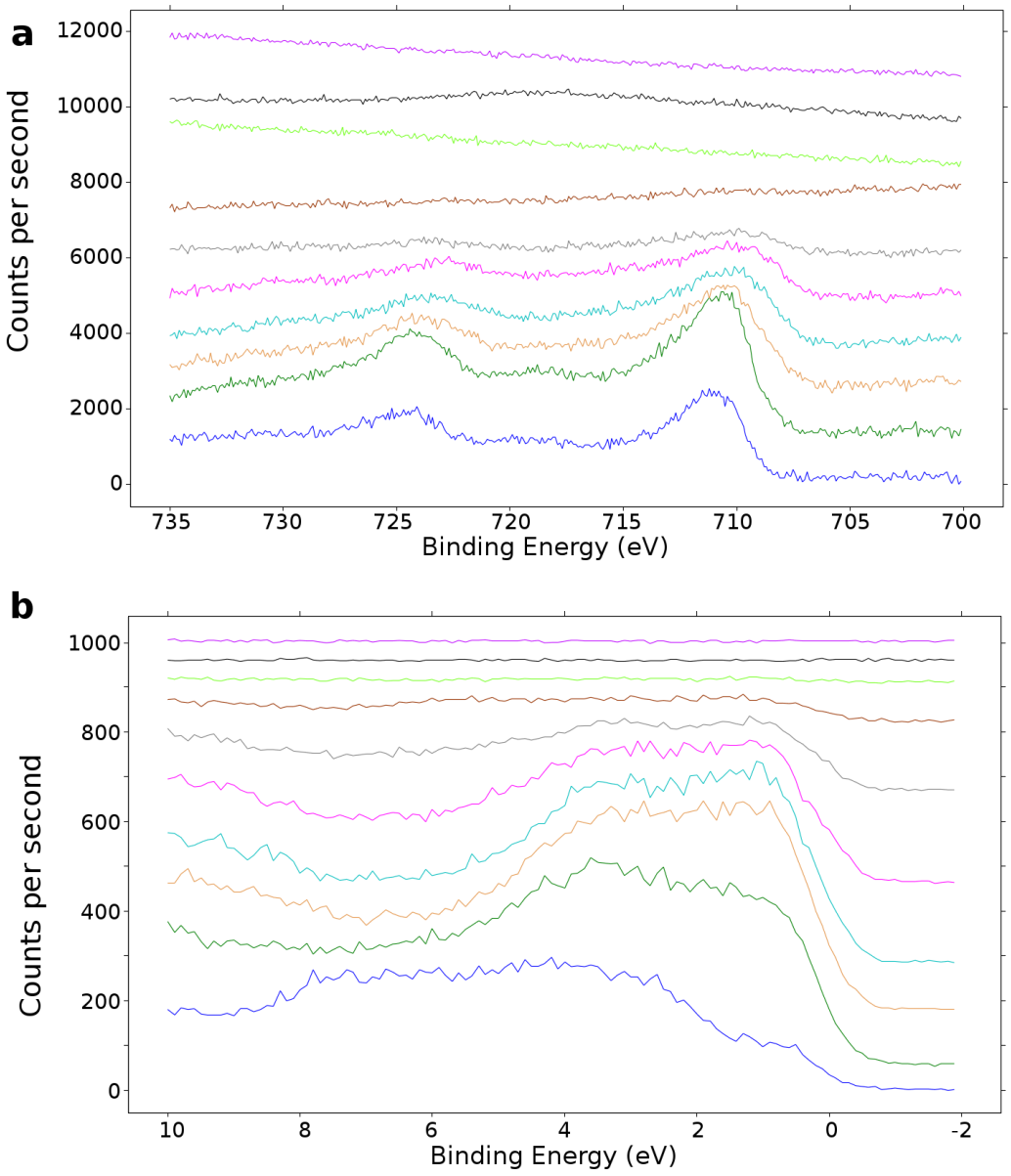

Figure 4.20: a - Profile of sample C2 on line Fe2p, the bottom red line corresponds to the surface of the sample following lines which were made during removal of next 2nm (2 QL) from the sample. b - profile of valance band, the bottom red line corresponds to the surface of the sample following lines which were made during removal of next 2nm (2 QL) from the sample.

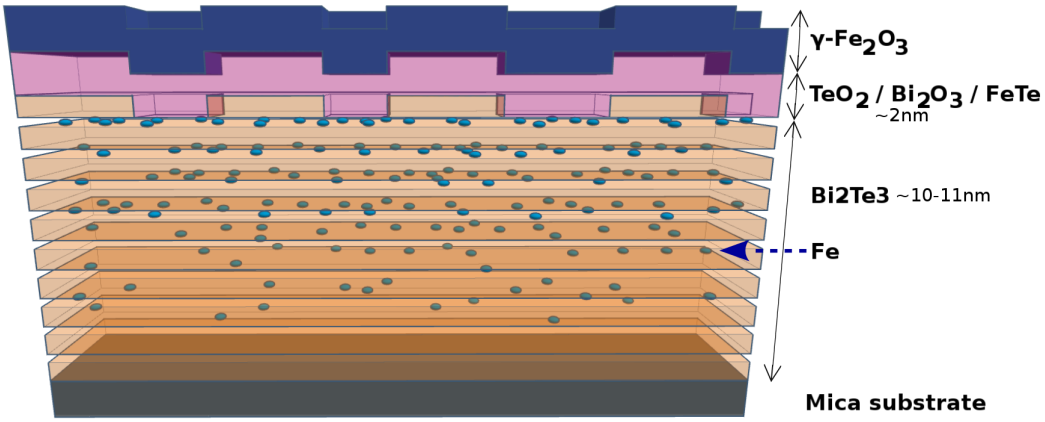

Figure 4.21: Artistic sketch of sample C2 cross-section based on data received from the depth profile.

freshly deposited Bi_2Te_3 [29, 30, 12, 34]. Taking into account the data from the depth profile, we managed to create a model of the layer with deposited iron, presented in Fig.4.21. On presented figure we marked with blue spot the detected states of iron, that should not disturb the structure of Bi_2Te_3 and tend to accumulate in the Van der Waals layers between the QL's. Because of uncertainty of the state of the iron (oxide or FeTe) it was marked as Fe.

4.3 Summary

Conducted experiments on samples from the group A revealed differences in crystal structure between sample grown on Muscovite Mica A1 and Silicon (001) A2 and A3. The diffraction image of sample A1 has shown a clear presence of very small terraces that posses two characteristic to the hexagonal cell patterns. The correct structure and stoichiometry of this film were confirmed as well by the LEED image and XPS spectra (Bi/Te - 46/54). In case of samples A2 and A3 the RHEED image revealed formation of polycrystalline structure that might be caused by mismatch between Bi_2Te_3 and silicon (001). Performed XPS also revealed as well that both A2 sample and A3 are rich in Te (A2: 35/65; A3: 33/67) such composition

is known to cause formation of the interlayers of Te in between the Van der Waals layers of Bi_2Te_3 [50].

Investigation of the samples from group B revealed that the deposition technique similar to one used in creation of the sample A1 gives stable and repeatable high quality films of Bi_2Te_3. Due to unique opportunity given by planned variation in thickness, we were able to revile that layers of Bi_2Te_3 have tendency to grow with Stransky-Krastanov dynamics. Similarly to the sample A1, films from group B shown the stoichiometry rich in bismuth, that should, in result, give a stable superstructure Bi-BT within the QL's. Performed after the oxidation XPS measurements revealed existence of passivated layer ($\sim 2nm$) of Te and Bi oxides, that is stable in time and acts as protective layer from further degradation of deposited layers.

Experiments performed on the last set of samples with deposited iron oxide allowed us to identify the state of iron ($Fe3+$) and type of the formed oxide ($\gamma - Fe_2O_3$). Additionally, depth profiling of the layer C2 has shown the presence of iron within the structure of Bi_2Te_3. The lack of change in energy of core levels both of Bi and Te, characteristic to formation of Bi_2Te_3, lead us to conclusion that the additional iron within the layer might be in oxidized form or in compound with Te but at the same time, it does not destroy properly formed QL's of Bi_2Te_3. This data allowed us to create possible model of formed structure that we presented in Fig.4.21.

Chapter 5

Time resolved spectroscopy techniques

In this chapter we will focus on ultrafast time resolved spectroscopy. We will show the current description of the mechanisms of the signal generation and the setup used to perform our experiments. We will also present the results obtained on thin films of Bi_2Te_3 that were described in previous chapters.

5.1 Introduction to pump-probe techniques

5.1.1 Experiment

All performed measurements were made on femtosecond laser setup at Le Mans University presented in Fig.5.1. Used geometry allowed us to perform standard pump-probe spectroscopy both in reflection as well as in transmission. As the laser source for the experiment we used Ti:sapphire Chameleon laser operated with (f_L) 80 MHz repetition rate and (P_L) maximal power of 3,2 W with pulse duration τ_{pulse} below 200fs. That translate to the energy of single pulse at:

$$E_{pulse} = \frac{P_L}{f_L} = \frac{3,2W}{80MHz} = 40nJ$$

Produced by the laser beam 830nm (1.495eV) is then split with a polarizing beam splitter into a pump and a probe beams. The probe beam is introduced in an synchronously pumped Chameleon OPO (principles of second harmonic generation and frequency mixing in Appendix), from Coherent company, that allows us to tune the wavelength in range of 600-550nm and finally permit to do two-color pump-probe experiments (pump and probe linearly and circularly polarized respectively) that allowed us to filter out the pump contribution on the photodetector. During our experiments we kept the probing line in range 590-570 nm (2.13 eV). For the chosen energies of pump and probe it corresponded to absorption lengths of 8 nm and 10 nm (for optical constants see Appendix) [38]. The pump line was modulated with wave function by EOM device, which was adjusted in real time by lock-in amplifier using as a reference signal from photo-diode. Pump signal was also delayed in time to the probe signal by changing its path using computer controlled delay line (Fig.5.1.b). This part of the system is crucial for femtosecond spectroscopy. Delay line causes delay of the pump arrival in accordance to probe in order to detect the evolution of the system as a function of time. Delay line usually consist of mechanised moving mirror, in our experiment it is placed on the pump optical path. This element requires a high precision of movement in order to achieve a good resolution of acquired data. To put it in perspective, a movement of the mirror by $\Delta L = 0.1mm$ results in

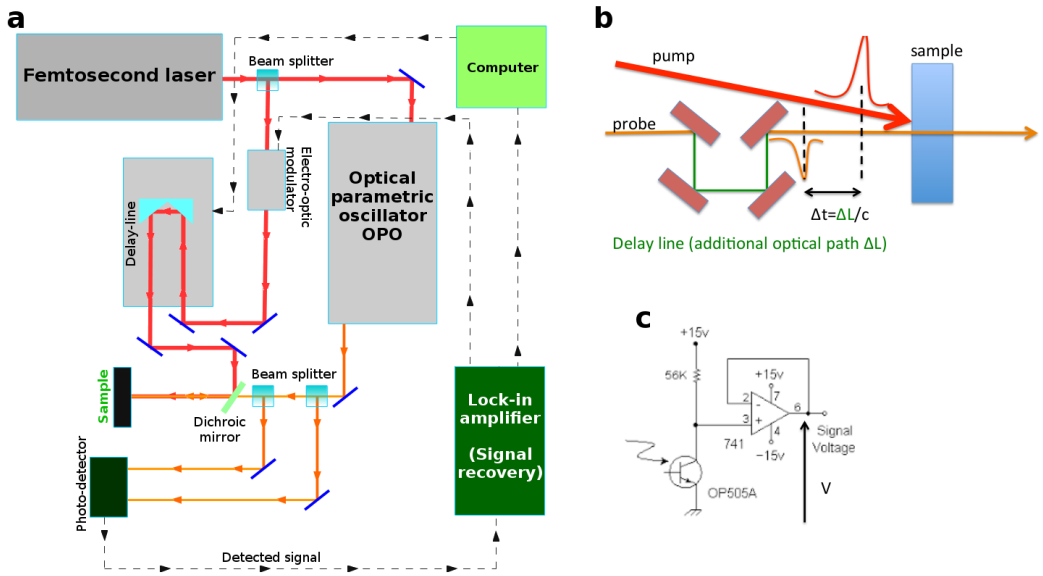

Figure 5.1: a - Schematic of two-color pump-probe experiment. b - Schematic of delay line. c - Schematic of photo detector.

time delay between pump and probe at the scale of:

$$\Delta t = \frac{2\Delta L}{c} = \frac{10^{-4}s}{3 \cdot 10^{8} m/s} \approx 300 fs$$

The pump and probe meet each other at the dichroic mirror, that reflects pump and transmits the probe. This allow us to superimpose pump and probe on the surface of the sample. In our experiment we use pump power of around 10mW ($E_{pulse} = 0.125nJ$), that gives the rate of energy that the pump deposits on the surface of the sample at:

$$P_p = \frac{E_{pulse}}{\tau_{pulse}} = \frac{0.125nJ}{200fs} = 625W$$

The energy of the probe was kept at around 1mW that is 10 times lower then the pump. Both beams were then focused with microscope objective down to a spot of A area around $80\mu m^2$. That gives the total intensity of the pump equal to:

$$I_p = \frac{P_p}{A} \sim 8 \times 10^{12} \frac{W}{m^2}$$

and the fluence of the pump (that gives us information of how much energy single pulse has deposited over the era):

$$F_{pulse} = \frac{E_{pulse}}{A} = 1,6\frac{J}{m^2} = 0,16\frac{mJ}{cm^2}$$

The reflected (or transmitted) probe is then directed to photo detector (Fig.5.1.c), that transforms the intensity of the arriving pump to voltage, that can be then introduced into lock-in amplifier.

5.1.2 Theory

Methods of registration of fast processes have went through an unusually rapid process of development, throughout last 100 years. At the end of the 19th century the shortest possible time resolution was around few ms (10^{-3}), and at the end of 20th century it was pushed by a tremendous factor of 10^{14}, which opened a new doorways for the understanding of fundamental processes in physics and chemistry. Nowadays technology allows direct observation of quantum effects with time resolution as short down attoseconds (10^{-16} s), what is one of the most spectacular achievements in terms of technology and it was awarded in 2018 an Nobel Prise in Physics. This time resolution was achieved in 2006 as the shortest time-scale ever was observed (direct measurement of light waves - Fig.5.2). Unfortunately systems that are able to achieve such time resolution are still presenting a challenge. On the other hand the femtosecond (10^{-15} s) time resolution is relatively easy to achieve with commercially available sources.

Ultrafast processes are governed by different rules than conventional macroscopic physics. For example, during first few femtoseconds after the excitation electrons move while cations may still be frozen. In such time scales classical statistical temperature cannot be defined and such systems are deterministic mainly because the observation time is too short for the system to explore the entire phase space. New concepts have to be thought up in order to understand

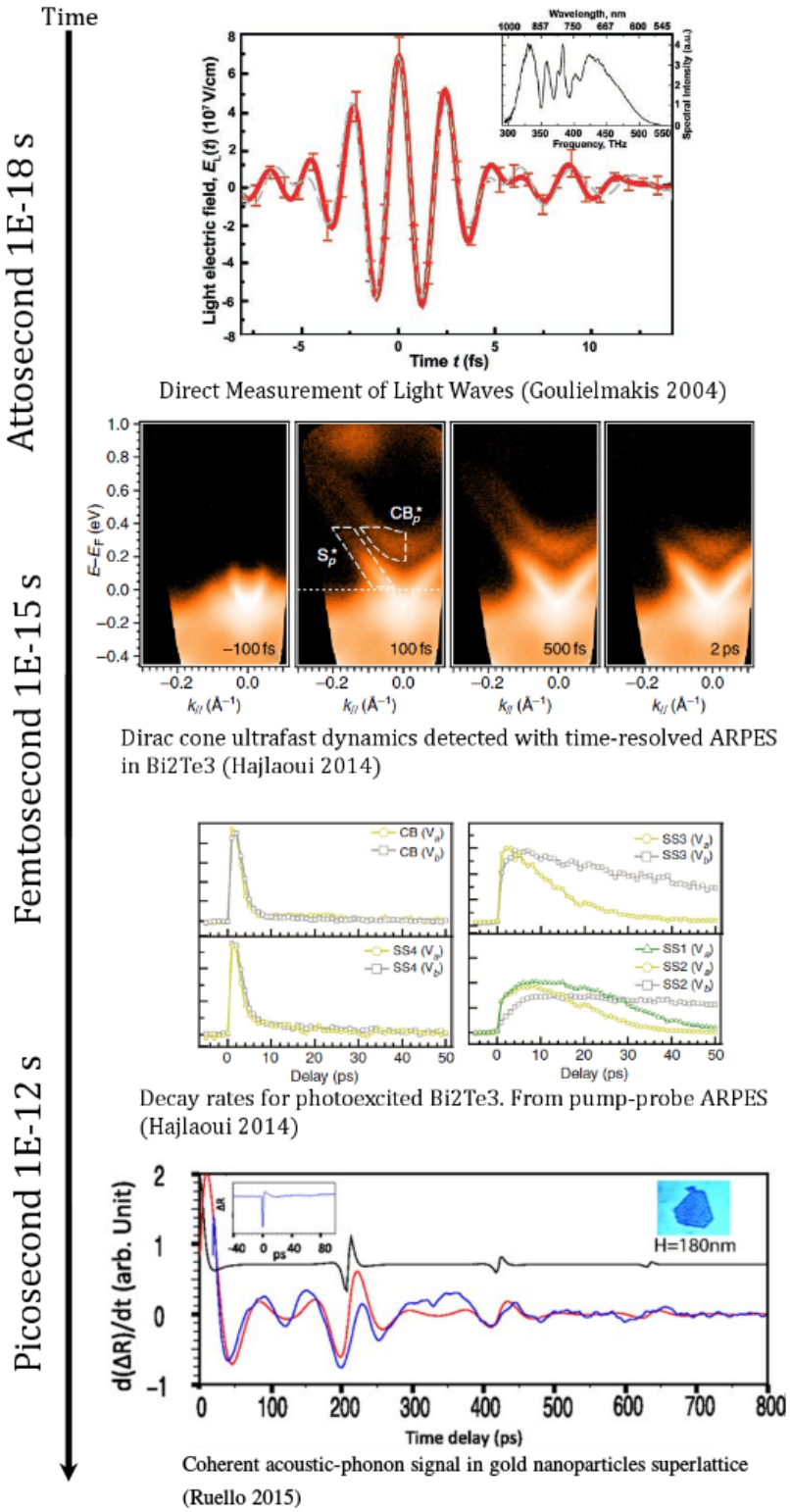

Figure 5.2: Time scale of our ability to register physical processes.

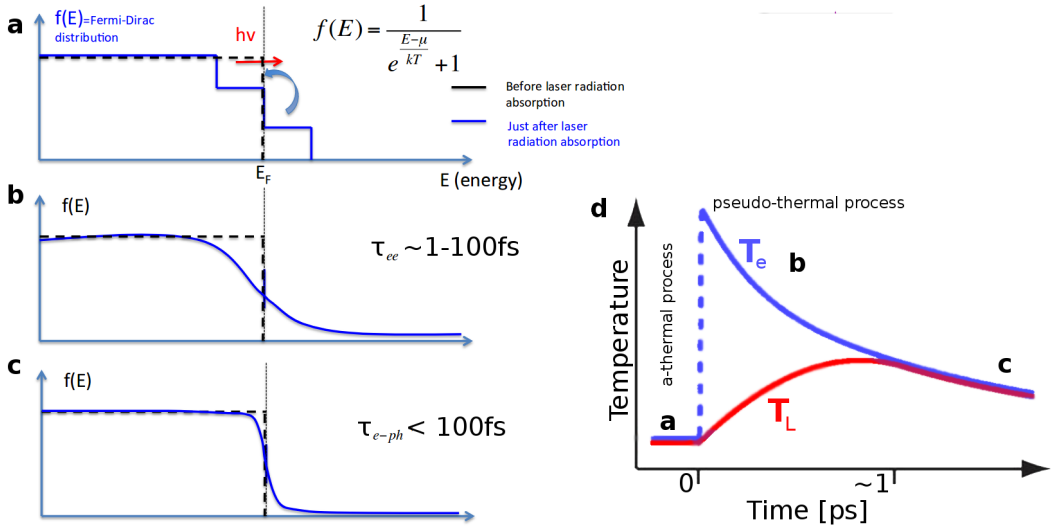

Figure 5.3: Time dependence of the Fermi distribution after an ultrafast laser exciton: a - photon energy is first absorbed by the electrons, b - thermalization of electronic subsystem, c - thermization of the electronic subsystem with the phonon (cations) subsystem. d - TTM two temperature model shows the time scale of afore mentioned processes.

and interpret the femtosecond time scale. Ultrafast laser excitation may lead to non trivial effects, such as the relaxation channels used by the system to dissipate energy being dependent of the duration of the external trigger. The time resolved pump-probe experiment is based on the simple idea of time-lapse motion detection like in normal cameras.

Carrier dynamics:

When the photon packet arrives to the sample it interacts with part of its volume, leading to modification of internal energy. The photon energy is first absorbed by the electrons, in the case of interaction with light in visible spectrum range (Fig.5.3), in general after which electrons start to thermalize rapidly τ_{ee} by electron-electron collisions (Fig.5.3.b) [56]:

$$\tau_{ee} = \tau_0 \left(\frac{E_F}{kT}\right)^2 = \tau_0 \left(\frac{E_F}{\Delta E}\right) \tag{5.1}$$

usually within $1-100fs$, after which the system start to dissipate energy through electron-phonon interaction (Fig.5.3.c) [57]:

$$\tau_{e-ph}(E) = \frac{C_e}{2g}\left(1+\sqrt{1+\frac{E}{E_0}}\right) \tag{5.2}$$

As a first approximation those time can be derived by taking into account the specific heat of electron C_e and lattice C_L in two temperature model (TTM) initially proposed by Kaganov, Tanatarov and Lifshitz [58] (Fig.5.3.d). After excitation with an ultrashort optical pulse electrons and after the electron-electron thermalization, the electrons are described by a Fermi-Dirac distribution at temperature T_e (see Fig.5.3.b) and the lattice by a Bose-Einstein distribution at temperature T_L, the general equations for this model are as follow [59]:

$$\begin{cases} C_e(T_e)\dfrac{\partial T_e}{\partial t} = \kappa\Delta^2 T_e - g(T_e-T_L) + P_0(r,t) \\ C_L\dfrac{\partial T_L}{\partial t} = g(T_e-T_L) \end{cases} \tag{5.3}$$

where g is the coupling constant between electronic and phononic subsystem (deformation potential, Fröhlich, etc...), κ is the electron thermal conductivity, and $P_0(r,t)$ is optical source term that provides the energy to the electronic subsystem (Gaussian function). The energy transfer from the electrons towards the phonon subsystem is proportional to the difference of their corresponding effective temperatures. This model works quite well with metals where the relaxation of electrons occurs through the intraband relaxation mechanism [59], but in case of semiconductors we have to take into account not only the intraband process but also interband process, due to existence of band gap Fig.5.4.b. The two temperature model can be separately applied be defined for electrons and holes in intraband relaxation process, that takes place in the conduction (CB) and valence (VB) bands respectively. This allows the determination of the energy exchange between electrons and holes with lattice during that intraband process. This works as far as the interband relation ($CB \rightarrow VB$) does not take place and usually the intraband process is much faster that the interband relaxation which aloows to separate in time the description of each of these processes.. For this purpose, we need to define in the TTM a corresponding heat capacity for both electron and holes. After the intraband process is

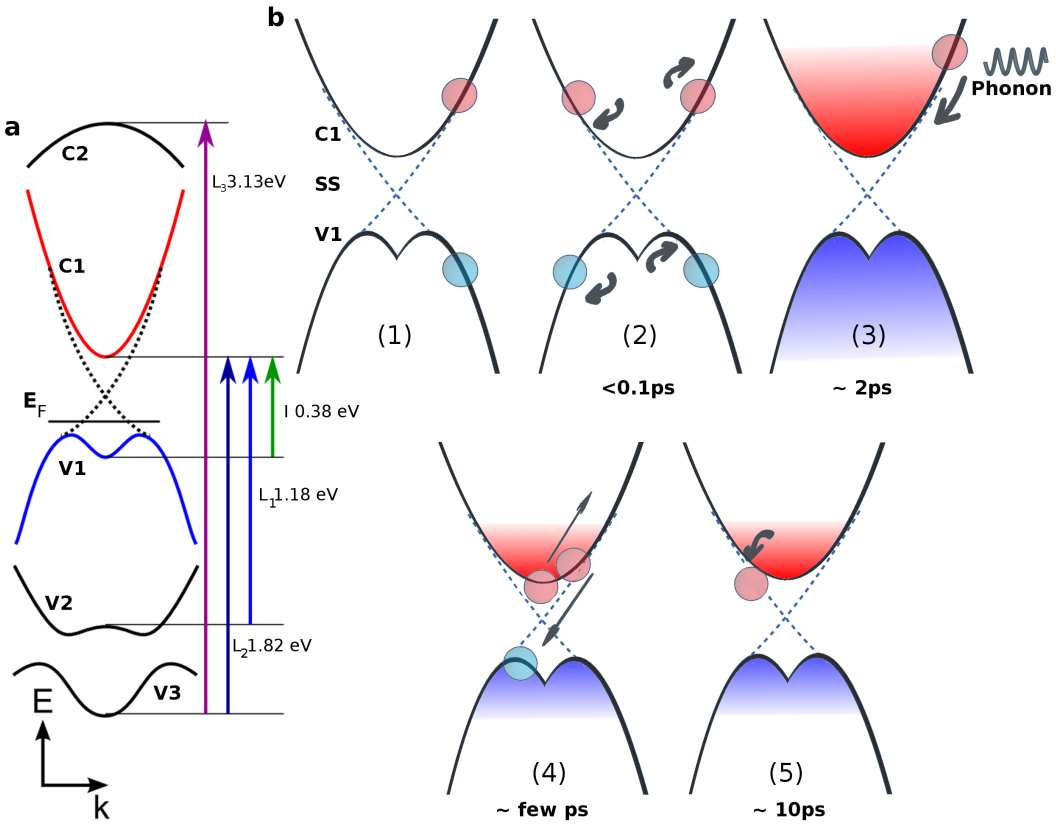

Figure 5.4: Schematic diagrams of electronic dispersions in $Bi_{1.5}Sb_{0.5}Te_{1.7}Se_{1.3}$. b - diagrams of relaxation processes of photo-excited carriers in the lowest conduction band (C1), the highest valence band (V1), and the surface states (SS) exisitng in 3D topological insulators: (1) photo-excitation of electron-hole pairs, (2) carrier thermalization, (3) carrier cooling due to phonon emission, (4) Auger recombination, and (5) intraband scattering from C1 and V1 to SS. From Y. Onishi et. al. Phys Rev B (2015).

achieved, we can say that carriers and phonon are thermalized ($T_e = T_L = T$)[59, 60]. At this stage, we can consider the electrons and holes are pretty well localised in energy at the bottom and top of the CB and VB (Fig.5.4.b). We describe then the dynamics of electrons (holes) with their volumic concentration. The electrons (holes) can then relax (interband process) either by non-radiative or radiative recombination process. For the first case, the energy that has been released to the lattice increases its temperature. For the second one, the energy is converted into a radiation. The carrier dynamic can then be described according to the Boltzman equation[59]. The carrier dynamics equation will take following form:

$$\frac{\partial N(t,x)}{\partial t} = D_{eh}\frac{\partial^2 N(t,x)}{\partial x^2} - \frac{N(t,x)}{\tau_R} + \frac{1-R}{h\nu_L} I_L f(t) e^{-\alpha x} \tag{5.4}$$

where D_{eh} is the carrier diffusion coefficient, R is the optical reflectivity of the material, τ_R is the rate of carriers recombination, $h\nu_l$ is the laser quantum energy, I_L is the laser intensity, $f(t)$ is the temporal envelop of the laser pulse (Gaussian) and α is the optical absorption. This out-of-equilibrium electron-hole distribution will immediately affects the optical properties of the material. The dielectric function will be perturbed which leads to the following variation of the optical reflectivity coefficient with:

$$\frac{\Delta R}{R} = f(\varepsilon_1, \varepsilon_2) = \frac{\partial lnR}{\partial \varepsilon_1}\Delta\varepsilon_1 + \frac{\partial lnR}{\partial \varepsilon_2}\Delta\varepsilon_2 \tag{5.5}$$

where the ε_1 and ε_2 are the real and imaginary part of the dielectric constant, which are dependant on number of photo-excited carriers. During the excitation with the pump light pulse we transfer electron from the VB into the CB (Fig.5.4.a) in result we change the electron density function leading to modification of light absorption and transmission through the change of $\Delta\varepsilon_1$ and $\Delta\varepsilon_2$. This effect is then used in pump-probe experiment in following way: after the pump excitation the irradiated region is probed with a second laser pulse (so-called probe) which fluence is smaller than the pump. Because the fluence of the probe is much lower than the pump, the induced change in dielectric function by the probe is small enough to be in the linear regime of the detection process. Probe that is being transmitted or reflected from the sample carriers now information about the change generated in dielectric function ($\Delta\varepsilon_1$ and

$\Delta\varepsilon_2$) initiated by the pump pulse

During the first femtoseconds we can typically observe (Fig.5.5) a sharp change in optical properties, that is typically refereed as electronic peak. In case of absorbing solid, as it is in case of Bi_2Te_3, this phenomenon is attributed directly to excitation of hot carriers, which relaxation process play an important role in launching the coherent vibrations, that will be discussed later on. As earlier proposed in the literature [61], the transient electronic contribution to the change in signal $\Delta R/R_{elec.}$ of the optical reflectivity can be numerically adjusted with a function that takes into account the integrated response of the solid during the pump-probe cross correlation as well as the decaying signal. For the latter one, we need two use two characteristic times, τ_1 for the fast dynamic (ps) and τ_2 for the slower one (thermal effect or slow electronic relaxation).

$$\frac{\Delta R(t)}{R}_{elec.} = \left[1 + erf\left(\frac{t}{\sigma} - \frac{\sigma[\tau_1+\tau_2]}{\tau_1\tau_2}\right)\right]\left[A_1 exp\left(-\frac{t}{\tau_1}\right) + A_2 exp\left(-\frac{t}{\tau_2}\right)\right] \tag{5.6}$$

with σ the resolution of measurement that is dependant on the optical path and the laser pulse duration, τ_1 the hot carrier relaxation, τ_2 the thermal relaxation, A_1 the hot carriers contribution and A_2 the thermal contribution. Once the electronic contribution is adjusted, it is possible to extract the phonon contribution $\Delta R/R)_{phonon}$ arising from the optical and acoustic phonons (green curve in Fig.5.5).

Phonon generation and detection:

The relaxation of hot carriers leads to generation of stress at the unit cell level (generation of optical phonon) or macroscopic scale (acoustic phonon) within the structure. This photo-induced stress is the driving mechanism of coherent vibrations. For the case of coherent acoustic phonons, the lattice motion can usually be described with general equation of motion in accordance to classical Newton law [59, 60]:

$$\frac{\partial^2 u(x,t)}{\partial t^2} - \nu^2 \frac{\partial^2 u(x,t)}{\partial x^2} = \frac{1}{\rho}\frac{\partial \sigma(x,t)}{\partial x} \tag{5.7}$$

where $u(x,t)$ is a function describing the atom motion, ν is a speed of propagation of the acoustic pulse, ρ is the density of the medium and $\sigma(x,t)$ is time and space function of photo-

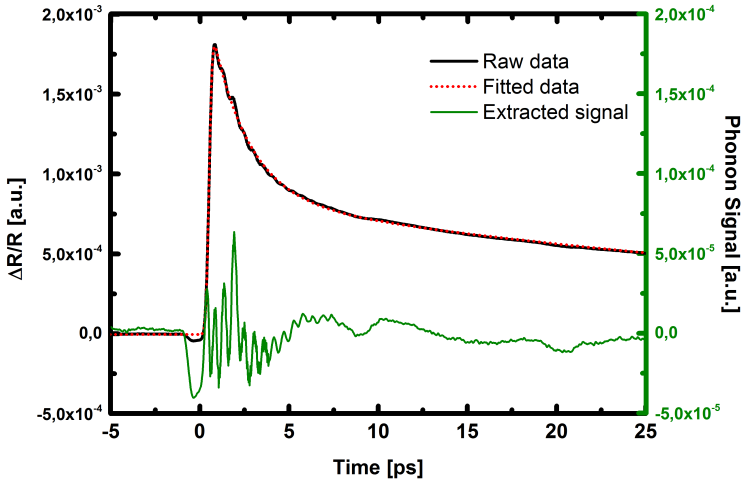

Figure 5.5: Measured signal was fitted with function 5.6 and remaining after subtraction residua are consisting mainly of the phonon signal from investigated region.

induced stress. This photo-induced stress spatial distribution is governed by the optical skin depth at the pump light wavelength, but can also be affected by hot carriers diffusion for example [59, 60, 63]. In this approximation, we are only discussing one dimensional geometry. It is possible to take such assumption when the irradiated area is much larger than the distance of propagation of the coherent acoustic pulse. The photo-induced stress has few dominating processes at its origin, that is deformation potential and theromoelasticity [59, 60, 63].

Deformation potential mechanism generates the stress within the material by modification of the electron energy distribution. This change in electronic distribution, in this case due to optical excitation, leads to the change in interactions between electrons-cations, cations-cations and electrons-electrons. In result, it generates evolution of the interatomic forces, since they are dependent on this distribution (Fig.5.6). A change in the interatomic forces leads to the change of position of cations from their equilibrium in lattice and hence to the crystal deformation [59, 60, 63]. We can say that the out-of equilibrium carriers induce the deformation of the crystal lattice and consequently coherent vibrations are emitted. The relation between

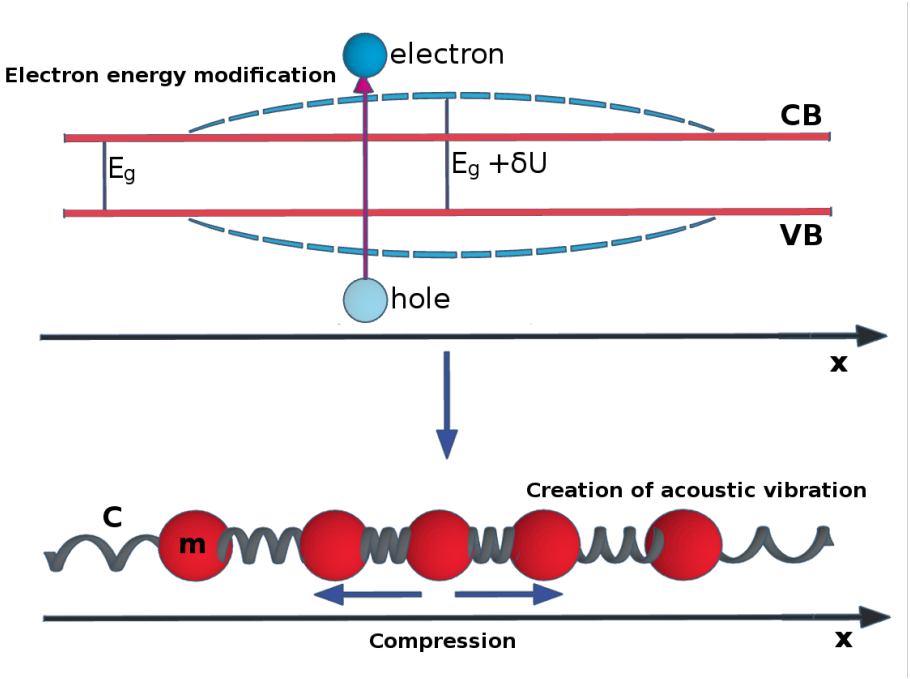

Figure 5.6: Deformation potential in band structure picture: excitation of an electron hole pair disturbs the electronic distribution and modifies the interatomic interaction leading to a change of atomic positions and consequently to the generation of a strain field.

the local strain in the lattice $(\frac{\delta V}{V})$ and the change of the electronic energy (δU) is given by equation [60]:

$$\frac{\delta V}{V} = \frac{\delta U}{d_{eh}} \tag{5.8}$$

where d_{eh} is deformation potential parameter. We can clearly see that the change in electron energy levels is directly connected to generation of strain in the structure. It is possible to understand the deformation potential through the molecular picture, as shown in Fig.5.7. When the light pulse induces the carrier excitation the electron (or holes) takes unoccupied electronic levels, in result it leads to creation or destruction of atomic bonds. Depending on the type of the bond (bonding or anti-bonding) this process leads to compression or expansion of the bond between the atoms [60]. The photo-induced stress can be correctly described by taking

into account the existence of electronic band structure in the solid. During the photo-induced carrier excitation we are modifying the electron population at different levels E_k, we can then show that the measured photo-induced stress[63]:

$$\sigma_{DP} = -\sum_k \delta n_e(k) E_k \gamma_k = \sum_k \delta n_e(k) \frac{\partial E_k}{\partial \eta} \tag{5.9}$$

where k is the wave number of electron, $\delta n_e(k)$ denotes the change in concentration at level k, γ_k is the electronic *Grüneisen* coefficient and $\frac{\partial E_k}{\partial \eta}$ is the induced change in electronic levels because of the induced stress (i.e the deformation potential parameter).

Due to ultrafast relaxation of the photo-excited carriers in metals, the deformation potential is able to launch the coherent acoustic vibrations only during first picoseconds before the relaxation of the carriers at the Fermi level. This means that the coherent acoustic pulse has a typical duration of 1ps (the order of the electron-phonon thermalization time). As a consequence, such THz pulse is not easy to be detected [59, 60]. After the thermalization process is finished, the lattice has been heated up and the thermoelastic process becomes the driving mechanism (discussed a bit later on). The role of the deformation potential can be especially important in system in which electrons cannot easily escape and are confined within the excited region (like in the case of nanoparticles, see [62]), in such case the electron pressure can remain the largest contribution to the induced stress. In case of semiconductors with channels for fast intraband relaxation (hot electrons are relaxing towards the bottom of the conduction band), we can simplify the deformation potential:

$$\sigma_{DP} = \sum_k \delta n_e(k) \frac{\partial E_k}{\partial \eta} = N \frac{\partial E_k}{\partial \eta} = N \frac{\partial E_g}{\partial \eta} = -NB \frac{\partial E_g}{\partial P} = -d_{e-op} N \tag{5.10}$$

Where B is the bulk modulus of the crystal, N is the concentration of photo-excited carreirs, E_g is the band gap, and d_{e-op} is deformation potential parameter at the band gap energy. This model works only for frequencies that are smaller than inverse of the intraband relaxation process time. Deformation potential, depending on the nature of electronic levels to which the carriers where excited, can take either compressive or tensile nature [59, 60, 63]. The type of

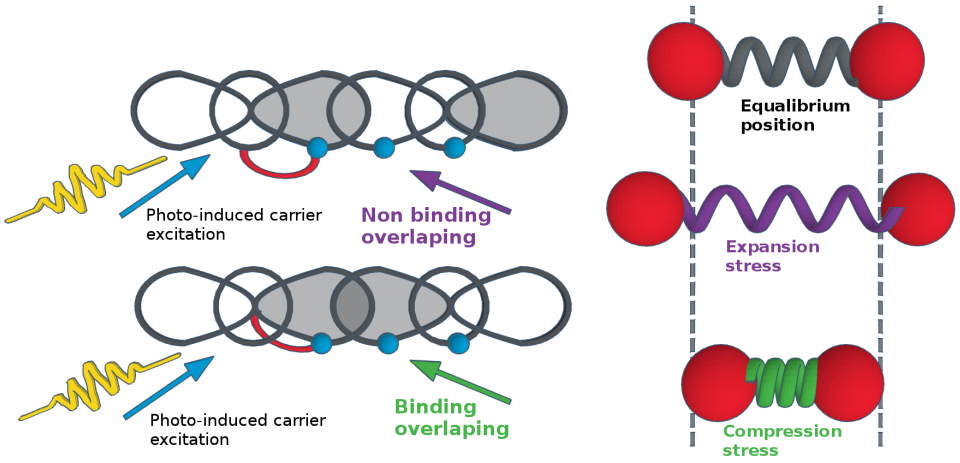

Figure 5.7: Deformation potential in molecular picture: excitation of electron from one orbital to another modifies the electronic distribution causing appearance of bonding (compression) or antibonding (expansion) interactions between atoms.

the change is determined by the sign of the deformation potential parameter, and can be directly obtained from the pressure dependence of the band gap. In case of an increase with the pressure $\frac{\partial E_g}{\partial P} > 0$ the d_{e-op} is positive, and the structure expands under the electron excitation. The opposite reaction leads to the structure contraction. This situation is a direct result of the nature of molecular bonds (binding, non-binding or anti-binding) Fig.5.7.

The most known mechanism of generation of coherent acoustic phonons is the thermoelasticity. The basis of this phenomenon is the conversion of deposited laser pulse energy into lattice energy (thermal energy) by different channels of relaxation. The quick rise in thermal energy leads to an expansion of the irradiated volume through the lattice anharmonicity. This expansion, in case of ultra short laser pulses used in our experiment, generates ultrafast expansion in a time corresponding to the electron-phonon relaxation time. If we neglect the process of electron diffusion within the structure, it is possible to analytically describe the generated stress. The function of the photo-induced stress will be dependant on the temperature rise at depth of pump penetration ξ and on the total pulse energy Q that is deposited over the area A

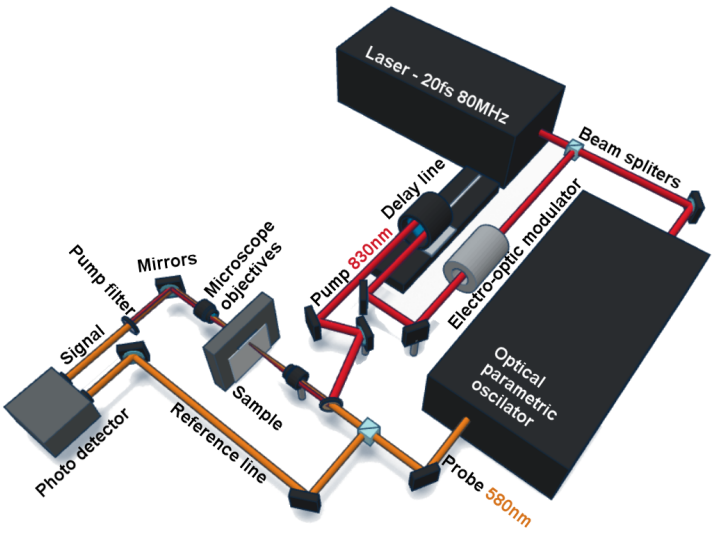

Figure 5.8: Scheme of two color pump (830nm) and probe (580nm) setup, used for the experiments.

of the structure. Induced change in temperature will take the following form [63]:

$$\Delta T = \frac{(1-R)Q}{CA\zeta} e^{-\frac{x}{\xi}} \tag{5.11}$$

where R is the optical reflectivity of the material, C is the specific heat per unit volume, x - is the distance form the surface and ξ is the typical absorption length of the pump wavelength (in case of Bi_2Te_3 for pulse 830nm it is $\xi \sim 10nm$ [38], see Appendix 7.2). Having the expression for the temperature profile we can now write down the time dependent photo-induced stress profile $\sigma(x,t)$ equal to:

$$\sigma(x,t) = -3B\beta\Delta T(x,t) \tag{5.12}$$

where B is the bulk modulus and β is linear thermal expansion coefficient.

Regarding the generation of optical phonon [64, 65, 66] we can distinguish two main models used to describe this effect. Taking into account that light can couple directly with optical phonon branches, the natural first process that was discussed is the stimulated Raman process [64, 65]. The Raman active mode whose normal coordinate is given by Q is described

following:

$$\frac{d^2Q}{dt^2} + \Omega^2 Q = \left(\frac{\partial \chi}{\partial Q}\right) |E_0(r,t)|^2 = \sum_{uv} \frac{\frac{\partial \chi_{uv}}{\partial Q} E_u E_v}{2} \tag{5.13}$$

where E_u denotes a component of the optical pump field, $\frac{\partial \chi_{uv}}{\partial Q}$ is nonlinear Raman tensor and χ_{uv} in linear electronic susceptibility. The second process is the displacive excitation of coherent phonons (DECP, deformation potential)[66], it can describe the generation of optical phonons which conserves the crystal symmetry denoted as A_1 modes. In this model we assume that, by a high intensity short laser pulse, we are able to disturb the electronic distribution in the material. In this particular case, we can say that this process is similar to the approach based on the deformation potential coupling discussed previously for coherent acoustic phonon. By this excitation the nuclear coordinates within a unit cell will change along A_1 symmetry. In this model the photo-generated interband transitions excite the population of carriers N, that are linearly dependant on the equilibrium A_1 coordinate Q_0 [66]:

$$Q_0 = \kappa N \tag{5.14}$$

and it gives us the equation of optical mode motion:

$$\frac{\partial^2 Q}{\partial t^2} = -\omega^2 [Q - Q_0] - 2\gamma \frac{\partial Q}{\partial t} \tag{5.15}$$

where ω_0 is the angular frequency of A_1 optical mode, γ is the damping constant.

In the previous paragraphs, we have briefly introduced the generation mechanisms of coherent acoustic and optical phonons. These phonons can be detected in a pump-probe experiment since they both modulate the interatomic distances (at the level of a unit cell for optical phonon or at a more macroscopic level for acoustic phonon), which consequently modulates the dielectric constant ($\Delta\varepsilon_1$, $\Delta\varepsilon_2$, see Equation 5.6). Depending on detection scheme, reflected or transmitted probe light is collected by a photo-diode which signal provides, only indirectly, some information about the photo-induced dynamics. We say indirect in a sense that we do not have access directly to the photo-induced strain but only through the modification of the

optical properties. For the detection of coherent acoustic phonons, we have to take into account the interferometric contribution due to the free surface motion $u(0)$ and the photo-elastic coupling leading to probe light scattering. For example, in the case of a semi-infinite system it has been shown that the change of the complex transient optical reflectivity generated by acoustic vibration $\left(\frac{\Delta r}{r}\right)_{ac}$ is given by:

$$\left(\frac{\Delta r}{r}\right)_{ac} = -2ik_0u(0) + \frac{4ik_0n}{1-n^2}\frac{\partial n}{\partial \eta}\int_0^{\infty}\eta(x,t)e^{2ink_0x}dx \tag{5.16}$$

where k_0 is the probe light wave vector in vacuum, $u(0)$ - is the free surface displacement in the sample, η - the strain, n - complex refractive index and $\frac{\partial n}{\partial \eta}$ - is the photo-elastic coefficient. For acoustic phonon the $\frac{\Delta r}{r}$ can be sinusoidal (Brillouin, transparent materials) or have the form of a pulse (opaque materials)[59, 60]. For optical phonon, due to the fact that the group velocity is nearly zero (no propagation), the transient optical properties takes into account only the time dependence, even of course if the total detected signal integrate the response over a volume defined by the skin depth at the given probe wavelength. For optical phonon detection process of $\left(\frac{\Delta r}{r}\right)_{op}$ is proportional to:

$$\left(\frac{\Delta r}{r}\right)_{op} = A\frac{\partial \chi}{\partial Q}a_0 sin(\omega_0 t + \varphi) \tag{5.17}$$

where $\frac{\partial \chi}{\partial Q}$ is a Raman tensor (that can be a complex term [64]), χ - is the electronic susceptibility. A and a_0 are terms that can be complex and involve the generation and detection process of the stimulated Raman mechanism [64, 65].

The fractional change in reflectivity, due to the pump pulse, were R denotes the reflectivity before the excitation is given by following relation (derivation in appendix)[63]:

$$\frac{\Delta R}{R} = 2Real\left(\frac{\Delta r}{r}\right) \tag{5.18}$$

For all our analysis we assume that the change of the reflectivity can be related to the change in voltage generated on the photo-diode:

$$\frac{\Delta U}{U} \approx \frac{\Delta R}{R} \tag{5.19}$$

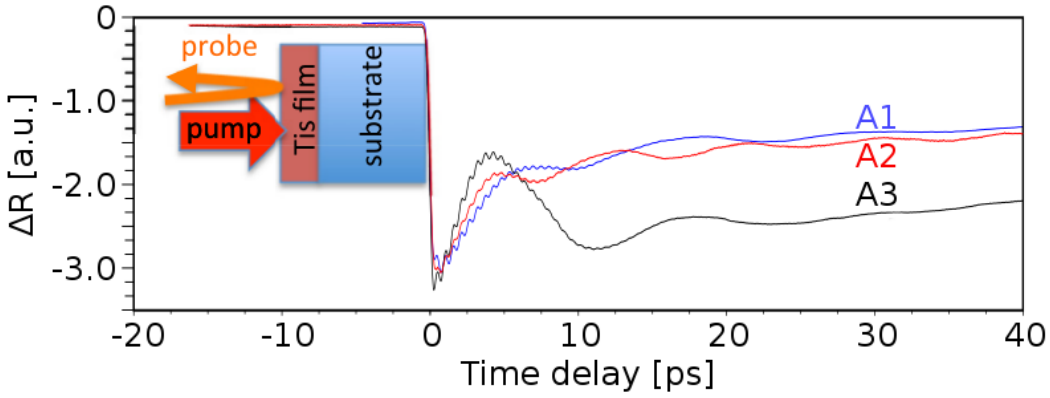

Figure 5.9: Time-resolved optical reflectivity obtained for samples A_1,A_2,A_3, data was normalized to largest magnitude for clarity.

5.2 Femtosecond laser spectroscopy - results

5.2.1 Role of structural order on electron and phonon dynamics

Samples described in this section are a perfect example of how different structures influence the obtained time-resolved optical response [29]. The time-resolved optical reflectivities obtained for the three samples are shown in Fig.5.9. The signals are composed of different contributions. The first sharp variation of the optical reflectivity R corresponds to the electronic excitation by the pump light, with subsequent decay of the out-of equilibrium carriers. Within the first picoseconds, several oscillatory components appear. The high-frequency component, as shown in Fig.5.10.a, is the signal of the coherent LO phonon A^1_{1g}, well identified by its characteristic frequency [68, 69, 70, 41]. The fast Fourier transform (FFT) of this high-frequency mode is shown in Fig.5.10.b, the signals in Fig.5.10 also show a rapid birth of low-frequency component before the A^1_{1g} mode fully decayed.

Although in our setup (Fig.5.8) we used circular probe polarization, which integrates all the contributions from the transient dielectric tensor [65], we were not able to detect the lower frequency transverse mode E^1_{g1} or the LO mode A^2_{1g} (Table.2.2). E^1_{g1} was also not detected in

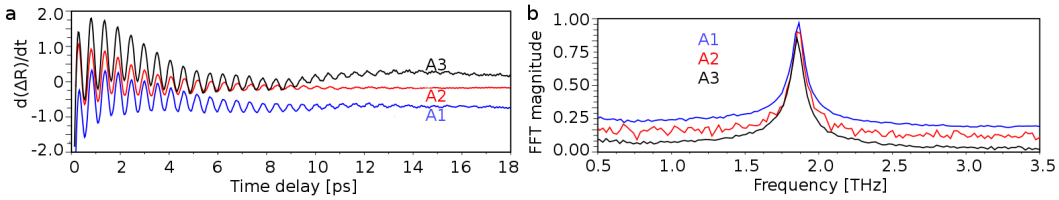

Figure 5.10: a - optical phonon signal obtained through time derivation of obtained signal, we can see strong signal from A^1_{1g} mode. b - Fast Fourier transformation of derived signal.

other studies on bulk BT [41, 68, 69, 70]. By comparing the A^1_{1g} frequency (Fig.5.10.b), we could not detect large difference between samples A1,A2 and A3. The phases in case of these these three samples is very similar as shown in Fig.5.10.a, and we did not detect any significant difference in the decay time of both hot carriers as well as the detected phonon dynamics. This is an indication that the relaxation of the A^1_{1g} mode is not dependant on long-range crystallographic order, what is in agreement with the observation of a constant Raman linewidth ($175cm^{-1}$) conducted on cleaved films that showed variable nanostructures such as change in number of QL [71]. We know that in case of Bi_2Te_3 this anharmonic coupling (phonon-phonon collision) is the main cause of low thermal conductivity of this material [72, 73]. The detected frequency of A^1_{1g}, (Fig.5.10.b) shows the same frequency as in bulk crystal and simulations (table 2.2), it is direct proof that the detected coherent optical phonon A^1_{1g} originates from the Bi_2Te_3 structure with the right chemical environment, what is in direct agreement with performed by us x-ray photo-electron spectroscopy analysis. Consequently, the slight excess of Bi in film A1 and the excess of Te in films A2 and A3 might be isolated in the structure, probably within an interlayer between QLs for Bi and Te as suggested in previous chapter [50].

We have to remember that despite the random distribution of Bi_2Te_3 grains in film A2 and A3 or the existence of crystallized terraces in film A1, the generation and the detection of A^1_{1g} mode is very efficient. Thus it let us to believe that the main mechanism behind this process is due to the large and localized coupling between hot electrons and the A^1_{1g} mode. The mechanism of ultrafast generation of symmetry A^1_{1g} modes has already been discussed in

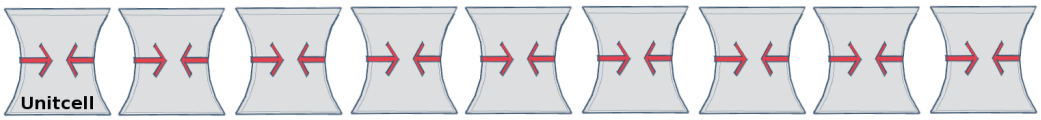

Figure 5.11: Optical phonon vibrations are confined to the unit cell and do not create force that would act on whole layer.

the literature [66] and is usually attributed to a hot electron-phonon coupling that preserves the lattice symmetry. But the discussion of the quantitative generation process needs knowledge of the electron-phonon coupling parameter, which is usually lacking. In case of Bi_2Te_3, recent calculations have shown that the isotropic electron/optical phonon deformation potential is in fact as large as $d_{e-op} \approx 40eV$ [73]. We have reported (Fig.5.10.b) that for our nanostructures the A^1_{1g} mode has the same frequency as bulk BT. This indicates that the interatomic potentials are similar in bulk BT and in our nanostructures (for the case of enough thick layer, i.e. bulk-like layer), so that it is reasonable to use a bulk electron/optical deformation parameter, as a first approximation, to discuss the photo-induced forces. Then, following the conventions used in semiconductor physics [67], the associated photo-induced stress driven by the deformation potential can be written as:

$$\sigma_{e-op} = -d_{e-op}N$$

where N is the photo-excited carrier concentration. Since d_{e-op} is positive this indicates first that in the early stage of excitation there is an expansion of the BT QL's. With a concentration of photo-excited carriers of $N \sim 0.5 \cdot 10^{27} m^{-3}$, the photo-induced stress becomes as large as $\sigma_{-op} \sim -3GPa$. The force that induces atomic motion in case of optical phonons can be defined as:

$$F_{e-op} \approx \frac{\partial \sigma_{e-op}}{\partial x}$$

Because the motion is confined (Fig.5.11) down to $h = 1QL \sim 1nm$ this force becomes:

$$F_{e-op} \sim \frac{\sigma_{e-op}}{h} = 3 \cdot 10^{18} Jm^{-4}$$

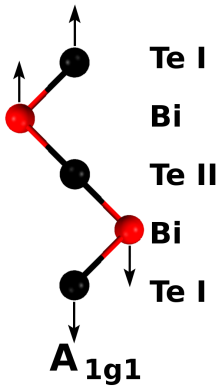

Figure 5.12: A^1_{1g} optical phonon mode in Bi_2Te_3

in magnitude, which is similar to what has been estimated for the A^1_{1g} mode in Bi for an equivalent range of pump excitation [74]. It is worth emphasizing that this force does not depend on the nanostructure thickness. This is the reason why, on the basis of our observations and our theoretical estimates, we believe that this electron/optical deformation potential mechanism could be the driving mechanism of the coherent A^1_{1g} excitation. The photo-induced stress can of course be smeared because of hot electron diffusion, but we think that it should be somehow limited within a QL because of van der Waals contacts. If we consider that each QL is nearly isolated or poorly connected, due to the van der Waals bonds, then the photo-excited carriers can be contained mostly within each QL. We can assume as well that the electrons are evenly distributed within each QL. We can show that, at a Fermi velocity of $V_F \sim 3.6 \cdot 10^5 ms^{-1}$ [75], the distribution of hot electrons over a distance of 10 nm takes 30 fs. The photo-excitation induces an expansion of each QL which corresponds to a 1D-like breathing of each QL. This motion is in agreement with the symmetric atomic motion of the A_{1g} LO mode sketched in Fig.5.12.

The second dominant contribution in the detected signal comes from photo-induced coherent acoustic phonons. The detected acoustic vibrations provide us with information about the elasticity of Bi_2Te_3 in confined geometries and on the electron-acoustic phonon coupling

(Figs.5.13.a-c). Observed light-induced coherent acoustic phonons dynamics for the three samples show a clear difference. Conducted experiments, with a characteristic penetration depth of pump light of $\xi \sim 10nm$, assure us that several QLs are nearly simultaneously excited by the pump beam. Excitation like that allows a simultaneous in-phase motion (mechanical resonance) as already observed in similar experiments on different thin films [76, 77] or nanoparticles [78]. In case of samples from group A we have to take into account the elastic boundary conditions between the BT-substrate interface, to estimate the efficiency of the acoustic phonon confinement. For that we calculate the acoustic reflection coefficient that is defined by [76, 77]:

$$R_{ac} = \frac{Z_{film} - Z_{substrate}}{Z_{film} + Z_{substrate}}$$

Where the impedance $Z = \rho V$ with ρ is the mass density and V is the sound velocity in the material. In the case when the film and substrate impedances are different, then a part of the coherent acoustic phonons is confined. Such situation will lead to out-of-plane vibration of the nanostructures [76, 77]. According to the literature (bulk longitudinal sound velocity $V_{Bi2Te3} = 2600ms^{-1}$ [79], $\rho_{Bi2Te3} = 7460kgm^{-3}$) in case of bulk Bi_2Te_3 the acoustic impedance is similar to that of silicon (100) ($V_{Si} = 8400ms^{-1}$, $\rho_{Si} = 2200kgm^{-3}$) but much larger than that of mica ($\rho_{mica} = 2790kgm^{-3}$ and out-of-plane velocity $V_{mica} = 5027ms^{-1}$ [80]. As a consequence, for a perfect film-substrate interface, we expect no acoustic confinement as in case of sample deposited on silicon. All those conditions are met for film A2, where almost all energy of generated acoustic phonon is being transmitted into the Si substrate ($R_{ac} \sim 0.03$). Generated acoustic phonon is then detected in the substrate with the Brillouin mode signature, whose frequency is $f_{Si} = 2n_{Si}V_{Si}/\lambda = 115GHz$. What is in agreement with our observations (Fig.5.13.e), in case of a probe wavelength fixed at $\lambda = 582nm$ and $n_{Si} = 4$ [81]. In order to better understand this vibration we fitted it with following function:

$$R_{ac}(A2) \sim cos(2\pi f_{A2}t + \varphi_{A2})e^{-t/\tau_{A2}}$$

with $f_{A2} = 111GHz$ and $\tau_{A2} = 24ps$ (dotted line in Fig.5.13.b). On the other hand, for film A1, the detected vibration is not that of a Brillouin nature in the mica substrate. Estimation

of the Brillouin frequency gives $f_{mica} = 2n_{mica}V_{mica}/\lambda = 27GHz$, with $n_{mica} = 1.6$ [82]. The detected vibration observed in film A1 is actually mechanical resonance of eigenmodes due to the confinement of acoustic phonons ($R_{ac} \sim 0.17$). The fast Fourier transformation shown in Fig.5.13.d is a direct evidence of two modes existence:

$$f_1 \approx 80GHz \text{ and } f_2 \approx 160GHz$$

with $f_2 \sim 2f_1$. This is the result of the resonator harmonics generated in this sample, whose frequency is given by:

$$f_n = \frac{nV_{A1}}{2H_{A1}} \text{ , with n = 1,2,3, . . .}$$

where V_{A1} is the longitudinal sound velocity of film A1 and H_{A1} its thickness (Fig.5.8.g). Performed numerical fit using only the fundamental mode gives:

$$R_{ac}(A1) \sim cos(2\pi f_1 t + \varphi_{A1})e^{-t/\tau_{A1}}$$

with $\tau_{A1} = 14ps$ (Fig.5.8.a) gives a very close match with the detected signal. Thanks to this model, we were able to obtain $V_{A1} = 2460ms^{-1}$, which is a very close to theoretical estimates in bulk Bi_2Te_3 ($\sim 2300ms^{-1}$) [83] and estimates obtained in pump-probe experiments performed on $Bi/Sb)_2Te_3$ superlattice (∼2600 m s -1) [79]. Taking the mass density of the stoichiometric Bi_2Te_3 film, $\rho = 7642kgm^{-3}$, we can calculate the elastic constant for axial compression:

$$C_{33} = \rho \times V^2 \approx 36 - 46GPa$$

what is as well in accordance with other calculations [73]. We were able as well to explain with this model vibration detected in sample A3. Contrary to what one may think even (though the film was grown on silicon similarly to A2), we were not able to observe only the Brillouin mode in the silicon substrate. The FFT shown in Fig.5.13.f shows a very small Brillouin signal in Si, with additional modes not resolved yet. A numerical fitting (Fig.5.13.c) has been done with two damped cosinuses frequencies indicated by dotted vertical lines similarly to previous

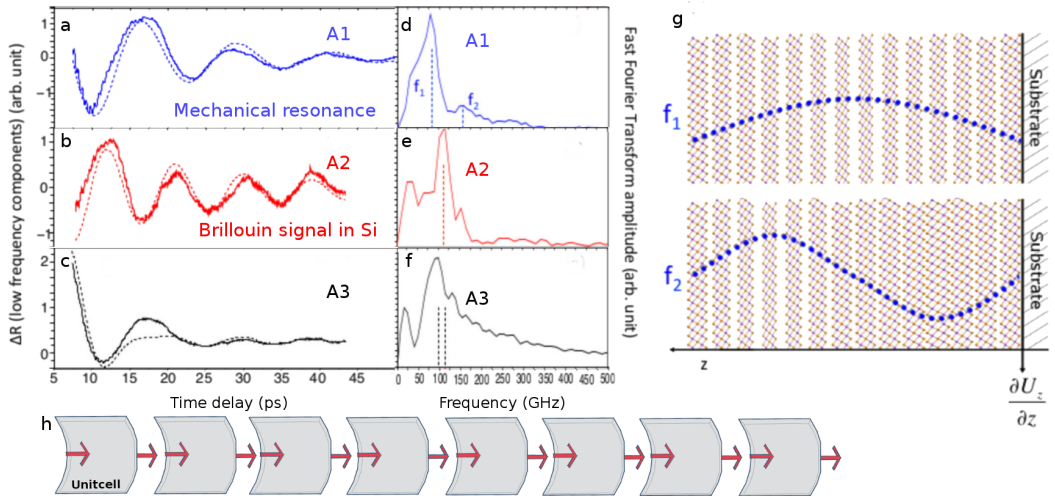

Figure 5.13: a–c Coherent acoustic phonon signals extracted from the transient optical reflectivity signals. For clarity, curves have been scaled in amplitude. Dotted lines are numerical adjustments (see text for more details). d–f Corresponding coherent acoustic phonon spectra obtained by a fast Fourier transform (FFT). (g) The first two confined acoustic eigenmodes in film A1. U_z is the normal displacement of atoms.

two samples (Fig.5.13.c) but it was almost impossible to reproduces obtained signal. One of the explanation of this phenomena would be an existence of complex interfaces and multilayer composition as well as the polycrystalline texture of Bi2Te3 as shown by RHEED page 47. In this situation the sound velocity is a mixture of in- and out-of-plane sound velocity.

For sample A1 probing the assemblies of QLs with coherent acoustic phonons provided us with new insights into the QL van der Waals interactions. What is the case for most of the solids bonded with Van der Waals interaction [76] the macroscopic and mesoscopic elastic modulus originates from the Van der Waals contacts. If we assume that this is the case in sample A1, then it is possible to obtain elastic constant of Te-Te Van der Waals force:

$$C_{VdW} \sim C_{33} \times a_{Te-Te} \sim 12 - 16 Nm^{-1}$$

where the distance between two QLs is $a_{Te-Te} = 0.364nm$ [84]. Our estimates are giving a value that is 1.5 to 2 times larger than previously obtained macroscopic measurements [84]. Of course we have to remember that the constant C_{VdW} is 10 times larger than real Van der Waals interactions that exist in rare gas crystals [73].

Last but not least it is crucial to further discuss the physical origin of the acoustic phonon emission. We can estimate that the driving mechanism of generated coherent acoustic phonon is of an electronic nature. Calculation of the photo-induced thermoelastic stress caused by the rapid lattice heating that follows the electronic decay according to standard model [85] takes form:

$$\sigma_{Th} = -3\beta B\Delta T \sim 0.1 - 0.2GPa$$

with the bulk modulus $B \approx 37GPa$ [73], out-of-plane Bi_2Te_3 thermal expansion $\beta = 2 \cdot 10^{-5}K^{-1}$ [86], and the lattice heating $\Delta T = \Delta E/C_L \approx 60K$, where lattice heat capacity is equal to $C_L = 1.5 \cdot 10^6 Jm^{-3}K^{-1}$ [87] and laser pump energy absorbed per unit of volume $\Delta E = N \cdot 1.495eV \sim 10^8 Jm^{-3}$ (the temperature increase is obtained with a fluence of $0.1mJcm^{-2}$ without taking into account the heat conductivity close to the interface). This thermoelastic stress seems to be much smaller than the stress caused by the electron-acoustic phonon deformation potential given by [85, 88]:

$$\sigma_{e-ac} \approx -a_{e-ac}N = -2.5GPa$$

where $a_{e-ac} = 35eV$ [73] is the electron-acoustic deformation potential (four times larger than in GaAs [67]), and $N \sim 0.5 \cdot 10^{27}m^{-3}$. The dominating nature of the electron-acoustic phonon deformation potential mechanism is in line with the evaluation of this scattering process [28].

5.2.2 Quantum confinement effects

Following section presents the results focused on Quantum confinement caused by scaling down the layer of Bi_2Te_3 [12]. Showcased results gave us a clear understanding at the thickness limits of Bi_2Te_3, that are extremely crucial for development of new devices based on this mate-

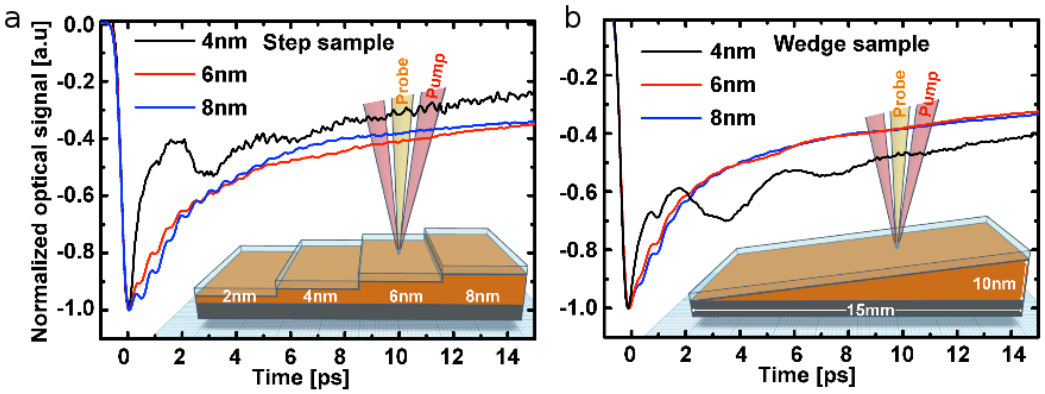

Figure 5.14: Ultrafast optical response of ultrathin layers of Bi_2Te_3 .Time-resolved optical reflectivity obtained for various layers of Bi_2Te_3 for the a - step B1 and b - wedge B2 sample. The signals are normalized to the maximum of electronic peak. (insets) The pump and probe are represented in the artist view as red and orange beams.

rial. The experiments were made with a standard front-front configuration with incident pump and probe beams perpendicular to the surface (hexagonal c axis perpendicular to the surface of Bi_2Te_3, section 2) as shown in Fig.5.9. Pump-probe experiments were conducted with the step sample B1 and wedge sample B2. In our experiments, the pump and probe wavelengths were fixed at 830 nm (1.495 eV) with $\xi = 10.1nm$ and 582 nm (2.13 eV) with $\xi = 9.8nm$ [38]. Such small penetration depth, what was not explained in previous section, is caused by the specific electronic band structure in this energy range where interband transitions exist [38]. The maximum fluence used during the experiment was in the range of $100\mu Jcm^{-2}$ which corresponds to a photo-excited carriers concentration of around $10^{16}cm^{-3}$. Both pump and probe were focused with a microscope objective providing a typical spot radius of $\approx$5 micrometers. With this spot diameter and sample length (along the gradient) of around 1.5 cm (very smooth gradient for the wedge sample Fig.3.8) and a width of 1cm, we were able to investigate many positions along and perpendicular to the gradient. This allowed us to get a very good statistic of transient reflectivity signals that is of utmost importance to reveal subtle properties changes

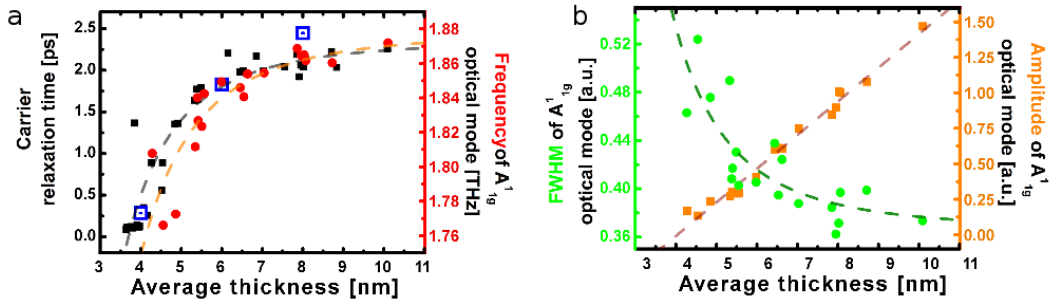

Figure 5.15: Thickness dependence of the ultrafast carrier and phonon dynamics. a - Thickness dependence of the electron-phonon relaxation time for the wedge B2 (black squares) and step B1 (centred blue squares) samples. Thickness dependence of the A^1_{1g} optical phonon frequency (red dots). b - Thickness dependence of the A1g optical phonon amplitude (gold squares) and full width at height maximum (green dots).

as shown in this study.

Obtained time resolved and thickness dependent optical reflectivity signals are presented in in Fig.5.14 both for the B1 and B2 samples respectively. The signals can be decomposed to three parts first one a sharp variation to the transient optical reflectivity that is the consequence of the electronic excitation and can be modelled with error function Eq.5.2. And the second one that describes the decay of the signals both by electronic and thermal dissipation of energy. And the third one with oscillatory components generated by the photo-excitation of different phonons (Fig.5.5 green line - phonon signal). Both of electronic decay and the phonons response were separated:

$$\frac{\Delta R}{R} = \frac{\Delta R}{R}_{electron+thermal} + \frac{\Delta R}{R}_{phonons}$$

where the electronic and thermal contribution is composed of signal due to the excitation of the pump beam and the decay described by two exponential functions. The extracted decay times show the first extremely fast decay time τ_1 ranging from 85fs to 2ps attributed to hot carriers relaxations and a slower part τ_2 with a time spanning from 30 up to 60 ps associated to

long living carriers and thermal relaxation processes (Eq.5.6). For both the step (B1) or wedge sample (B2), we observed a huge modification of the carrier relaxation time (Fig.5.15.a) and phonons dynamics (Figs.5.15). In figure 5.15.a we can see that for thick Bi_2Te_3 layers, the characteristic time of hot carrier relaxation τ_1 is close to $\tau_0 = 2.2ps$ what is very similar to the relaxation of hot carriers (electron and hole) for bulk Bi_2Se_3 [92, 93] and bulk Bi_2Te_3 [94], while for most confined Bi_2Te_3 (especially below 5nm) layers, the electron-phonon relaxation time is drastically evolving down to around 200 fs (Fig.5.10.a), this evolution can be described by the power of law function similar to the energy levels in quantum well system:

$$\tau_{e-ph} = \tau_0 - \frac{A}{L^{\alpha}} \tag{5.20}$$

where L is the thickness of the sample (black dashed line in Fig.5.15.a). This experimental observation indicates that the carriers relaxation process efficiency is almost ten times larger in the thinner Bi_2Te_3 layer than in the bulk like BT layer. We have to point out that we were not to able obtain signal for the thinnest 2nm layer of the step sample B1. The obtained vibrations for thick Bi_2Te_3 films reveal clearly the A^1_{1g} mode at 1.82 THz (Fig.5.16.b) in accordance with the literature [29, 96] and our reference samples (group A).

Presented time-domain optical phonon signals revealed as well an evidence of a slight optical phonon A1g softening (red dots in Fig.5.15.a and 5.16) as well as a decrease of the lifetime (green Fig.5.15.b), that is a direct proof that a modification of the interatomic potentials might occur for the system with a strong confinement. This softening of the A^1_{1g} frequency (around 4%) and raise in the damping time (reverse of FWHM) for ultrathin layers is in line with the observations made in Raman scattering experiments performed on Bi_2Se_3 [91, 97] and in Bi_2Te_3 [98]. The fact that this A^1_{1g} softening occurs both with phonons that are photo-excited with a laser pulse or with thermally excited phonons is one of the clues pointing that the softening does not originate from the hot electrons-driven potential softening (as known for bismuth crystal [99, 81]).

We can say that the size dependence we report is relevant to the entire volume of the deposited layer, based on the observations of band structure thickness dependence which con-

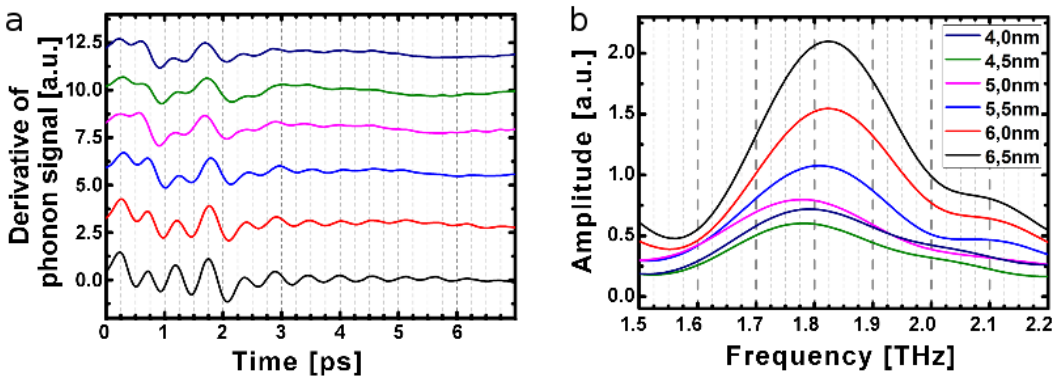

Figure 5.16: a - Typical oscillatory component at short time scale revealing the A1g optical phonon. b - Fast Fourier Transform (FFT) of signal shown in a reveal that the A^1_{1g} mode is softening for ultrathin layer.

firms that the electronic structure evolves for ultrathin layer [9, 100, 101], and the presence of the passivated layer that is a trivial phase in sense of topology should be neutral to the surface states. We can report that the sample thickness (L) dependence is similar to that of the electronic levels (ΔE) in known quantum wells systems that is expected to follow [82]:

$$\Delta E = \frac{A}{L^{\alpha}}$$

were $\alpha = 2$ and can take different power of laws (α) attributed to complex effects of the confinement, such as in the case of nanocrystals [102]. In our study we have fitted the relaxation time according to a phenomenological power law versus thickness L and found that presented above equation describes our system with α = 2.6 and $\tau_0 = 2.2ps$ Fig.5.17. What is surprising similar power of law applies well for describing the softening of the A^1_{1g} optical mode frequency and its life time (Fig.5.15 dashed lines). That is as if a common phenomena correlates these parameters but we do not have theoretical supports at that time.. We have to remember that in our situation TIs nanolayers are confined only in one direction while nanocrystals are 3D quantum-confined systems. We know that we can relate the electron-hole relaxation time to both the matrix element (deformation potential term in the Hamiltonian [103]) and the den-

sity of states (according to the Golden Fermi rule). The relationship between this experimental law and electronic structure that evolves with thickness remains challenging since a full electronic and phonon dispersion curves are needed for bulk and surface states. Fortunately there exists other possible explanations of this phenomena. With the reduction of the system size, the efficiency of carriers surface trapping is known to rise since the probability for the electron to reach the surface per unit of time is much higher when the mean free path of electrons is similar in size to that of the sample thickness. Such surface recombination is the channel of efficient relaxation in semiconductor nanocrystals and the quantum size effect on the electron-phonon coupling [104]. Another interpretation in case of metallic nanoparticles is based on the removal of electron-ion screening interaction caused by lowering the carrier density in close proximity to the surface which contains a large quantity of atoms in comparison to the bulk for few nm nanoparticles with radius R [105, 106]. The following phenomenological equation describing the scattering rates was proposed:

$$\frac{1}{\tau_{e-ph}} = \frac{1}{\tau_0} + \frac{V_F}{\alpha R}$$

where τ_0 is bulk electron-phonon relaxation time, α an adjustable coefficient and V_F is the Fermi velocity [105]. Another interpretation was proposed in case of Bi_2Se_3 thin films, in which the decrease of the relaxation time was attributed to the size dependent Fröhlich interaction [107]. In our case we can think about possible trapping at the oxide cap layer which could lead to increased damping of hot carriers, even if it is difficult at that stage to evaluate this contribution. It has already also been shown that the interband scattering channel range of the bulk-surface occurs up to 5 nm in Bi_2Te_3 compounds [75], what is in perfect agreement to the critical thickness that we estimate and could be a possible indication that the observed anomaly is a crossover from the 3D to the 2D system. Such interpretation is supported by the fact that the coupling between surfaces Dirac fermions wavefunctions from opposite sides of a thin layer has occurs in range of few nm for BS, and what is more is possible to detect even in 10nm films. Additional effect could as well play a crucial role in this process such as possible band bending, that was already observed at the free surface of a bulk crystal [108].

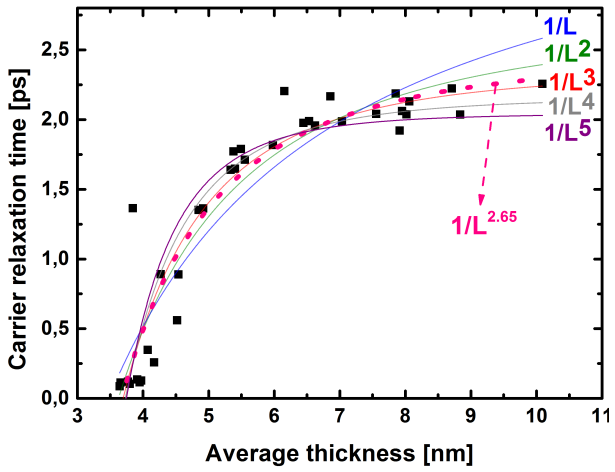

Figure 5.17: Results of fitting the power of law function to the time of relaxation of hot carriers versus the film thickness. Performed calculation resulted with relaxation of the fitting procedure close to $\alpha = 2.65$.

This would suggest that such situation could be enhanced in confined layers of Bi_2Te_3 in close proximity to the opposite surfaces. All the above mentioned factors, the modification of the bulk electronic levels, the surface band bending, the hybridization of two opposite surfaces states, as well as the A1g optical phonon softening that we report, together correspond to a modification of the electron-ion interaction, in other words the deformation potential parameter, which in turn influences the carrier relaxation time rate in the case of electron-phonon collision processes. The particular case of the electron-acoustic phonon deformation is now discussed on the basis of the analysis of the coherent acoustic phonon signal. We can notice first that the assignment of the origin of the acoustic phonon contribution is straightforwardly established by the linear dependence of the period of oscillation with the BT layer thickness as shown in Fig. 5.18b. Secondly (as shown in Fig 5.19) that the acoustic phonon signal is highly size dependent and exhibit a resonant-like behaviour for a thickness around 5nm. We try to propose an explanation in the following discussion.

Due to evolution of electron band structure with thickness in TI, the electron-hole acous-

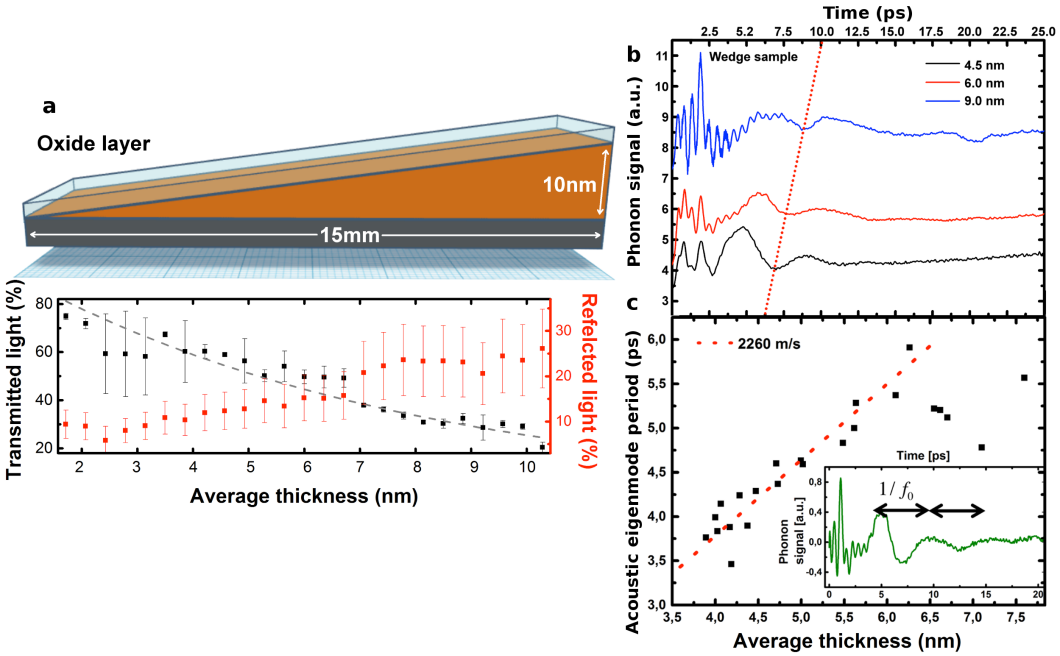

Figure 5.18: a - Art view of the cross section of the C2 wedge sample together with continuous wavelength optical transmission, with dashed curve we presented calculated Beer-Lambert law, and with red reflectivity along thickness gradient. b - Contribution of the phonons signal to the transient reflectivity signal for three different thickness. d - Thickness dependence of the longitudinal acoustic resonance eigenmode period $1/f_0$. The red dashed slope provide estimation of the longitudinal sound velocity $2260m/s$ in Bi_2Te_3. Inset shows example of acoustic signal with the period $1/f_0$ for 6nm layer.

tic deformation potential is dependant on thickness of the material [9, 101]. In order to find the thickness dependence of the deformation potential we have to consider that the excited electrons (and holes) rapidly thermalize down(/up) to the CB(/VB) (Fig.5.4), in this case the relevant deformation potential is d_{33} which is close to the band gap E_g [59, 60, 63]:

$$d_{33}^{ac-eh} = \frac{\partial E_g}{\partial \eta_{33}}$$

This approximation is met when the frequency on the detected acoustic oscillation is smaller than inverse of the time of thermalization in the CB and VB. The discussed acoustic phonons correspond to the thin film eigenmodes, i.e. those inducing an out-of-plane strain η_{33}. The strain associated to the acoustic eignenmode is directly connected to the layer thickness change (dL) with:

$$\eta_{33} = \frac{dL}{L}$$

in consequence the electron-hole acoustic phonon deformation potential takes form:

$$d_{33}^{ac-eh} = L\frac{\partial E_g}{\partial L}$$

The information about the band gap dependence is available in literature for Bi_2Se_3 and Bi_2Te_3 compounds [9, 101], this allowed us to estimate the experimental parameter $L\frac{\partial E_g}{\partial L}$. The evaluated thickness dependence is presented in Fig.5.19.b (blue curve), it clearly reveal the enhancement of the deformation potential parameter when reducing the thickness. In presented graphic we normalized received value to the maximum of the experimental amplitude for easier comparison. There is however a clear deviation for ultrathin layer where the calculated deformation potential cannot explain the sudden decrease of the experimental phonon amplitude. We believe that this effect comes from a detection process that can be numerically estimated as described below. We have realized a calculation of the contribution of coherent acoustic phonons to the transient optical reflectivity (detection process) by considering that none of the physical parameters change but only the thickness is reduced. To do that we have calculated the coherent acoustic phonon contribution to the transient optical reflectivity following the

standard method [109, 110, 111]. We have performed this calculation by considering the first acoustic eigenmode (f_0) strain field contribution whose standard expression is:

$$\eta_{33}(z,t) = A \times sin\left(\frac{\pi z}{L}\right) e^{i\omega_0 t}$$

where A is the amplitude and $\omega_0 = 2\pi f_0$. We can show that the contribution of deformation potential to the transient optical reflectivity can be calculated with the standard model where the optical reflectivity magnitude for normal incidence pump-probe experiment Eq.4.3 would possesses an acoustic phonon contribution [109, 110, 111]:

$$\left(\frac{\Delta R}{2R}\right)_{ac-ph} \approx Re[-4i \times C \times r_{12} k_1 \frac{L}{\pi} e^{i\omega_0 t} \tag{5.21}$$

$$-iC\frac{\partial k_1}{\partial \eta_{33}} \int_0^L A \times sin\left(\frac{\pi z}{L}\right) e^{i\omega_0 t} \left(r_{12} e^{-ik_1[L-z]} + e^{ik_1[L-z]}\right)^2 dz]$$

with optical parameter C dependant on optical parameters of Bi_2Te_3 is:

$$C = \frac{1 - r_{01}^2}{r_{01} e^{ik_1 H} + r_{12} e^{-ik_1 H}} \times \frac{1}{e^{ik_1 H} + r_{01} r_{12} e^{-ik_1 H}}$$

where r is the complex optical reflectivity coefficient of the non-perturbed system, k_i is the probe wavevector in medium i (0, 1 and 2 are respectively air, BT layer and the Mica substrate) and u(z) is the normal mechanical displacement of the transparent layer at a position z. The notation r_{33} is used for the optical reflection coefficient at the interface between medium i/j for oblique incident probe beam whose polarization is perpendicular to the incidence plane:

$$r_{ij} = \frac{n_i - n_j}{n_i + n_j}$$

The first term of eq.5.5 corresponds to an interferometric contribution due to the change of the transparent layer thickness induced by the relative interfaces displacement driven by the acoustic strain field. The second term corresponds to the photo-elastic contribution i.e. that due to the modulation of the refractive index by the coherent acoustic phonons strain field. The strain field is coupled to the internal probe light electric field given as the second term (in brackets) in the integral. $z = 0$ corresponds to the free surface of Bi_2Te_3 layer. In this model

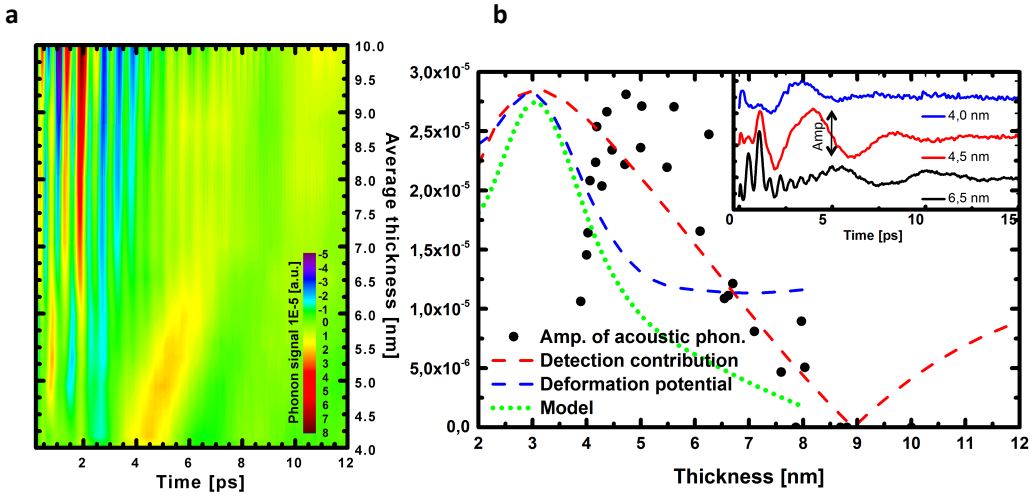

Figure 5.19: Scaling down layer of Bi_2Te_3 revealed generation of strong coherent acoustic phonon. a - Map of the optical and acoustic phonon mode amplitudes with fixed pump power, x-axis represent time and y-axis change of layer thickness. Experiment revealed appearance of large acoustic phonon signal in ultrathin layer. b - Thickness dependence of the photo-detected coherent acoustic signal amplitude. Green curve present model that takes into account the detection (red) contribution, estimated size dependant electron-hole acoustic deformation potential (blue) from the literature [9].

we omitted the contribution from the passivated oxide layer. The photo-elastic coefficient $\partial k_1/\partial \eta_{33}$, it can be derived according to:

$$k_0 \frac{\partial n_1}{\partial \eta_{33}} = k_0 \frac{\partial n_1}{\partial E_{probe}} \times \frac{\partial E_{probe}}{\partial \eta_{33}} = k_0 \frac{\partial (n_1^{'} + i n_1^{''})}{\partial E_{probe}} \times \frac{\partial E_{probe}}{\partial \eta_{33}}$$

where k_0 is optical wavevector in vacuum and $\dfrac{\partial E_{probe}}{\eta_{33}}$ the deformation potential coefficient at the probe energy, $n_1 = n_1^{'} + i n_1^{''} = 1.7 + i4.5$ is the Bi_2Te_3 refractive index at the probe energy $2.2eV$ [38], and that gives. The refractive index of Mica was taken as $n_2 = 1.6$. Equation 4.5 gives time dependant sinusoidal function of transient optical reflectivity signal with corresponding frequency eigenmode. Presented maximal amplitude is not absolute one due to lack of the value of deformation potential at the probe energy. It still gives us the ability to discuss the thickness dependence L. Assuming that the sound velocity of the Bi_2Te_3 does not change (Fig.5.18.c), we can say that the amplitude is proportional to the electron-hole deformation potential d_{ac-eh} and the photo-excited carriers concentration N only as [59, 60]:

$$\eta_{33}(z,t) = A \times sin\left(\frac{\pi z}{L}\right) e^{i\omega_0 t} \propto N(L) \times d_{33}^{ac-eh} \times sin\left(\frac{\pi z}{L}\right) e^{i\omega_0 t}$$

Because optical properties of Bi_2Te_3 do not show a drastic change at the probe energy, what has been shown with Beer-Lambert law (Fig.5.18.a), we can estimate that the carriers concentration versus thickness is roughly multiplied by two in 4nm compared to 10nm layer. This allowed us to calculate thickness dependence of the maximum of amplitude of the detected acoustic vibration (red dashed curve Fig.5.19.b). As stated before it is impossible to compare directly the absolute values but only the thickness (L) variations, because of this reason we normalized the curve to the maximum of detected amplitude in order to be able to discuss the tendency. Presented detection mechanism seems to reproduce the enhancement of the coherent acoustic phonon as well as the lowering of the detected signal in ultrathin layers. By including into this calculation the thickness dependant deformation potential we are able to obtain (Fig.5.19.b green dotted curve) model of the observed effect. Presented curve show similarities in the appearance of the maximum and broadness but show as well a clear shift

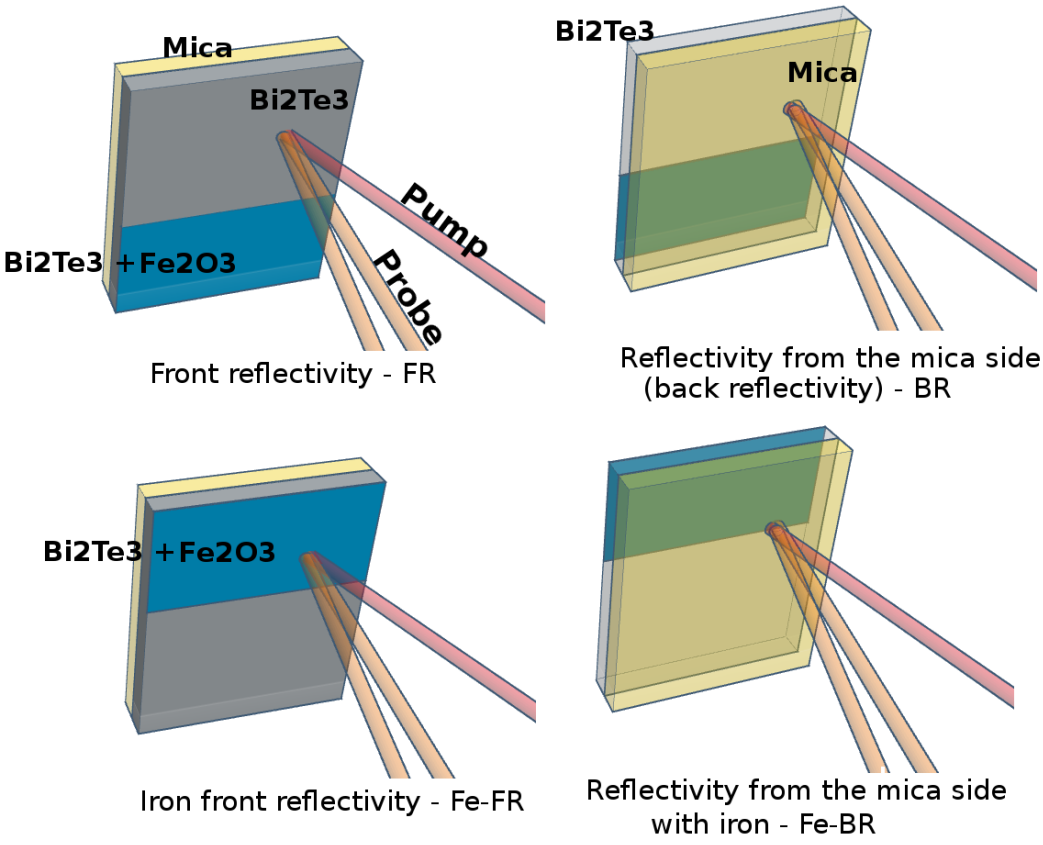

Figure 5.20: All performed configurations of reflectivity measurements made with iron sample.

between the theory and the experiment that is probably due to the necessary approximations, such as value of $L\frac{\partial E_g}{L}$, as well as considering that the photo-elastic coefficient in thickness independent what is likely not true.

5.2.3 Influence of iron oxide capping layers

Study of topological insulators entered the state of finding the best possible systems to harness their unique properties. Current study is mainly focused on spin-charge current conversion that requires presence of ferromagnetic layer or material with strong spin orbit coupling [5, 6, 7]. Realization of such devices requires from us the understanding of the deposited lay-

ers interactions with topological insulators and understanding of both physical and chemical aspects of those interfaces. In this experiment we focused on changes of hot carrier relaxation time and phonon dynamics in Bi_2Te_3 structure, caused by the close proximity of Fe^{3+} oxide interface, that was in line with previous investigations [34]. In our experiments we used the laser pump with wavelength equal to 830nm (1.49eV) and 415nm (2.98eV) and the probe beam with a wavelength of 580 nm (2.14eV), that is close in energy to the reported indirect band gap of $\alpha - Fe_2O_3$ at 2.1eV [112, 113, 114] and similar to the direct band gap of $\gamma - Fe_2O_3$ [115, 116, 117]. Considering these optical properties, we can consider that the iron oxide is nearly transparent at both the pump and probe wavelength. Thanks to that we can be sure that our pump and probe beams were highly transmitted through the iron oxide layer, and the excited processes were generated mainly within the layer of Bi_2Te_3. As shown in the previous section (see part 5.2.2), the dynamics of hot carrier dissipation after the optical excitation can be robustly changed by the modification of the bulk electronic levels, the surface band bending or the hybridization of two opposite surfaces states. The experiments, conducted on the sample C1 covered partially with iron oxide were made with both transmission and reflection geometries, from mica and free surface side (Fig.5.21). This experiment revealed a strong modification of the relaxation time of the hot carriers τ_1 (table 5.1) that at the first sight looks very similar to the situation observed in the case of quantum confinement evidenced for the layer of Bi_2Te_3 thinner than $5nm$ Fig.5.15. On the contrary, the dynamics of hot carriers measured on the sample area where no iron was deposited looks like the signal obtained for "bulk" BT material (see Fig. 5.9 and 5.14).

It is worth to mention that similar relaxation time scales were observed in case of both $\alpha - Fe_2O_3$ and $\gamma - Fe_2O_3$ nanoparticles with decay times spanning from 0.36 up to 67ps [114, 118]. The process was attributed to the recombination of electron-hole govern by intrinsic mid-bandgap states and internal defect-induced trap states, and surface defects that create additional fast channel of carrier relaxation (Fig.5.21.c). Similar situation was also observed in case of $LT : GaAs$ [119], in which the excess of As within the structure is dramatically re-

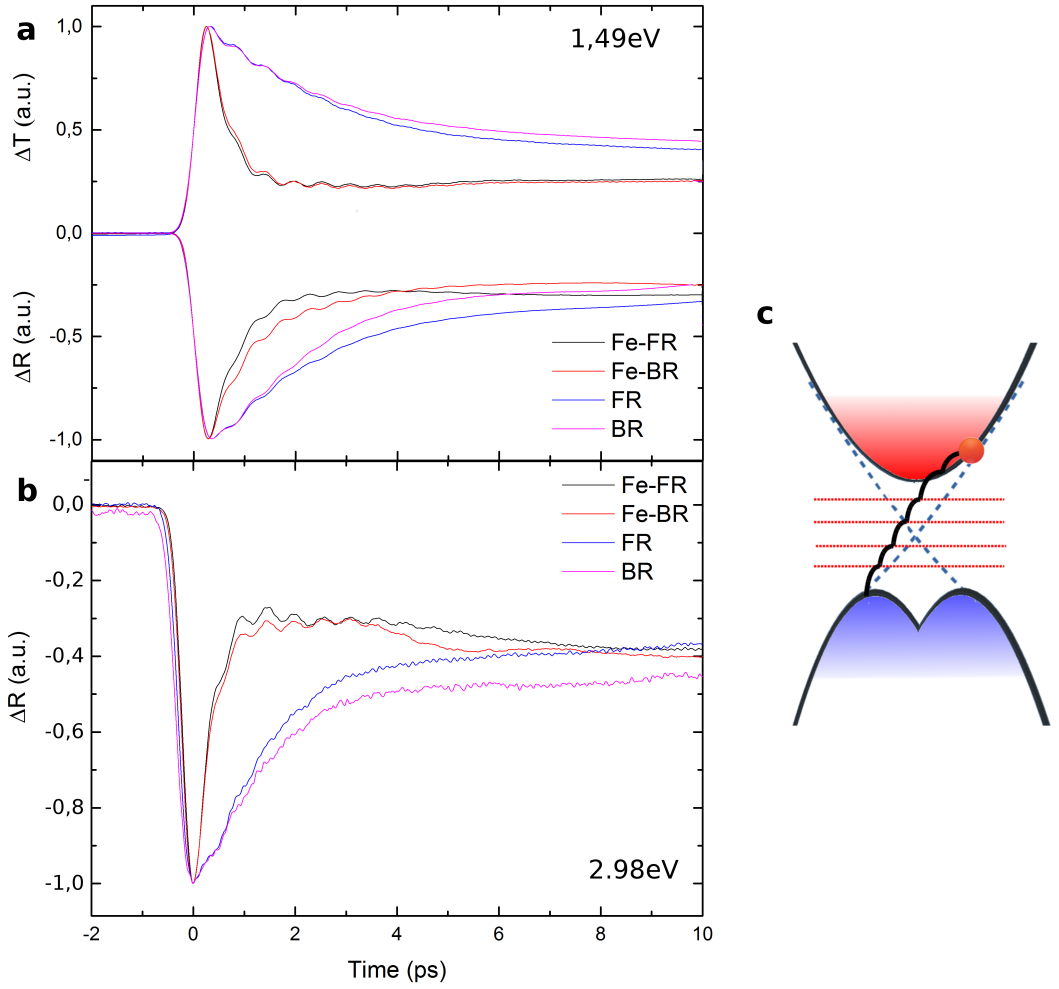

Figure 5.21: a - Time-resolved optical transmission (ΔT) and reflectivity (ΔR) obtained for the sample C1 with a pump wavelength 830nm. Signals, marked with Fe, were made on a part of sample with iron oxide, the letter B denotes the position of excitation by pump from the back side (mica side) similar for the front (F). The letters T and R are denoting transmission and reflection. b - Time-resolved optical reflectivity (ΔR) obtained for the sample C1 with a pump wavelength 415nm. c - Schematic of the relaxation process of photo-excited carriers in presence of mid-bandgap states induced by the close proximity of $\gamma - Fe_2O_3$ atoms within the structure of Bi_2Te_3.

ducing the life time of the photo-excited carriers and shows linear change with the precipitate spacing. Because of defects in the band gap, the recombination of the e–h pairs can be as fast as few ps.

In our situation, due to the pretty large band gap of iron oxide, as said previously, we can exclude the contribution from the intrinsic response of iron oxide. However, as presented in Fig. 4.21, the depth profile analysis revealed, aside of the presence of the $\gamma - Fe_2O_3$ layer directly on top of Bi_2Te_3, possible appearance of diffused iron atoms within the Bi_2Te_3 structure. This iron atoms in insertion as sketched in the inset of Fig. 4.21, can act as a defect and can create some states in the band gap (or elsewhere) in the BT band structure. As a consequence, this scattering centres may accelerate the hot carriers relaxation. But the existence of the iron oxide on the top of the layer may also have a contribution and may change the electronic structure of the BT layer. Existence of such material near the surface states of topological layer can indeed lead to a strong modification of the topological spin structure as already reported in iron doped $Bi2Se_3$ [120, 121]. Contributed to such doping, strong Coulomb and magnetic perturbations are breaking the formation process (Fig.2.1) of TI by directly influencing two crucial steps of Dirac cone formation, the crystal field symmetry and the spin-orbit interactions. As reported by the direct ARPES measurements [120] such situation leads to band gap opening in TI surface, what is very similar to the situation caused by scaling down the layer [9] that we have discussed in the part 5.22.

As a summary, at this stage, forth origin of the fast relaxation process we evidence, we cannot disentangle the contributions coming from the possible scattering centres (created by the inserted Fe atoms) and the one coming from a possible strong magnetic interaction, that modifies the electronic structure, and consequently the electron-phonon coupling parameters. Despite this current limitation, we show that the interaction of iron cap layer with very thin BT layer can be complex. This is again supported by the following discussion regarding the optical phonon (A1g) dynamics.

Beside of the modification of the hot carriers life time the time-resolved femtosecond

Table 5.1: Extracted with the fitting function E.q.4.1 relaxation times of hot carrier for the sample C1.

Name	τ_1	Name	τ_1	Name	τ_1	Name	τ_1
Fe-FT	350fs	Fe-BT	400fs	FT	2260fs	BT	2090fs
Fe-FR	560fs	Fe-BR	1050fs	FR	2090fs	BR	1990fs

pump-probe spectroscopy revealed indeed a clear difference in excitation of the A^1_{1g} optical phonon mode in presence of iron oxide doping Fig.5.22. Thanks to the specific design of the samples from the group C, where the clean part could be used as self reference, we were able to directly compare properties such as frequency and amplitude of the generated phonon. Such approach was necessary due to higher sampling rate (number of steps of the delay line), used in this experiment, that can directly affect the frequency of the detected vibrations but provides us with much better frequency resolution. All presented data were gathered during short span of time, in order to assure exactly the same condition and parameters (such as stability of the laser, humidity, temperature, etc.) of the experiment. In presented signal we can see a clear enhancement of the amplitude of the generated coherent optical mode which is accompanied by a slight stiffening of A^1_{1g}. In fig 5.22.b we superimpose the derivative of the transmitted phonon signal, where we can clearly see a difference in the frequency of excited optical mode between doped (from FFT $f_{Fe} \approx 1.82Thz$) and un-doped (from FFT $f_{BT} \approx 1.80Thz$) side, the difference is at the level of about $1,1\%$. The blue shift of optical phonon mode was observed previously only as a function of the pump fluence or the temperature in material such as graphene, V_2O_3 or gold [122, 123, 124]. In the case of gold, performed ab inito calculations revealed that the blue shift of the phonon modes is induced by the rise of photo-excited electrons temperature (T_e from TTM model) that results in increase of the crystal's melting temperature [125, 126, 127]. This phenomenon was qualitatively explained by enhanced electronic delocalization accompanied by decrease in screening of the attractive nuclear potential leading to effective bond hardening [125, 126]. In the case of graphene, the transient stiffening of the G-mode phonons

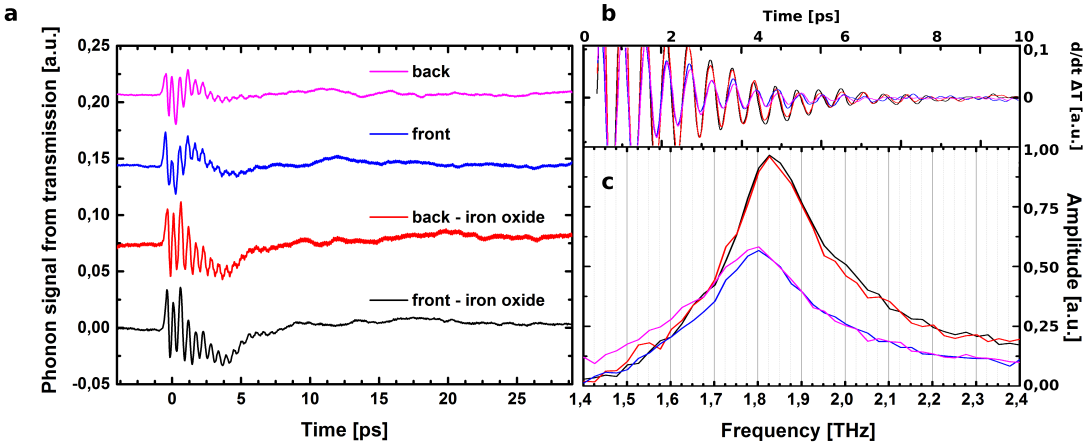

Figure 5.22: Time-resolved transmission (ΔT) obtained for the sample C1. Graph a presents the extracted phonon signals. b - presents overlapped derivatives of the signal showing, in the real time, the difference in frequency. Graph c presents the FFT showing appearance of blue shift of A^1_{g1} frequency in Bi_2Te_3 doped with iron oxide.

has been attributed to reduction of strong electron-phonon coupling. In situation when Fermi energy is close to the Dirac point, G-mode phonons can efficiently decay into electron-hole pairs. However, in situation when Fermi energy has been shifted from the Dirac point, the process of quick relaxation can be no longer available once the required electron and hole states are no longer present. Such electronic decoupling can lead to an increase of the phonon energy [122]. In the case of the V_2O_3 hardening of the A_{1g} mode was explained by decrease of the average distance between two closest vanadium atoms induced by the bonding properties of the a_{1g} orbitals. This effect was observed experimentally and confirmed by the $LDA+U$ calculations [123].

With the intention to better evidence this unique blue shift of the A^1_{1g} optical phonon mode frequency, we prepared the sample C2. The geometry of this sample, similar to the sample B2, allowed us to perform continuous study of the influence of iron oxide layer on the properties of Bi_2Te_3. In figure 5.23.a we presented the FFT signal coming from the wedge sample

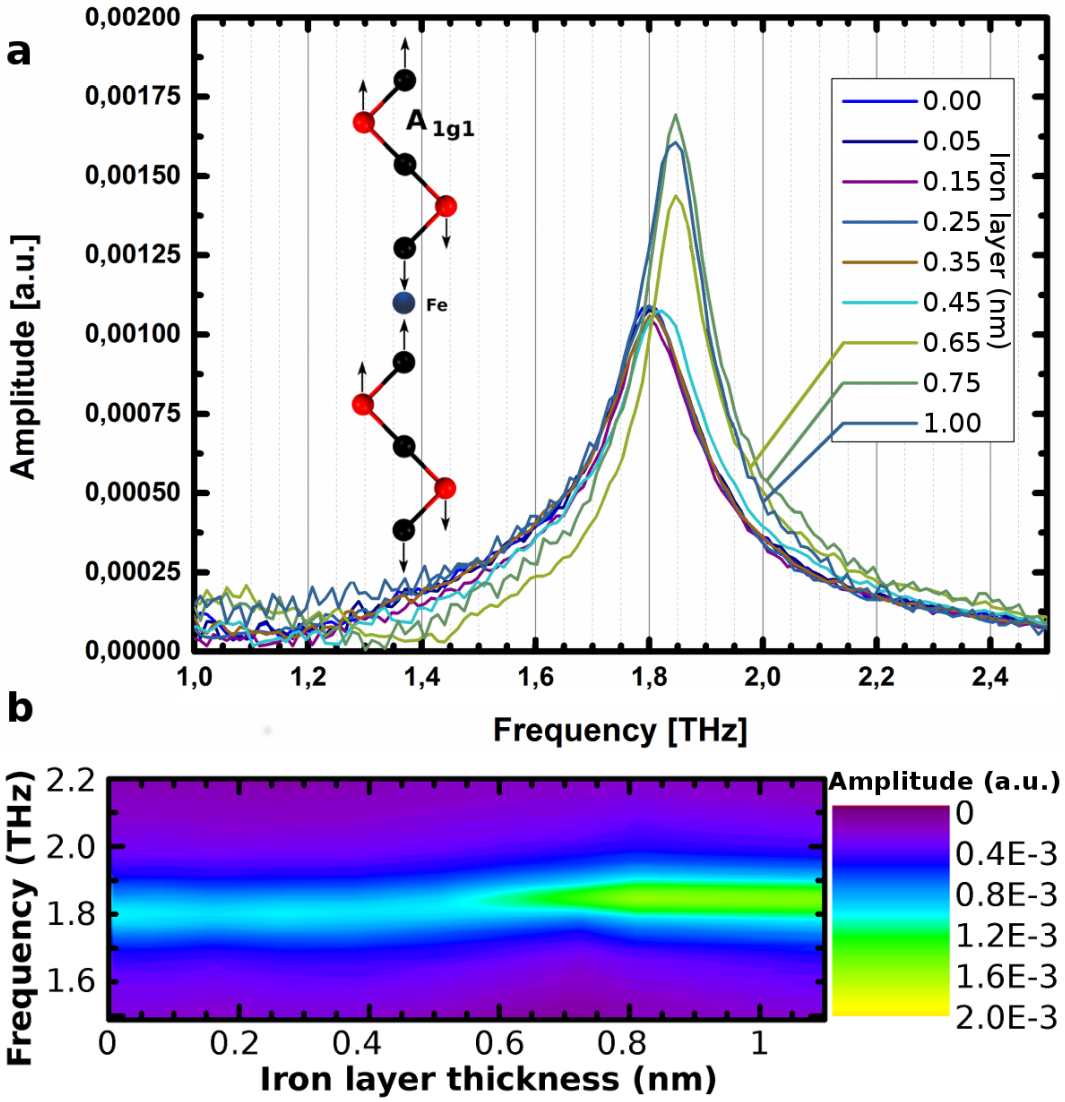

Figure 5.23: a - FFT amplitude from measurements performed on the sample C2 with iron wedge, Signal revealed that the blue shift has discreet nature dependant on quantity of doping. The frequency shift appears when the relaxation time of photo-excited electron is faster than $\tau_e < 0.9p$. b - Schematic of A^1_{g1} optical phonon mode in presence of iron in between VdW layer.

that revealed discrete character as a function of the amount of deposited iron on the phonon hardening. The presented data clearly show the same shift in frequency as in the sample C1 from $f_{BT} = 1.80THz$ to $f_{Fe} = 1.82THz$ and the same enhancement of the detected phonon amplitude that occurs when the deposited layer of iron is larger than $0.5nm$. In fig.5.23.b we presented the map with larger quantity of measured points of the detected optical phonon frequency (and amplitude in color) as a function of deposited capping layer thickness. Revealed stiffening of the optical phonon mode can originate from modification of the bonds under light excitation. Similarly to the photo-doping effect which modifies the interatomic potential and in result leads to evolution of the molecular bonds. In order to confirm this explanation we are planing to conduct a study of the pump fluence dependence in the future. The second explanation of the observed phenomena is based on the shift of the Fermi level due to the presence of Fe in the structure, that according to the presented before depth-profiling can be accumulated in between the VdW layers. In this case the presence of additional structures can lead to change in interatomic potential of Bi_2Te_3 QL's leading to stiffening of the A^1_{1g} mode. Such stiffening has already been observed on a transverse optical phonon dynamics, in multilayers of graphene [128]. This optical phonon mode was associated to a shear motion between neighbours layer of graphene. It was shown that the increase of the number of graphene layers increased the electrostatic interaction between each layer, leading to a final hardening of the elastic constant and consequently to the blue shift of the phonon frequency. We could imagine a similar scenario in our case even if modeling and additional experiments are necessary to conclude. In any case, this experimental results shows again the necessary detailed investigation of the composite structure associating a cap layer (in that case an iron cap layer) and the BT layer.

Chapter 6

Summary

As a conclusion, in this work we wanted to address few problems concerning the topological insulators, in particular bismuth telluride. Bi_2Te_3 due to its vast potential in future electronics requires from us a better understanding of the limiting factors, that could put a barrier in future applications. As mentioned before one of the phenomena that so far it was disregarded in the literature was the role of electron-phonon coupling (with A^1_{1g} mode mode [27] and strong coupling of 2D surface electrons with LA mode [28]) that set a limit on 2D surface electron transport. Knowing that, we tried to tackle this question with complete and thorough chemical and physical investigation performed on films from group A grown by state-of-the-art molecular beam epitaxy. This group consisted of three samples one of witch was deposited on Muscovite Mica and two deposited on Silicon (001). During their growth we tried using different parameters of growth to see how they influence the quality of deposited material. We manage to show differences in crystal structure between sample from this series. In case of sample A1 the diffraction image form RHEED experiment showed a clear presence of very small terraces that posses two characteristic to the hexagonal cell patterns. The formation of the crystal and its stoichiometry was confirmed as well by the LEED image and XPS spectra (Bi/Te - 46/54). In case of samples A2 and A3 the RHEED image revealed formation of polycrystalline structure that probably originated from the mismatch between Bi_2Te_3 and silicon

(001) substrate. Performed XPS revealed as well that both samples A2 and A3 were rich in Te (A2: 35/65; A3: 33/67) and such composition is causing formation of the interlayers of Te in between the Van der Waals layers of Bi_2Te_3 [50]. Finally due to diligent analysis of the deposited structures we were able show with ultrafast two-color pump-probe technique, that it is possible to excite a coherent A^1_{1g} LO mode in thin films containing 10 QLs of Bi_2Te_3 with no detectable restriction in their emission, contrary to what was suggested previously in the literature [41]. The A^1_{1g} phonon dynamics is nearly not disturbed by the nanostructure of the films, which indicates that the phonon decay takes place locally by anharmonic coupling rather than by scattering due to geometrical inhomogeneities like islands or grain boundaries. Our estimates show that the optical-phonon deformation potential photo-induced stress appears to be as high as -3GPa for a photo-excited carrier concentration of $N \sim 0.5 \times 10^{27} m^{-3}$, which is quite large and likely to launch atomic motion of the A^1_{1g} mode in our nanostructures. It is important to note here that we did not detect two different A^1_{1g} mode components arising from the so-called bulk and surface phonons as reported on bulk Bi_2Se_3 with time-resolved angle-resolved photo-emission spectroscopy [92]. The origin of the difference is not clear yet, since this could be either due to the confinement of our nanostructures or due to the lack of sensitivity of optical methods even if in the particular case of Bi_2Te_3, the pump/probe light penetrates only around 10 nm, which is still a characteristic distance over which surface and bulk electrons may interact [75]. Besides the A^1_{1g} phonon dynamics, we also show, before the A^1_{1g} mode decays, the birth of coherent acoustic phonons whose spectrum drastically depends on the film's nanostructure, contrary to that of the A^1_{1g} mode. This clearly shows the sensitivity of the longitudinal acoustic modes to the nanostructure arrangement. The generation mechanism of these acoustic phonons is also attributed to the deformation potential mechanism. Finally, the measurement of the time of flight (sound velocity) of these longitudinal acoustic phonons in the single-crystalline film (A1) provides an evaluation of the out-of-plane elastic modulus (36–46 GPa) of these assemblies of QLs.

The second task that we wanted to adress with this work was enhancement of the surface

states contribution into overall properties of the topological insulator material. In case of ultra thin films the ratio of surface states to bulk states starts to be not negligible, in the case of thin films, at a critical thickness the surface states from opposite surfaces of the films can couple together and open thickness-dependent gap (Fig.2.4) [9, 31, 32], which is non trivial and may give rise to quantum spin Hall state similarly to HgTe quantum wells [33]. In order to gain better understanding of the processes of electron and phonon dynamics, under working conditions or exposure to air we created second group B of the samples. Thin film in this series were created in order to better understand the influence of critical thickness in the Bi_2Te_3 [9, 31, 32, 33] on electron and phonon dynamics. We managed to deposit two unique samples on Muscovite Mica with different geometry: one with large steps (that grants us an access to large surface area with uniform thickness that provides a precise description of the thickness dependence), second one with continuous slope (that allow us to conduct experiments with higher number of investigated spots). Chemical and physical investigation of the structural properties of the samples from group B revealed that the deposition technique developed for sample A1 gives stable and repeatable high quality films of Bi_2Te_3. Due to unique opportunity given by planned variation in thickness we were able to revile that layers of Bi_2Te_3 have tendency to grow with Stransky-Krastanov dynamics. Similarly to sample A1, films from group B shown stoichiometry rich in bismuth, that should in result give a stable superstructure Bi-BT within the QL's. Performed after the oxidation XPS, measurements revealed existence of passivated layer ($\sim 2nm$) of Te and Bi oxides, that is stable in time and acts as protective layer from further degradation of deposited layers. Due to diligent preparation of this set of samples, we were able to reveal in this work a clear modification of the out-of-equilibrium carriers and phonons dynamics when the Bi_2Te_3 layer is reduced to few nanometers. Performed time-domain investigation provided us with a new insight in to the size-dependent physical properties of topological insulators, while in the past the size-dependent electronic properties were probed only at the thermodynamic equilibrium. We were able to show a drastic decrease of the electron-phonon relaxation time with an increase of the confinement that before that

was only fully described for semiconductor and metallic nanostructures, while only partially characterized regarding its ultrafast response for BS layers for example [107]. It was possible to assign this effect to a size-dependent electron-hole phonon deformation potential parameter which still needs to be confirmed by ab-initio calculation. One of the most interesting phenomena observed in this experiment was increase of the coherent acoustic phonons signals with decreasing thickness (L) that could be explained by a enhancement of the electron-hole acoustic deformation potential parameter. The performed experimental optical measurement integrates bulk and surface electrons into the final response, but non negligible surface carriers contribution could exist since our film thickness scaled down with the characteristic to Bi_2Te_3 distance for surface Dirac fermions states to hybridize. Unfortunately it is difficult to give a quantitative estimate by of separated contributions to the received signal. Apart from the quantum-confinement effect contribution of the carrier surface recombination could as well enhance the carrier relaxation time, especially in close proximity to the oxidised layer. All these new physical insights showed us that downscaling the layer of topological insulators is changing its properties in not straightforward ways that have to be taken into account for potential TIs based spintronic nanodevices.

The last question that we wanted to address in this work is related to creation of new devices, that would efficiently use the properties of TI's. Mainly reaction of bismuth telluride to the presence of doping and additional layers [34]. Due to necessity of using ferromagnetic (Fig.2.5) or metallic layers with strong spin orbit coupling like platinum or cobalt [5, 6, 7], to create working spin-current converters, we have to be able to create stable chemically systems, that would not disturb the topological insulator surface states and would still allow the transfer of generated polarized spin current into other layers. To better understand this processes we created the last group of samples C . The synthesized films possessed additional oxidized iron layer. For this study we created two samples one with uniform thin cap of iron ($\sim 1nm$) covering half of the sample and second similar to sample B2 with uniform continuous wedge of iron ($1nm \rightarrow 0nm$) deposited on $15nm$ layer of Bi_2Te_3. Such configurations gave us means to

directly compare the effects induced by the presence of other materials, on both crystal structure as well as phonon and hot carrier dynamics. Thanks to the design, half of the surface was not covered by the iron element which consequently permitted us to have an in-situ reference. By this we were able to eliminate effects that could be induced by different growth conditions, and give us chance to directly compare the measured signals. With performed X-ray photoelectron spectroscopy we were able to identify the state of iron ($Fe3+$) and type of the formed oxide ($\gamma - Fe_2O_3$). In order to better understand the created structure we performed depth profiling of the layer C2 (with iron wedge) that revealed presence of iron within the structure of Bi_2Te_3. Lack of change in energy of core levels of both Bi and Te, characteristic to formation of Bi_2Te_3, lead us to conclusion that the additional iron within the layer might be in oxidized form or in compound with Te. The formed compound containing the iron element, seems to not disturb the Bi_2Te_3 structure. The informations, received after the analysis of the depth profiling, allowed us to create possible model,for the Fe-doped superstructure, that was presented at the end of chapter 4. Time-domain investigation revealed first a strong modification of the photo-excited carriers. In particular the Fe-doped system exhibit a very fast electron-phonon relaxation thermalization time in comparison to the iron-free layer. The observed phenomenon could originate from the change in electronic band distribution caused by the close proximity of iron within the structure. Such doping within the TI layer can directly influence the Fe-doped layer through a change in the crystal field symmetry and/or through a strong spin-orbit coupling. Consequently, the electron-phonon matrix element would be drastically modified. This possibility has already been discussed in the literature [120,121], but our detailed sample characterization show that we have to be careful, since we evidenced some possible migration over a couple of nanomaters of the Fe element. Therefore, this information could indicated that we form some mid-gap states or internal change in crystal field symmetry and spin-orbit interaction, that still has to be confirmed numerically. Effect like that could as well originate from appearance of additional mid-bangap states or internal defect-induced traps that allow fast relaxation of carriers. The second effect that was observed in this study a clear, even small, blue

shift of the A^1_{1g} optical mode. Such hardening of the optical phonon mode was only observed in materials such as graphene, gold or V_2O_3. The revealed stiffening can originate from two possible mechanisms, similar to photo-doping evolution of molecular bonds or similar to the case of graphene shift of the Fermi level, in presence of iron compound between QL's. This presented explanation still requires further study of the material. After achieving the promising results from this set of samples, we launched two scientific programs. Their main goal is further investigation of the metallic (Fe, Pt, Ag, Cu, Co and Au) interfaces interactions with TI layers, in order to find the optimal structures that could be used in future electronics. The future study will be expanded by addition SQUID, PEEM, ARPES and time resolved Kerr effect and ellipticity rotation.

Chapter 7

Appendix

7.1 Second harmonic generation

Second harmonic generation can occur in crystal materials which lack inversion symmetry and can exhibit so-called $\chi^{(2)}$ non-linearity. This can give rise to the phenomenon of frequency doubling, where an source (pump) wave generates another wave with doubled optical frequency in the medium. In most cases, the pump wave is delivered in the form of a laser beam, and the frequency doubled (second-harmonic) wave is generated in the form of a beam propagating in a similar direction

To better understand the basic concept we should approach it from theoretical point of view. Let us expand the polarization P as power series in energy, in result we receive:

$$P(t) = \varepsilon_0[\chi^{(1)}E + \chi^{(2)}E^2 + \chi^{(3)}E^3 + ...] \tag{7.1}$$

Because $\chi^{(1)} >> \chi^{(2)} >> \chi^{(3)} >> ... >> \chi^{(n)}$ and $\chi^{(3)}$ is very small we can leave only two parts:

$$P(t) = \varepsilon_0[\chi^{(1)}E + \chi^{(2)}E^2] \tag{7.2}$$

Now let us consider the simplest electromagnetic wave in shape of cosine function:

$$E(t) = E_0 cos(\omega t) \tag{7.3}$$

and insert it to the simplified equation, we will receive:

$$P(t) = \varepsilon_0[\chi^{(1)} E_0 cos(\omega t) + \chi^{(2)} E_0^2 cos^2(\omega t)] \tag{7.4}$$

$$P(t) = \varepsilon_0[\chi^{(1)} E_0 cos(\omega t) + \frac{1}{2}\chi^{(2)} E_0^2 (1 + cos(2\omega t))] \tag{7.5}$$

Where part $\frac{1}{2}\chi^{(2)} E_0^2 cos(2\omega t)$ is our second harmonic generation. Frequency doubling mechanism can be understood as follows. Due to the $\chi^{(2)}$ non-linearity, the fundamental wave generates a non-linear polarization wave which oscillates with twice the fundamental frequency. According to Maxwell's equations, this non-linear polarization wave radiates an electromagnetic field with this doubled frequency. Due to phase-matching issues, the generated second-harmonic field propagates dominantly in the direction of the non-linear polarization wave.

The phase matching of the radiated electric field of ω and 2ω is crucial in SHG. If both beam would not be in phase they would interfere destructively. The applied electric field is strong enough to generate the second order radiation, but not so strong so that the dominant term is higher, because of that we can think of second harmonic generation signal as a perturbation, and as such is small. To met this phase matching condition both waves should travel our crystal with the same speed, but in order to do that the refractive index for the two different frequencies should be the same. What is not possible in standard medium, but is possible for birefringent crystals, which posses double refractive index. This phenomenon arises from the anisotropy of the crystal structure, in which structure posses ordinary and extraordinary refractive index. In microscopic sense, different molecules radiate in different ways and this leads to difference in refractive index. Crystals which exhibit such properties are for example calcite $(CaCO_3)$, ruby (Al_2O_3), barium borate (BaB_2O_4) or even ice. The indices are dependent on both the frequency of light and the angle between propagation and optical axis:

$$\frac{1}{n_e^2(\theta)} = \frac{sin^2(\theta)}{n_e^2} + \frac{cos^2(\theta)}{n_0^2} \tag{7.6}$$

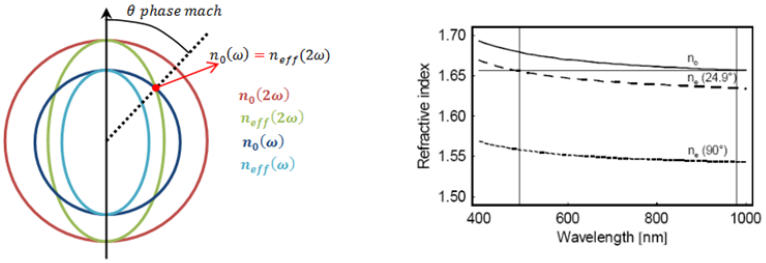

and for correct angle $n_{e,2\omega} = n_{0,\omega}$ we can obtain equation for correct angle, at which phase match can exists:

$$sin^2(\theta) = \frac{n_{0,\omega}^{-2} - n_{0,2\omega}^{-2}}{n_{e,2\omega}^{-2} - n_{0,2\omega}^{-2}} \tag{7.7}$$

So for the particular θ angle we can expect that phase matching conditions might be meet. And this is indeed true, as shown in figure 2 in case of BBO crystal. This method is so called angle tuning. Unfortunately ordinary and extraordinary rays with parallel propagation vectors will quickly diverge from one another, and because of that in such structure the overlap between them can only be maintained for a short distance. This effect is so called walk-off. Other methods of generating efficient SHG include non-critical phase matching which is particular case of angular phase matching. Which occurs when ordinary and extraordinary rays intersect at angle $\theta = 90°$, it usually occurs at higher temperatures. But the most efficient technique is so called quasi-phase matching, in periodically alternating structures, which can give high efficiency over a long length of crystal. It can be achieved through mechanical slicing of crystal into thin segments and rotating them by 180°, or in more sophisticated way of inversion of the orientation of the ferroelectric domains by external static electric field. It can be achieved in normal crystals as well as polymer structures, which are much cheaper and easy to deal with.

7.1.1 Frequency mixing and parametric generation of light

Frequency mixing is a process in non-linear crystal materials in which sum frequency generation (SFG) or difference frequency generation (DFG) can occur. In this effect two pump

beams generate another beam with the sum or difference of the optical frequencies of the pump beams. In order for efficient work our pumps needs to be in phase match, and usually there is no simultaneous phase matching for sum and difference frequency generation.

To better understand origins of this effect, lets return to the equation 7.2 for quadratic dielectric polarization, from previous section. And consider a case when two independent sources of light enter non-linear medium. The wave will take following form:

$$E(t) = E_1 cos(\omega_1 t) + E_2 cos(\omega_2 t) \tag{7.8}$$

Then let us insert this wave into equation 7.2, in result we will get:

$$P(t) = \varepsilon_0[\chi^{(1)}E + \chi^{(2)}E^2] \tag{7.9}$$

$$= \varepsilon_0[\chi^{(1)}(E_1 cos(\omega_1 t) + E_2 cos(\omega_2 t)) + \chi^{(2)}(E_1 cos(\omega_1 t) + E_2 cos(\omega_2 t))^2] \tag{7.10}$$

$$= \varepsilon_0[\chi^{(1)}(E_1 cos(\omega_1 t) + E_2 cos(\omega_2 t)) + \chi^{(2)}E_1^2 cos^2(\omega_1 t) + \chi^{(2)}E_2^2 cos^2(\omega_2 t) + 2\chi^{(2)}E_1 E_2 cos(\omega_2 t)] \tag{7.11}$$

We can see that aside of SHG terms for ω_1 and ω_2 we obtained additional term:

$$P_{1,2} = 2\varepsilon_0\chi^{(2)}E_1 E_2 cos(\omega_2 t) \tag{7.12}$$

$$= 2\varepsilon_0\chi^{(2)}E_1 E_2(cos([\omega_1 + \omega_1]t) + cos([\omega_1 - \omega_1]t)) \tag{7.13}$$

that contains sum and difference of beams that enter our medium. Thus, the second-order nonlinear medium can be used to mix two optical waves of different frequencies and generate a third wave at the sum frequency or at the difference frequency. The former process is called frequency up-conversion (or SFG) and is shown in figure 7.1, whereas the latter frequency down-conversion (or DFG) shown in figure 7.2.

Very similar effect to the SFG and DFG can be created with only single coherent pump beam to produce so called signal and idler beams. This effect can be created in so-called optical parametric oscillator. Typical optical parametric oscillator consist of nonlinear crystal placed

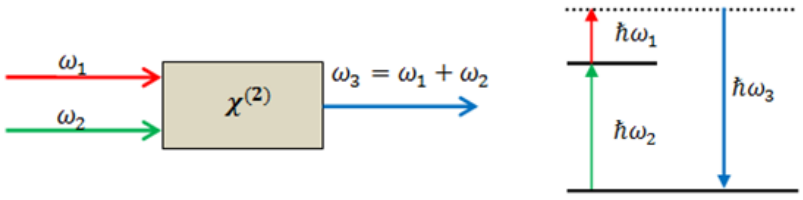

Figure 7.1: SHG process

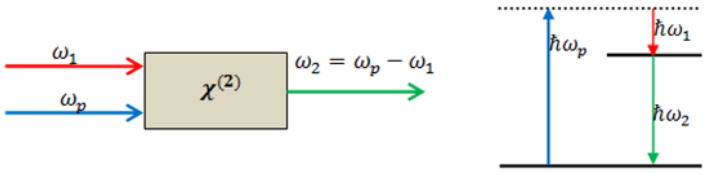

Figure 7.2: DFG process

inside of the optical resonator, as shown in figure 7.1.1. In nonlinear crystal, pump, signal and idler beams overlap. The interaction between these waves leads to amplitude gain for signal and idler waves (so-called parametric amplification) and a corresponding lowering of the pump wave.Created gain allows the resonating waves to continue oscillating in the resonator and compensate the loss that the resonating waves have experienced at each cycle.

OPO is a light source very similar to a laser (also using laser resonator), but it is based on optical gain from parametric amplification in a nonlinear crystal rather than stimulated emission. A main appeal of OPO is that the signal and idler wavelengths, which are determined by a phase-matching condition, can be varied in wide ranges. It is possible to access through OPO wavelengths which are difficult or impossible to obtain from any laser (i.e. green laser light or infra-red light source). Because of this, and the ability to produce output beams with narrow line width and high power, the OPO are very popular in spectroscopy.

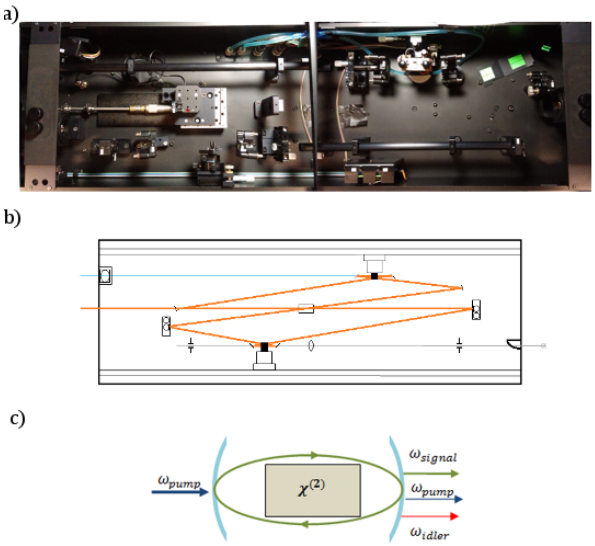

Figure 7.3: a) Photography of used setup; b) Schematic of ring OPO, optical unit with external spectrometer; c) Schematic of OPO.

7.2 Optical parameter of Bi_2Te_3

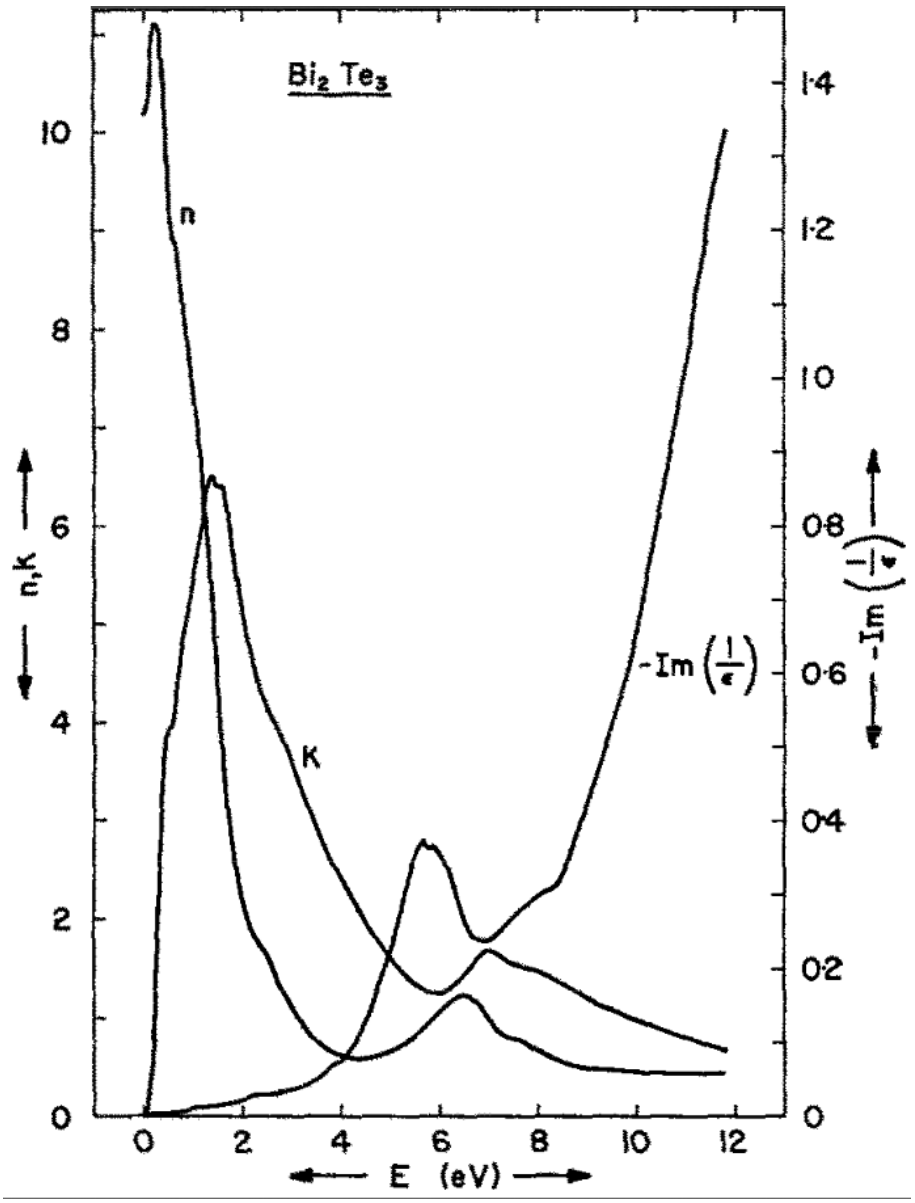

Figure 7.4: Optical constants n and k of Bi_2Te_3 and energy loss function $-Im(1/\varepsilon)$ from Kramers-Kroning analysis, $E \perp c$. From Greenaway J. Phys. Chem. Sol. (1965)[38].

7.3 Reflectivity change

Optical reflectivity is given by:

$$r = r_0 e^{i+\varphi}$$

first derivative:

$$r' = r_0(1+\varphi)e^{i\varphi+id\varphi}$$

The change of the system reflectivity is given by:

$$\frac{\Delta R}{R} = \frac{r^{*\wr} r' - r r^*}{r r^*}$$

$$= \frac{r_0^2 r_0^2 \varphi + r_0^2 \varphi^2 - r_0^2}{r_0^2} = 2\varphi + \varphi^2$$

we will assume that $\varphi \ll 1$ then the term φ^2 is negligible in result:

$$\frac{\Delta R}{R} = 2\varphi \tag{7.14}$$

The change of optical reflectivity can be defined as:

$$\frac{\Delta r}{r} = \frac{r' - r}{r} =$$

$$= \frac{r_0(1+\varphi)e^{i(\varphi+d\varphi)} - r_0 e^{i\varphi}}{r_0 e^{i\varphi}} =$$

$$= (1+\varphi)e^{id\varphi} - 1$$

by Taylor expansion:

$$\frac{\Delta r}{r} = (1+\varphi)(1+id\varphi) - 1 = \varphi + id\varphi + i\varphi d\varphi$$

the part $i\varphi d\varphi$ is negligible giving us:

$$\frac{\Delta r}{r} = \varphi + id\varphi \rightarrow \varphi = Real\frac{\Delta r}{r}$$

knowing that the reflectivity change of the system eq.6.1 takes form:

$$\frac{\Delta R}{R} = 2Real\left(\frac{\Delta r}{r}\right)$$

7.4 Publications

List of Figures

List of Tables

Bibliography

[1] J.E. Moore, L. Balents, Phys. Rev. B 75, 121306(R) (2007)

[2] J. E. Moore, Nature 464, 194-198 (2010)

[3] M.Z. Hasan, C.L. Kane, Rev. Mod. Phys. 82, 3045-3064 (2010)

[4] X.-L. Wang, S.X. Dou, C. Zhang, NPG Asia Mater, 2, 31-38 (2010)

[5] R. Dey, N. Prasad, L.F. Register, S.K. Banerjee, Phys. Rev. B 97, 174406 (2018)

[6] I. Žutić, J. Fabian, S.D. Sarma, Rev. Mod. Phys. 76, 323 (2004)

[7] J. Sinova, S.O. Valenzuela, J.Wunderlich, C.H. Back, T. Jungwirth, Rev. Mod. Phys. 87, 1213 (2015)

[8] F. Vidal, M. Eddrief, B. Rache Salles, I. Vobornik, E. Velez-Fort, G. Panaccione, M. Marangolo, Phys. Rev. B 83, 241410(R) (2013)

[9] Y. Zhang, et al., Nature Phys. 6, 584-8 (2010)

[10] J. Linder, T. Yokoyama, A Sudbo, Phys. Rev. B 80, 205401 (2009)

[11] Y.Y. Li, et. al. Adv. Mater. 22, 4002-4007 (2010)

[12] M. Weis, B. Wilk, G. Vaudel, K. Balin, R. Rapacz, A. Bulou, B. Arnaud, J. Szade, P. Ruello, Sci. Rep. 7: 13782 (2017)

[13] F. Bloch, Zeitschrift für Physik 52, 7, (1929) 555

[14] T. Ando, Y. Matsumoto, Y. Uemura, J. Phys. Soc. Japan 39, pp 279-288 (1975)

[15] K.v. Klitzing, G. Dorda, M. Pepper, Phys. Rev. Lett. 45, 6, (1980) 494

[16] H. Zhang, C.X. Liu, X.L. Qi, X. Dai, Z. Fang, S.C. Zhang, Nature Phys. 5, 10.103 (2009)

[17] D. Xiao, M-Ch. Chang, Q. Niu, Rev. Mod. Phys 82.1959 (2010)

[18] J. Alicea, Rep. Prog. Phys 75, 7 (2012)

[19] D. Hsieh, D. Qian, L. Wray, Y. Xia, Y.S. Hor, R.J. Cava, M.Z. Hasan, Nature, 452, 970-974 (2008)

[20] B.A. Bernevig, T.L. Hughes, S.C. Zhang, Science, 314, 1757-1761 (2006)

[21] K. Shen, G. Vignale, R. Raimondi, Phys. Rev. Lett. 112, 096601 (2014)

[22] K.T. Yamamoto, Y. Shiomi, K. Segawa, Y. Ando, E. Saitoh, Phys. Rev. B94, 024404 (2016)

[23] J.C. Rojas-Sanchez, S. Oyarzun, Y. Fu, A. Marty, C. Vergnaud, S. Gambarelli, L. Vila, M. Jamet, Y. Ohtsubo, A. Taleb-Ibrahimi, P. Le Fèvre, F. Bertran, N. Reyren, J.M. George, A. Fert, Phys. Rev. Lett. 116, 096602 (2016)

[24] Z. Alpichshev, J.G. Analytis, J.H. Chu, I.R. Fisher, Y.L. Chen, Z.X. Shen, A. Fang, A. Kapitulnik, Phys. Rev. Lett. 104, 016401 (2010)

[25] P. Roushan, J. Seo, C.V. Parker, Y.S. Hor, D. Hsieh, D. Qian, A. Richardella, M.Z. Hasan, R.J. Cava, A. Yazdani, Nature 460, 1106–1109 (2009)

[26] J. Chen, H.J. Qin, F. Yang, J. Liu, T. Guan, F.M. Qu, G.H. Zhang, J.R. Shi, X.C. Xie, C.L. Yang, K.H. Wu, Y.Q. Li, L. Lu, Phys. Rev. Lett. 105, 176602 (2010)

[27] M.V. Costache, I. Neumann, J.F. Sierra, V. Marinova, M.M. Gospodinov, S. Roche, S.O. Valenzuela, Phys. Rev. Lett. 112, 086601 (2014)

[28] D. Kim, Q. Li, P. Syers, N.P. Butch, J. Paglione, S.D. Sarma, M.S. Fuhrer, Phys. Rev. Lett. 109, 166801 (2012)

[29] M. Weis, K. Balin, R. Rapacz, A. Nowak, M. Lejman, J. Szade, P. Ruello, Phys Rev. B 92, 014301 (2015)

[30] R. Rapacz, K. Balin, A. Nowak, J. Szade, Journal of Crystal Growth 401 567-572 (2014)

[31] C.X. Liu, H.J. Zhang, B. Yan, X.L. Qi, T. Frauenheim, X. Dai, Z. Fang, S.C. Zhang, Phys. Rev. B 81, 041307(R) (2010)

[32] H.Z. Lu, W.Y. Shan, W. Yao, Q. Niu, S.Q. Shen, Phys. Rev. B 81, 115407 (2010)

[33] M. Konig, H. Buhmann, L.W. Molenkamp, T. Hughes, C.X. Liu, X.L. Qi, S.C. Zhang, J. Phys. Soc. Jpn. 77, 031007 (2008)

[34] K. Balin, R. Rapacz, M. Weis, J. Szade, AIP Advances 7, 056323 (2017)

[35] Y. Feutelais, Materials Research Bulletin 28 (1993)

[36] J. Kaczkowski, A. Jezierski, Materials Science-Poland 4, 26 (2008)

[37] P. Larson, S.D. Mahanti, M.G. Kanatzidis, Phys. Rev. B 61, 8162 (2000)

[38] D.L. Greenaway, G. Harbeke, J. Phys. Chem. Solids 26, 1585 (1965)

[39] W. Richter, H. K öhler, C.R. Becker, Phys. Status Solidi B 84, 619 (1977)

[40] W. Kullmann, J. Geurts, W. Richter, N. Lehner, H. Rauh, U. Steigenberger, G. Eichhorn, G. Geick, Phys. Status Solidi B 125, 131 (1984)

[41] Y. Wang, L. Guo, X. Xu, J. Pierce, and R. Venkatasubramanian, Phys. Rev. B 88, 064307 (2013)

[42] M. A. Herman, H. Sitter, Molecular Beam Epitaxy: Fundamentals and Current Status, Springer-Verlag, 1989

[43] E. Zaremba and W. Kohn, Phys. Rev. B 15 (4): 1769, (1977)

[44] K. Hoefera, C. Beckera, D. Rataa, J. Swansona, P. Thalmeiera, and L. H. Tjenga, PNAS 101, 14979-14984 (2014)

[45] S. Golia, M. Arora, R.K. Sharma, A.C. Rastogi, Current App. Phys. 3 195-197 (2003)

[46] K. Watanabe, N. Sato, S. Miyoba, J. Appl. Phys. 54 1256 (1983)

[47] F.A.A. Amin, A.S.S. Al Ghaffari, M.A. Issar, A.M. Habib, J. Mater. Sci. 27 1250 (1992)

[48] S.A. Omer, U.G. Isifield, Solar Energy Mater. Solar Cell 53 67 (1998)

[49] J.C. Tedenac, S. Charar, Phys. Low Dimens. Struct. 5-6 61 (2000)

[50] J. W.G. Bos, F. Faucheux, R.A. Downie, A.J. Marcinkova, Sol. Stat. Chem. 193, 13-18 (2012)

[51] R.J. Cava, J. Huiwen , M.K. Fuccillo, Q.D. Gibson, Y.S. Hor, J. Mater. Chem. C 1 (2013) 3176

[52] M.P. Seah, S.J. Specer, Surf. Interf. Anal. 33, (2002) 631

[53] S. Tanuma, C. J. Powell, D. R. Penn, Surf. Interf. Anal. 21, (1994)165

[54] QUASES program by S. Tougaard

[55] A.P. Grosvenor, B.A. Kobe, M.C. Biesinger, N.S. McIntyre, Surf. Interface Anal. 36: 1564 – 1574 (2004)

[56] C. Kittel, Introduction to Solid State Physics, J. Wiely and Sons, 8th Edition (2005)

[57] V.E. Gusev, O.B. Wright, Phys. Rev. B 57, 5 (1998)

[58] M. I. Kaganov, I. M. Lifshitz, L. V. Tana-tarov, Sov. Phys. JETP4, 173 (1957)

[59] V.E. Gusev, A. A. Karabutov, AIP Press, New York (1993)

[60] P. Ruello, V. E. Gusev, Ultrasonics 56, 21-36 (2015)

[61] E. Golias, J. Sanchez-Barriga, Phys. Rev. B 94, 161113(R) (2016)

[62] M. Perner, S. Gresillon, J. Mrz, G. von Plessen, J. Feldmann J. Porstendorfer, K.-J. Berg, G. Berg, Phys. Rev. Lett. 85, 792 (2000)

[63] C. Thomsen, H. T. Grahn, H. J. Maris, J. Tauc, Phys. Rev. B 34, 6 (1986)

[64] Y.X. Yan, E.B. Gamble, K.A. Nelson, J. Chem. Phys. 83, 5391 (1985)

[65] R. Merlin, Sol. Stat. Comm. 2-3, 207-220 (1997)

[66] H. J. Zeiger, J. Vidal, T.K. Cheng, E.P. Ippen, G. Dresselhaus, M.S. Dresselhaus, Phys. Rev. B 45, 2 (1992)

[67] P. Yu, M. Cardona, Fundamentals of Semiconductors, Springer

[68] M. Eddrief, P. Atkinson, V. Etgens, and B. Jusserand, Nanotechnology 25, 245701 (2014)

[69] N. Kamaraju, S. Kumar, and A. K. Sood, Eur. Phys. Lett. 92, 47007 (2010)

[70] K. Norimatsu, J. Hu, A. Goto, K. Igarashi, T. Sasagawa, and K. G. Nakamura, Sol. State Commun. 157, 58 (2013)

[71] S. Y. F. Zhao, C. Beekman, L. J. Sandilands, J. E. J. Bashucky, D. Kwok, N. Lee, A. D. LaForge, S. W. Cheong, and K. S. Burch, Appl. Phys. Lett. 98, 141911 (2011)

[72] C. B. Satterthwaite and R. W. Ure Jr., Phys. Rev. 108, 1164 (1957)

[73] B.-L. Huang and M. Kaviany, Phys. Rev. B 77, 125209 (2008)

[74] T. Garl, E. G. Gamaly, D. Boschetto, A. V. Rode, B. Luther-Davies, and A. Rousse, Phys. Rev. B 78, 134302 (2008)

[75] M. Hajlaoui, E. Papalazarou, J. Mauchain, G. Lantz, N. Moisan, D. Boschetto, Z. Jiang, I. Miotkowski, Y. P. Chen, A. Taleb-Ibrahimi, L. Perfetti, M. Marsi, Nano Lett. 12, 3532-3536 (2012)

[76] A. Ayouch, X. Dieudonne, G. Vaudel, H. Piombini, K. Valle, V. Gusev, P. Belleville, and P. Ruello, ACS Nano 6, 10614 (2012)

[77] C. Mechri, P. Ruello, and V. Gusev, New. J. Phys. 14, 023048 (2012)

[78] V. Juve, A. Crut, P. Maioli, M. Pellarin, M. Broyer, N. Del Fatti, and F. Vallée, Nano Lett. 5, 1853 (2010)

[79] Y. Wang, C. Liebig, X. Xu, and R. Venkatasubramanian, Appl. Phys. Lett. 97, 083103 (2010)

[80] D. J. Cebula et al., Clays Min. 17, 195 (1987)

[81] S. L. Johnson, et al. Phys. Rev. Lett. 100, 155501 (2008)

[82] J. M. Ziman, Principle of Theory of Solids, Cambridge University Press (1964)

[83] Y. Wang, B. Qiu, A. J. H. McGaughey, X. Ruan, and X. Xu, J.Heat Trans. 135, 091102 (2013)

[84] J. R. Wiese and L. Muldawer, J. Phys. Chem. Solids 15, 13 (1960)

[85] C. Thomsen, H. T. Grahn, H. J. Maris, and J. Tauc, Phys. Rev. B 34, 4129 (1986)

[86] M. H. Francombe, Br. J. Appl. Phys. 9, 415 (1958)

[87] L. Xue-Dong and Y.-H. Park, Mat. Trans. 43, 681 (2002)

[88] P. Ruello, S. Zhang, P. Laffez, B. Perrin, and V. Gusev, Phys. Rev. B. 79, 094303 (2009)

[89] B. Zhou, et al. Phys. Rev. Lett. 101, 246807 (2008)

[90] C-X. Liu, et al. Phys. Rev.B 81, 041307 (2010).

[91] . Kim, et al. Nanotech. 27 045705 (2016)

[92] J. A. Sobota, et al. Phys. Rev. Lett. 108, 117403 (2012)

[93] D. Hsieh, et al. Phys. Rev. Lett. 107, 077401 (2011)

[94] E. Golias and J. Sanchez-Barriga, Phys. Rev. B 94, 161113(R) (2016)

[95] S. Giraud, A. Kundu, R. Egger, Phys. Rev. B 85, 035441 (2012)

[96] S. Giraud, A. Kundu, R. Egger, Phys. Rev. B 85, 035441 (2012)

[97] M. Eddrief, P. Atkinson, V. Etgens, B. Jusserand, Nanotech. 25, 245701 (2014)

[98] K. M. Shahil, M. Z. Hossain, D. Teweldebrhan, A. A.Balandin, Appl. Phys. Lett. 96, 153103 (2010)

[99] Y. Giret, A. Gellé, B. Arnaud, Phys. Rev. Lett. 106, 155503 (2011)

[100] F. Vidal et al., Phys. Rev. B 88, 241410 (2013)

[101] Y. Li, et al., Adv. Mater. 22, 4002–4007 (2010)

[102] G. Allan, C. Delerue, Phys. Rev. B 70, 245321 (2004)

[103] B-L. Huang, M. Kaviany, Phys. Rev. B 77, 125209 (2008)

[104] D.M. Mittleman, Phys. Rev. B 49, 14435 (1994)

[105] A. Stella, et. al., Phys. Rev. B 53, 15497–15500 (1996)

[106] A. Arbouet, et. al., Phys. Rev. Lett. 90, 177401–4 (2003)

[107] Y.D. Glinka, et. al., Appl. Phys. Lett. 103, 151903 (2013)

[108] M. Hajlaoui, et. al., Nature Comm. 5, 3003 (2014)

[109] O. B. Wright J. Appl. Phys. 71, 1617 (1992)

[110] V. Gusev, Acta Acustica 82, S37 (1996)

[111] O. Matsuda, O.B. Wright, Rev. Sci. Instrum. 74, 895 (2003)

[112] S. Mohanty and J. Ghose, J. Phys. Chem. Solids 53, 81 (1992)

[113] W.H Strehlow, E.L. Cook, J. Phys. Chem. Ref. Data 2, 163 (1973)

[114] A.G. Joly, J.R. Williams, S.A. Chambers, G. Xiong, W.P. Hess, D.M. Laman, J. App. Phys. 99, 053521 (2006)

[115] R. Grau-Crespo, A. Y Al-Baitai, I. Saadoune, N. H De leeuw, J. Phys. Condens. Matter 22, 255401 (2010)

[116] S. Chakrabarti, D. Ganguli, S. Chaudhuri, Physica E 24, 333-342 (2004)

[117] J.K. Vassiliou, V. Mehrotra, M.W. Russell, E.P. Giannelis, R.D. McMichael, R.D. Shull, R.F. Ziolo, J. Appl. Phys. 73, 5109 (1993)

[118] N. J. Cherepy, D. B. Liston, J. A. Lovejoy, H. Deng, and J. Z. Zhang, J. Phys. Chem. B 102, 770 (1998)

[119] E.S. Harmon, M.R. Melloch, J.M. Woodall, D.D. Nolte, N. Otsuka, C.L. Chang, Appl. Phys. Lett. 63, 2248 (1993)

[120] L. A. Wray, Y. Xia, S.-Y. Xu, R. Shankar, Y.S. Hor, R.J. Cava, A. Bansil, H. Lin, M.Z. Hasan, Nature Phys. 7, 32–37 (2011)

[121] J. Honolka, et. al., Phys. Rev. Lett. 108, 256811 (2012)

[122] H. Yan, D. Song, K. F. Mak, I. Chatzakis, J. Maultzsch, T.F. Heinz, Phys. Rev. B 80(12), 121403 (2009)

[123] G. Lantz, B. Mansart, D. Grieger, D. Boschetto, N. Nilforoushan, E. Papalazarou, N. Moisan, L. Perfetti, V. L. R. Jacques, D. Le Bolloc'h, C. Laulhé, S. Ravy, J-P Rueff, T. E. Glover, M. P. Hertlein, Z. Hussain, S. Song, M. Chollet, M. Fabrizio, M. Marsi, Nat Commun. 8: 13917 (2017)

[124] R. Ernstorfer, M. Harb, C. T. Hebeisen, G. Sciaini, T. Dartigalongue, R. J. D. Miller, Science 323(5917):1033–7 (2009)

[125] V. Recoules, J. Clerouin, G. Zerah, P. M. Anglade,S. Mazevet, Phys. Rev. Lett. 96, 055503 (2006)

[126] F. Bottin, G. Zerah, Phys. Rev. B 75, 174114 (2007)

[127] S. Mazevet, J. Clérouin, V. Recoules, P. M. Anglade,G. Zérah, Phys. Rev. Lett. 95, 085002 (2005)

[128] D. Boschetto, L. Malard, CH. Lui, K.F. Mak, Z. Li, H. Yan, T.F. Heinz, Nano letters 13 (10), 4620-4623 (2013)